2013

Prediction Of Optical Properties Of Pi-conjugated Organic Materials For Technological Innovations

Iffat Nayyar
University of Central Florida

PREDICTION OF OPTICAL PROPERTIES OF PI-CONJUGATED ORGANIC MATERIALS FOR TECHNOLOGICAL INNOVATIONS

by

IFFAT H. NAYYAR
B.S. University of Delhi, New Delhi, India, 2003
M.S. University of Delhi, India, New Delhi, India, 2005

A dissertation submitted in partial fulfillment of the requirements
for the degree of Doctor of Philosophy
in the Department of Physics
in the College of Sciences
at the University of Central Florida
Orlando, Florida

Spring Term
2013

Major Professor: Artëm E. Masunov

ABSTRACT

Organic π-conjugated solids are promising candidates for new optoelectronic materials. The large body of evidence points at their advantageous properties such as high charge-carrier mobility, large nonlinear polarizability, mechanical flexibility, simple and low cost fabrication and superior luminescence. They can be used as nonlinear optical (NLO) materials with large two-photon absorption (2PA) and as electronic components capable of generating nonlinear neutral (excitonic) and charged (polaronic) excitations. In this work, we investigate the appropriate theoretical methods used for the (a) prediction of 2PA properties for rational design of organic materials with improved NLO properties, and (b) understanding of the essential electronic excitations controlling the energy-transfer and charge-transport properties in organic optoelectronics. Accurate prediction of these electro-optical properties is helpful for structure-activity relationships useful for technological innovations.

In Chapter 1 we emphasize on the potential use of the organic materials for these two applications. The 2PA process is advantageous over one-photon absorption for deep-tissue fluorescence microscopy, photodynamic therapy, microfabrication and optical data storage owing to the three-dimensional spatial selectivity and improved penetration depth in the absorbing or scattering media. The design of the NLO materials with large 2PA cross-sections may reduce the optical damage due to the use of the high intensity laser beams for excitation. The organic molecules also possess self-localized excited states which can decay radiatively or nonradiatively to form excitonic states. This suggests the use of these materials in the electroluminescent devices such as light-emitting diodes and photovoltaic cells through the processes of exciton formation or dissociation, respectively. It is therefore necessary to understand ultrafast relaxation processes required in understanding the interplay between the

efficient radiative transfer between the excited states and exciton dissociation into polarons for improving the efficiency of these devices. In Chapter 2, we provide the detailed description of the various theoretical methods applied for the prediction as well as the interpretation of the optical properties of a special class of substituted PPV [poly (p-phenylene vinylene)] oligomers.

In Chapter 3, we report the accuracy of different second and third order time dependent density functional theory (TD-DFT) formalisms in prediction of the 2PA spectra compared to the experimental measurements for donor-acceptor PPV derivatives. We recommend *a posteriori* Tamm-Dancoff approximation method for both qualitative and quantitative analysis of 2PA properties. Whereas, Agren's quadratic response methods lack the double excitations and are not suitable for the qualitative analysis of the state-specific contributions distorting the overall quality of the 2PA predictions. We trace the reasons to the artifactual excited states above the ionization threshold. We also study the effect of the basis set, geometrical constraints and the orbital exchange fraction on the 2PA excitation energies and cross-sections. Higher exchange (BMK and M05-2X) and range-separated (CAM-B3LYP) hybrid functionals are found to yield inaccurate predictions both quantitatively and qualitatively. The failure of the exchange-correlation (XC) functionals with correct asymptotic is traced to the inaccurate transition dipoles between the valence states, where functionals with low HF exchange succeed.

In Chapter 4, we test the performance of different semiempirical wavefunction theory methods for the prediction of 2PA properties compared to the DFT results for the same set of molecules. The spectroscopic parameterized (ZINDO/S) method is relatively better than the general purpose parameterized (PM6) method but the accuracy is trailing behind the DFT methods. The poor performances of PM6 and ZINDO/S methods are attributed to the incorrect description of excited-to-excited state transition and 2PA energies, respectively. The different

semiempirical parameterizations can at best be used for quantitative analysis of the 2PA properties. The ZINDO/S method combined with different orders of multi-reference configuration interactions provide an improved description of 2PA properties. However, the results are observed to be highly dependent on the specific choice for the active space, order of excitation and reference configurations.

In Chapter 5, we present a linear response TD-DFT study to benchmark the ability of existing functional models to describe the extent of self-trapped neutral and charged excitations in PPV and its derivative MEH-PPV considered in their *trans*-isomeric forms. The electronic excitations in question include the lowest singlet (S_1) and triplet ($T_1^{\dagger}$) excitons, positive (P^+) and negative (P^-) polarons and the lowest triplet (T_1) states. Use of the long-range-corrected DFT functional, such as LC-wPBE, is found to be crucial in order to predict the physically correct spatial localization of all the electronic excitations in agreement with experiment. The inclusion of polarizable dielectric environment play an important role for the charged states. The particle-hole symmetry is preserved for both the polymers in *trans* geometries. These studies indicate two distinct origins leading to self-localization of electronic excitations. Firstly, distortion of molecular geometry may create a spatially localized potential energy well where the state wavefunction self-traps. Secondly, even in the absence of geometric and vibrational dynamics, the excitation may become spatially confined due to energy stabilization caused by polarization effects from surrounding dielectric medium.

In Chapter 6, we aim to separate these two fundamental sources of spatial localization. We observe the electronic localization of P^+ and P^- is determined by the polarization effects of the surrounding media and the character of the DFT functional. In contrast, the self-trapping of the electronic wavefunctions of S_1 and $T_1(T_1^{\dagger})$ mostly follows their lattice distortions. Geometry

relaxation plays an important role in the localization of the S_1 and $T_1^{\dagger}$ excitons owing to the non-variational construction of the excited state wavefunction. While, mean-field calculated P^+, P^- and T_1 states are always spatially localized even in ground state S_0 geometry. Polaron P^+ and P^- formation is signified by the presence of the localized states for the hole or the electron deep inside the HOMO-LUMO gap of the oligomer as a result of the orbital stabilization at the LC-wPBE level. The broadening of the HOMO-LUMO band gap for the T_1 exciton compared to the charged states is associated with the inverted bond length alternation observed at this level. The molecular orbital energetics are investigated to identify the relationships between state localization and the corresponding orbital structure.

In Chapter 7, we investigate the effect of various conformational defects of *trans* and *cis* nature on the energetics and localization of the charged P^+ and P^- excitations in PPV and MEH-PPV. We observe that the extent of self-trapping for P^+ and P^- polarons is highly sensitive on molecular and structural conformations, and distribution of atomic charges within the polymers. The particle-hole symmetry is broken with the introduction of *trans* defects and inclusion of the polarizable environment in consistent with experiment. The differences in the behavior of PPV and MEH-PPV is rationalized based on their orbital energetics and atomic charge distributions. We show these isomeric defects influence the behavior and drift mobilities of the charge carriers in substituted PPVs.

Dedicated

with love

to

my dad (Late) M. Tahir Nayyar

and

my mom Nigar Nayyar

ACKNOWLEDGMENTS

Here, comes the time for the much awaited and valued part of my dissertation where I would like to extend my heartfelt gratitude to each one of those who have bestowed their blessings, wishes and support on me in making this day possible. It was more than my privilege being associated to my supervisor Prof. Dr. Artëm E. Masunov at University of Central Florida. My sincere thanks to Dr. Masunov for all his guidance, mentorship and advice which wasn't just limited to the confines of academic domain. His help, encouragement and motivation to carry out diverse projects during my graduate school have given me enormous opportunities to excel in the field of Science. I would also like to thank my wonderful dissertation committee members Dr. Hari P. Saha, Dr. Sergey Stolbov and Dr. Andre Gesquire for their time and critical comments which helped me improve the quality of my work immensely. I value the contribution of all the members of Multiscale Simulation Laboratory, NanoScience Technology Center, UCF for their help and support during my stay in the group. A special word of appreciation for Dr. Ivan A. Mikhailov 'the postdoc' for his long and useful scientific discussions.

It has entirely been an honor serving as an intern during my Ph.D. at 'the prestigious' Los Alamos National Laboratory with an opportunity to work with some of the genius minds in the field. I humbly acknowledge the contribution of Dr. Sergei Tretiak, Dr. Enrique Batista, Dr. Avadh Saxena, Dr. Darryl Smith and Dr. Richard Martin for adding to my professional growth and knowledge during my stay there. My association with Dr. Peter J. Delfyett and Dr. Eduardo Mucciolo has added myriad dimensions to my graduate experiences at UCF. Not to mention, all my present and previous teachers and professors at UCF and back home in India have played a significant role in laying the foundation of my career in Science. I have learnt a great deal from each one of these dynamic people who have helped me emerge as a better scientist today. I thank

them all from the bottom of my heart, especially to Anand Sir and Zafar Sir for their extreme support and guidance.

Luck has always been on my side when it comes to having genuine friends around. And Purvi serves the first on the list with Ivana, Gautam, Nupur and many more to follow. I take this opportunity to thank each one of them for standing by me unconditionally at all times. Divya Di and Chandana Di indeed deserve a great recognition for always motivating me to apprehend my capabilities. The time spent with all the roommates while at UCF has surely added many beautiful memories to my stay. Farzana and KK are also profoundly remembered for their help and encouragement in the times of need. I would certainly fall short of words on the mention of a dear friend Rajat 'the dangerous'. While he has been occupied in deriving the relationship between space and time, I have been holding on to our timeless friendship. His positive influence on my life is visible in many forms.

It has almost become a custom that the priceless contribution of the family members is written towards the end, but that in no way diminishes the importance of their presence in our lives. My Dad, being an educationist, had always laid emphasis on gaining and sharpening one's knowledge. He had taught me the key element to success, which lies in the sheer hard work and perseverance. He continued to guide me through all the walks of my life even after his heavenly abode. It was primarily his dreams and expectations, which have motivated me to achieve my goals in life. But truly this would not have been possible without my Mom's love, sacrifices and prayers. I can't thank her enough for having faith in all my decisions and standing beside me at every step of my life. My charismatic younger brother Athar not only has an extremely precious place in my heart but also has been my biggest strength so far. I have always cherished his critical yet constructive comments for inspiring me to attain the booming heights of success in all

my endeavors. Both the sets of my Grandparents are acutely thought of on this occasion. Although I did not get the chance to see my Grandfather from my Dad's side but he has been 'the epitome of cognizance and perfection' for the entire family. Not to forget, my extended family from both sides of the parents has always been praying for my well being and success.

The place my Dad holds in my life is undeniably irreplaceable by all means but my Father-in-law did fill that gap although for a short period. I want to thank my Father and Mother-in law for all their blessings and encouragement for my Ph.D. My husband Arif deserves being acknowledged for many more reasons than one can precisely think off. He has not left any stone unturned to provide me with the mental peace, inner strength and eternal happiness to combat with the pressures of completing the degree. His support and motivation for my academic career and professional growth has been the principal source of my achievements. I thank him for being in my life and adding colors to it in innumerable ways.

Despite my best efforts, surely I have not been able to mention all the people who have touched upon my life in one way or the other during my Ph.D. I would always owe them a deep sense of gratitude.

TABLE OF CONTENTS

LIST OF FIGURES

LIST OF TABLES

CHAPTER 1 INTRODUCTION

1.1 Conjugated Organic Systems

Functional π-conjugated organic materials are in much demand these days due to their variety of optoelectronic applications important for technological innovations in the field of interdisciplinary sciences such as physics, chemistry and biology. They are also a popular model to verify new theoretical methods and to study the ground and excited state electronic structures as a function of the length of conjugated chain, symmetry, total charge, topology of terminal groups etc. The characteristic π-electron structure of these compounds is such that they become conductive upon chemical doping, charge injection, or photoexcitation, and thus exhibit the electrical and optical properties of metals or semiconductors. The semiconducting behavior is however associated with the π orbitals forming delocalized valence and conduction wavefunctions supporting the mobile charge carriers. Thus, these conjugated systems with conducting properties possess a number of advantages over traditional inorganic semiconductors and have revolutionized the electronics and photonics industry. In this work, we will consider two aspects of light interacting with conjugated materials: (a) resonant absorption of two photons creating an excitation, and (b) evolution of excitation, including charge separation and recombination processes. They are considered in the following two sections.

1.2 Two-Photon Absorption

Optical materials with enhanced NLO responses, especially multi-photon absorbing properties, have important technological implications such as compact data storage,[1] microfabrication,[2] optical power limiting an up-conversion lasing,[3] bio-imaging,[4] photodynamic therapy[5] and three dimensional fluorescence microscopy.[6]

NLO properties are commonly defined in terms of susceptibility tensors χ, the coefficients in Taylor series expansion for polarization vector components P_i (dipole moment per unit volume), produced by macroscopic electric field components E_i(i=x,y,z)

$$P_i = \eta(\chi_{ik}^{(1)} E_k + \frac{1}{2}\chi_{ikl}^{(2)} E_k E_l + \frac{1}{6}\chi_{iklm}^{(3)} E_k E_l E_m) \tag{1.1}$$

where η is dielectric constant. Unlike linear case of absorption, probability of electronic excitation in a material caused by simultaneous absorption of two photons is quadratically proportional to the intensity of this beam

$$P_{2PA} = t.\sigma_{2PA}.\frac{I}{\hbar\omega} \quad , \quad P_{2PA} = t.\sigma_{2PA}.\frac{I^2}{\hbar\omega} \tag{1.2}$$

where $\hbar$ is Plank's constant, I is irradiance with frequency ω, t is the time of exposure, and σ_{1PA} and σ_{2PA} are one-photon and two-photon absorption (1PA and 2PA) cross-sections, respectively. These cross-sections are dependent on imaginary parts of respective susceptibilities

$$\sigma_{1PA} = \frac{4\pi\hbar\omega}{\eta c}\,\mathrm{Im}\left\langle \chi^{(1)}(-\omega;\omega)\right\rangle \tag{1.3}$$

$$\sigma_{2PA} = \frac{4\pi^2\hbar\omega^2}{\eta^2 c^2}\,\mathrm{Im}\left\langle \chi^{(3)}(-\omega;\omega,\omega,-\omega)\right\rangle \tag{1.4}$$

where c is speed of light. As a result, the excitation due to the 2PA can be confined to a small volume in space by a tightly focused laser beam as represented in Figure 1.1. If the excitation initiates photophysical or photochemical change in the material, this localized process can be used to keep large amounts of information in individually addressable three-dimensional arrays of storage bits. The 2PA can be used to increase the spatial resolution beyond the diffraction-limited 1PA processes. In addition, in three-dimensional memory design, the data holding capacity is increased by a factor proportional to the thickness of the medium. One of the proposed technologies for three-dimensional optical memory is photon-mode (as opposed to

heat-mode) recording. This technology uses polymers, doped with the photochromophores (molecules which undergo a reversible photoinduced isomerization or photochromism).[7]

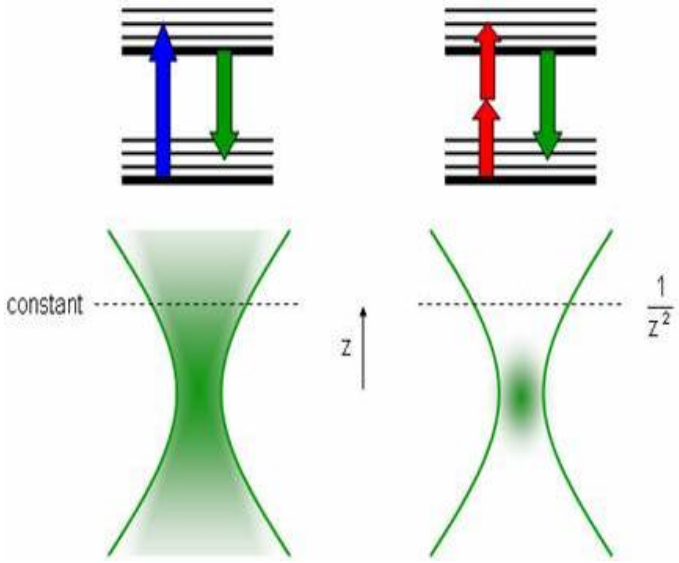

Figure 1.1: Schematic representation of 1PA and 2PA processes.
Because the 2PA processes is nonlinear, the fluorescence is confined to the focal center of the laser beam, and fluorescence power decays as $1/z^2$, where z is the axial distance away from the focus. (Source: www.biomicroscopy.bu.edu/r_nonlinear.html)

Identification of design strategies for the development of organic chromophores with large 2PA cross-sections offer the potential for greater sensitivity in various optoelectronic processes. This allows lower laser intensities to be used for excitation, and reduced probability of optical damage. Thus, reliable theoretical predictions of these properties (both frequencies and cross sections) of organic polymers possessing large cross-sections facilitate the computational NLO materials design as an alternative to costly and time-consuming synthesis and NLO measurements.

Traditional approaches use wavefunction theory (WFT) coupled with sum-over-states (SOS) formalism[8] to provide the NLO description. SOS method is based on the expansion of the

molecular energy in powers of the electric field. It requires the energies for ground and excited states, their permanent dipole moments and transition dipole moments between them. *Ab initio* WFT methods are computationally expensive and become intractable when applied to the molecules of practical interest. For this reason, semiempirical Hamiltonians have been used widely within the WFT methods. Semiempirical WFT methods typically combine model approximate Hamiltonian (such as intermediate neglect of differential overlap, INDO Hamiltonian, or its spectroscopic parameterization ZINDO/S) with different configuration interaction (CI) or coupled cluster (CC) wavefunctions. They have been exploited by several research groups as computationally efficient method to study the 2PA properties of conjugated compounds and their structure-property relations.[9-12] For instance, Breda's group published results of INDO calculations with the multi-reference CI wavefunctions, including single and double excitations (INDO/MRCISD).[13] In this work the experimental trends in the measured 2PA cross-sections for bis(styryl) benzene derivatives were reproduced well, although the excitation energies were markedly overestimated. The deviations in the excitation energies were somewhat improved by Das *et al.*[14] They used the Austin Model 1 (AM1) to optimize molecular geometries, while the INDO/CISD method was used to predict 2PA cross-sections. Zojer *et al.*[15] observed a good agreement of both the excitation energies and dipole matrix elements calculated at the INDO/MRCISD level with the experiment for AM1 optimized geometries of quadrupolar stilbene derivatives. The 1PA and 2PA properties were investigated for the AM1 optimized paracyclophane derivatives using single reference CIS and CISD excited wavefunctions using ZINDO program by Zhou *et al.*[16] Hales *et al.*[17] reported the quantitative and qualitative agreement of the 2PA spectra of the fluorine derivatives with the experiment when the first 300 excited states predicted by INDO/MRCISD were included in the perturbative SOS formalism.

Corredor *et al.*[18] provided an insight into the nature of the electronic transitions and essential states contributing primarily to the observed 1PA and 2PA states using CIS method in ZINDO/S parameterization for AM1 optimized geometries of diarylethene derivatives. Zhu *et al.*[19] reported the cross-sections to be overestimated by an order of magnitude for the isolated porphyrin in contrast to the corresponding dimer calculated by the MRCISD method with the ZINDO code. However, the results were shown to be extremely sensitive on the choice of the CI active space and reference determinants. The 2PA cross-sections calculated using the INDO/MRCISD method and based on the density functional theory (DFT) optimized geometries were tuned by an order of magnitude with varying the nature, order and orientation of the heterocycles in the donor-acceptor dipolar chromophores.[20] In another study by Li *et al.*,[21] the absorption and fluorescence emission spectra of different carbazole derivatives were investigated using CISD method by means of the ZINDO program at DFT optimized geometries for the quantitative prediction of the transition intensities for different substituted chemical moiety groups and length of π-bridges.

An alternative to increasing the complexity of the wave function is presented by the DFT that describes the electron correlation implicitly. Within DFT, the evolution of the system in oscillating laser field can be accurately described with real time dependent (TD) formalism.[5, 22, 23] However, approximations including the response approach are introduced in order to reduce the computational expense. In these approximations, a habitual truncation of Taylor expansion series in the powers of the field is used. Prediction of the NLO properties requires to go beyond linear response (LR), widely known as TD-DFT. Within quadratic response (QR) one can predict 2PA by calculating transition dipole moments and terminating SOS summation after the first few terms. Constrand *et al.*[24] calculated the 2PA cross-sections using DFT based on the three-state

model employing SOS formalism. The pioneering work in the calculation of 2PA cross-sections directly by QR-DFT has been done by Salek *et al.*[25] They reported the cross-sections for the small molecules calculated by DFT to be comparable to those obtained from CCSD. Later, a theoretical study on the 2PA in the conjugated organic molecules[26] which used the same QR-DFT approach was also published.

Day *et al.*[27] performed an extensive TD-DFT study of one- and two- photon absorption properties for the non-centrosymmetric chromophores. Their predicted 2PA spectra by the two-state model using LR-DFT were found to be in good agreement with the experiment. In another study,[28] they computed a closer agreement with the experiment using QR-DFT than the two-state model. The enhancement of the 2PA cross-sections[29] predicted for the porphyrin dimer relative to the monomer was in agreement we the experimental findings. However the sensitivity of the enhancement factor to the small differences in the excitation energies made the quantitative predictions of the cross-sections difficult. The applicability of the TD-DFT in the prediction of the 2PA properties for fluorine and its derivatives has been demonstrated by Zein *et al.*[30] with the Dalton code, though the excitation energies were significantly underestimated. In Hrobarikova *et al.*,[31] it is shown that the QR-DFT with the long-range corrected hybrid functional seemed to agree with the experimentally observed trends for the 2PA cross-sections, unlike the functional with a low fraction of Hartree-Fock (HF) exchange.

Another approach was chosen by Masunov and Tretiak, who used coupled-electronic oscillator (CEO) formalism in the third order.[32] This was shown to give a better agreement with experiment than the semiempirical approaches for 2PA cross-sections and especially excitation energies for large conjugated organic chromophores. Mikhailov *et al.*[33] introduced *a posteriori* Tamm-Dancoff approximation (ATDA) method, which is approximate second order TD-DFT

technique, and demonstrated the accuracy of state-to-state transition dipole moments it predicts for conjugated molecules. Good performance of TD-DFT methods, combined with the popular functionals and the modest basis sets is pleasantly surprising. It has been found that the LB94 functional ensures the correct Coulombic-asymptotic behavior and thus gives better results for polarizabilities as well as single photon excitation and photoionization spectra.[34] In a recent study,[35] LB94 has yielded good molecular orbital ionization potentials for OCS and CS_2 molecules. The results are expected to improve with the development of newer more accurate long-range-short-range corrected models of the density functionals, while preserving the computational cost.

In Chapter 2, we describe different theoretical methods employed to study the electronic structure for the set of π-conjugated organic molecules. In Chapter 3, we report the accuracy of different DFT formalisms to predict the 2PA spectra for an special class of substituted oligo (phenylene vinylenes) of donor-acceptor motifs. We also investigate the role of basis set, geometrical constraints and orbital exchange fraction on the 2PA excitation energies and cross-sections. In Chapter 4, different semiempirical methods are applied to the 2PA prediction of the same set of molecules. These studies help in the explorations of the accurate theoretical method for the prediction of 2PA properties.

1.3 Spatial Confinement of Electronic Excitations

Charged excitations like polarons and neutral singlet and triplet excitations are responsible for electronic transport in organic π-conjugated polymers. These polymers find a variety of applications in optical devices such as organic light emitting diodes,[36-38] solar cells,[38-40] lasers,[41-43] photovoltaic cells[44-46] and field-effect transistors.[47-49] The performance of these

devices is determined by the charge carrier energetics and transport properties between the donor and the acceptor molecules in semiconducting polymer materials.[50, 51] For instance, the oppositely charged carriers (holes and electrons) form the weakly bound neutral pairs in a light-emitting diode (Figure 1.2) if the Coulombic attraction between them exceeds their thermal energy. These pairs then dissociate radiatively or nonradiatively to form singlet or triplet neutral excitons giving rise to the device electroluminescence or electro-phosphorescence, respectively.[52, 53] On the other hand, the light absorption in a photovoltaic cell (Figure 1.3) results in the formation of the neutral excited states at the heterojunctions which then dissociate into the photo-generated holes and electrons producing the photocurrent.[54, 55] Investigations are being carried out to understand the operation of these devices, governed by the nature of the photoexcitations and the injection, transport and recombination of charge carriers in the organic conjugated materials.[56] Three kinds of excitation processes play a vital role in the development of organic optoelectronics:[57] charge transfer by an electron or a hole (polarons) in the polymer and excitonic energy transfer following the recombination of electron and hole producing singlet and triplet excitations. The determination of the spatial extent of their structural and electronic wavefunction is vital for the detailed knowledge of the dynamics of the excitonic states.[58-62] Therefore, a detailed understanding of the role of neutral and charged excitations in the mechanism of the intense electroluminescence and charge transport[63] is critical for improving the efficiency of these polymer-based devices. It is, however, necessary to investigate the ultrafast relaxation processes required in understanding the interplay between the efficient nonradiative transfer between excited states and the exciton dissociation into free electrons and holes (polarons) giving rise to the photocurrent in semiconducting polymers.[45, 64]

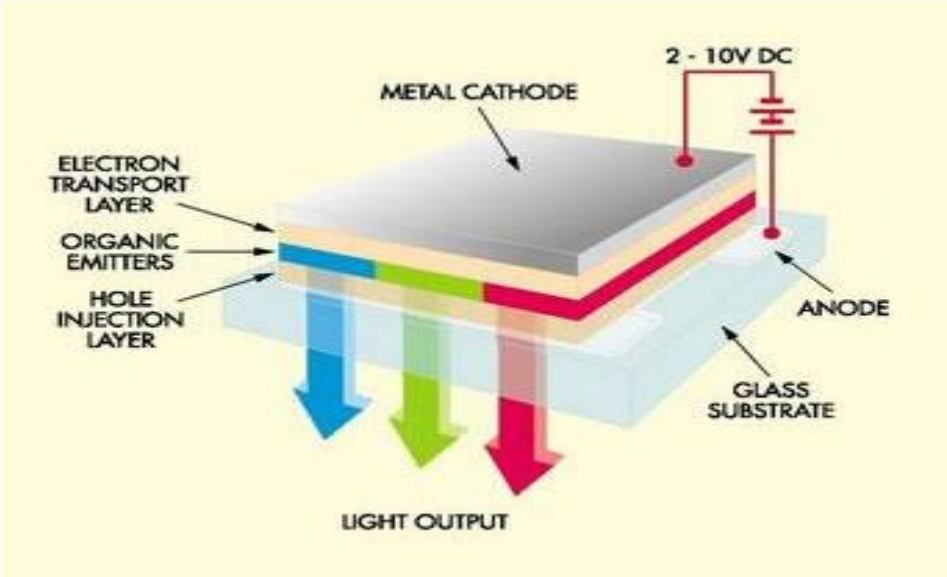

Figure 1.2: An organic light emitting diode.
(Source: www.msu.edu/~bibbing2/hdtutorial/futuretech.html)

Amongst all the organic polymers, the photophysical properties of PPV [poly (p-phenylene vinylene)] and its derivatives MEH-PPV have been extensively studied due to their high luminescence efficiency, mechanical flexibility, low cost and facile processing.[65-67] The extremely long spin coherence times owing to their weak intermolecular spin-orbit interaction of *van der* Waals type and small hyperfine field makes them favorable for studying the extension and migration of the electrically or photo-generated neutral and charged states within these systems.[65, 68] In addition, the easy availability of the spectroscopic measurements and experimental evidence[64, 69, 70] of self-localization in these polymers can be further exploited to explore the underlying physics of the spin coupling and spintronics[71] using computational quantum chemistry.

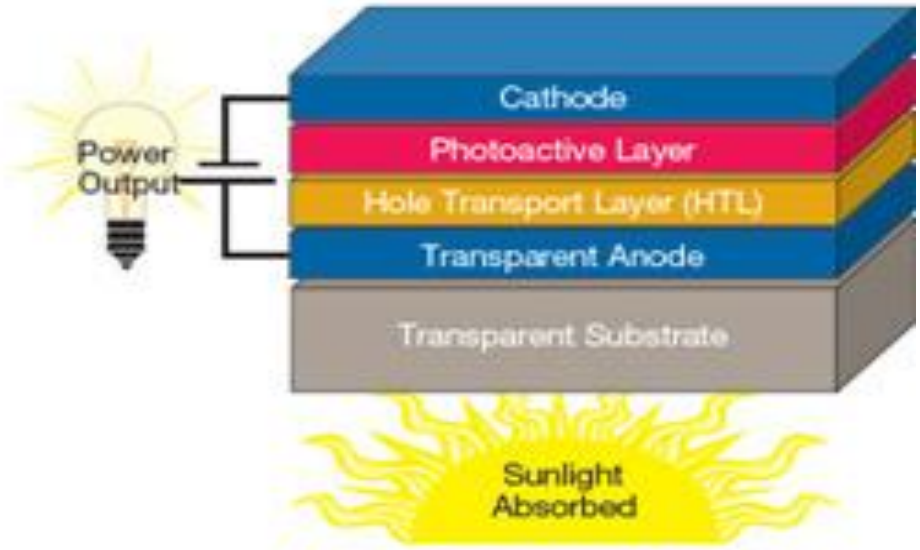

Figure 1.3: An organic photo-voltaic cell.
(Source: www.nenmore.blogspot.com/2011/04/organic-pv-market.html)

Earlier investigations on charged excitations in polythiophenes have shown that the unrestricted HF (uHF) method is not suited for studying open-shell π-conjugated systems due to inherent spin contamination.[72] The restricted open shell HF (roHF) calculations performed on thiophene oligomer radical cations exhibited localized character of the polaronic defects.[72, 73] For comparison, a generalized gradient approximation (GGA) functional, BLYP used within the unrestricted Kohn-Sham (uKS) scheme was unable to produce charge localization.[72] In a study by Zuppiroli *et al.*,[74] pure DFT overestimated the charge delocalization, whereas the semi-empirical (AM1) calculations were successful in describing the polaronic character of the charged carriers. In contrast, hybrid DFT calculations with 50% of the orbital exchange component yielded a localized polaron.[75] Time-dependent DFT (TD-DFT) calculations of PPV oligomers emphasized the importance of hybrid component in the functional model for correct description of excitonic properties.[76, 77] Semiempirical calculations of singlet excitons provided a detailed analysis of exciton dynamics and self-trapping in PPV and polyfluorenes.[78, 79]

The diffusion and mobility properties for excitons and polarons in substituted PPVs were discussed in several experimental[80-82] and theoretical[83-86] works. Calculations have predicted the self-trapping of the electronic excitations due to vibrational relaxation.[78, 79, 87, 88] Also, neutral and charged excitation processes have been studied using TD density functional theory (TD-DFT) for determining the electro-optical properties of PPV light emitting diodes.[89] Norton *et al*.[90] studied the polarization effects on localized charge carriers using quantum mechanical/molecular mechanical (QM/MM) methods with a polarizable force field treating the environment as a dielectric continuum. However, Dykstra *et al*.[58] demonstrated, via semiempirical methods, the localization of the excitons as due to the dynamic relaxation in MEH-PPV. The range-corrected functional LC-wPBE with full orbital exchange at long range predicted polaron formation in both the presence and the absence of the polarizable medium whereas the half-and-half functional BHandHLYP produces significant localization in charged polymers only in the presence of a dielectric environment. A TD study for the excited electronic states has laid emphasis on the role played by the Coulomb interactions in the localization of the polarons and excitons.[91] Recently Sai *et al*.[92] predicted polaron formation in perfect molecular crystals by tuning the fraction of exact exchange in hybrid DFT by first principles. A previous study[93] of the impact of various theoretical methods on the geometric and electronic properties of unsubstituted oligo (phenylene vinylene) (OPV) radical cations has exposed a sensitivity on the choice of the method rather on the molecular structure. Zojer *et al*.[94] has investigated the geometry relaxation effects following the electronic excitations to locate the regions of the strongest rearrangement of the electron density in conjugated organic molecules. Further, polaron formation has been observed in the presence of a polarizing environment in a non-adiabatic study of exciton dissociation in PPV oligomers.[57] Frolov *et al*.[95] spectroscopically

investigated properties of the π-π* transitions in PPV derivatives in the photoinduced absorption bands.

All these studies performed in the past indicate two distinct origins leading to self-localization (or self-trapping) of electronic excitations in low-dimensional semiconducting polymers. First of all, distortion of molecular geometry may create a spatially localized potential energy well where the state wavefunction self-traps. Secondly, even in the absence of geometric relaxation and vibrational dynamics, the electronic excitation may become spatially confined due to energy stabilization caused by polarization effects from surrounding dielectric medium.

The dependence of the localization behavior of charged excitations on the molecular structure and distribution of the atomic charges within the polymers have been highlighted previously. [96, 97] Yang *et al.*[86] observed an asymmetry in the behavior of hole and electron traps owing to the weaker intramolecular interactions between different conjugated segments of MEH-PPV than for unsubstituted PPV. Recently, an experimental study[68] revealed substantial difference in the response of the observed hyperfine fields by the opposite charges constituting a polaron pair for MEH-PPV organic light-emitting diodes. The asymmetry in the behavior of these charges was attributed to the different number of nuclear spins interacting with them, determining their degree of localization. Hence, the electron is more tightly trapped by the polymer than the hole due to the self-trapping being inversely related to the extent of hyperfine field felt. The electron- and energy- transfer properties for the *trans* and *cis* isomers were also revealed to vary for oligo (phenylene vinylene) derivatives with various side chain substitutions.[82, 98] The fluorescence intensity of the optoelectronic devices was shown to improve by the introduction of the *cis* defects into the backbone of the PPV derivatives.[99-101] Further, in a

theoretical study,[102] the hole and electron transport properties were observed to be markedly different for *cis* conformations of PPV derivatives in comparison to the *trans* ones.

In Chapter 5, we benchmark the ability of existing DFT functional models to describe the spatial extent of self-trapped neutral and charged electronic excitations in oligo (phenylene vinylene) derivatives. We study the influence of orbital exchange fraction and polarizable dielectric environment in localizing these excitations. In Chapter 6, we perform a detailed first principle study aiming to separate the two fundamental sources of spatial localization. We analyze the interdependence between the extent of the geometrical distortion and the localization of the orbital and spin density for all the excitations. In Chapter 7, we explore the effect of various conformational distortions of weak-*trans* and strong-*cis* nature on the spatial localization of the charged excitations. All these findings are important for understanding the excited-state dynamics and charge-transfer properties of excitons and polarons in polymeric materials. It also helps to tune the photo-physical properties by understanding their structure-property correlations.

CHAPTER 2 THEORETICAL METHODS

Computational methods play a vital role in detailed description of electronic structure for molecular and condensed matter. Over the last decades, various theoretical approaches have been applied to the prediction as well as the interpretation of the experimental measurements of various properties of the π-conjugated organic molecules. The most relevant of these approaches are briefly reviewed in the following sections and make use of well-defined approximations to a multi-electron Schrödinger equation as described below. The electronic states of a many-body system can be often described within Born-Oppenheimer approximation in which the atomic nuclei are assumed to be classical and the electrons moving in their static potential.[103, 104] The electronic Schrödinger equation is then

$$\hat{H}\,\Psi = E\Psi \tag{2.1}$$

Here $\Psi(\vec{r}_1,.....,\vec{r}_N)$ is the wavefunction describing the stationary electronic state, *N* is the number of electrons and $\hat{H}$ is the electronic molecular Hamiltonian given as

$$\hat{H} = \left[\hat{T}+\hat{V}+\hat{U}\right] = \left[\sum_i^N -\frac{\hbar^2}{2m}\nabla_i^2 + \sum_i^N V(\vec{r}_i) + \sum_{i<j}^N U(\vec{r}_i,\vec{r}_j)\right] \tag{2.2}$$

where $\hat{T}$ is the *N*-electron kinetic energy, $\hat{V}$ is the *N*-electron potential energy in the external field and $\hat{U}$ is the electron-electron interaction energy for *N*-electron system. Out of these three operators, $\hat{V}$ is system dependent while both $\hat{T}$ and $\hat{U}$ depend only on electron distribution. There are many sophisticated methods for solving the many-body Schrödinger equation based on the expansion of the wavefunction in Slater determinants.

The simplest electronic wavefunction is introduced in the mean field approximation known as the Hartree-Fock (HF) theory. In this approximation, each electron is assigned a wave function called a molecular orbital (MO) shaped by the mean field created by the density distribution of all other electrons. The total electron wavefunction is expressed as an antisymmetrized product (called Slater determinant) of these MOs. Electron interaction $\hat{U}$ is then composed of two terms: classical Coulomb energy and exchange energy E_X^{HF}, resulting from the quantum nature of electrons. Single Slater determinants are used for the description of electronically excited states in similar manner. Electron correlation part of $\hat{U}$ is missing from this picture, making mean field approximation inaccurate for the spectroscopic purposes.

2.1 Wavefunction Theory (WFT) Methods

A wavefunction theory (WFT) description of the molecular excited states starts with MOs optimized in a self-consistent field (SCF) procedure with a single Slater determinant wavefunction of the ground state known as restricted HF (rHF) method. Therefore, excited states can also be described by single determinants built on the reoptimized MOs for a specific state, with an imposed constraint that this excited state determinant is orthogonal to Slater determinants of the ground and lower lying excited states. However, searching for the wavefunction in the form of linear combination of these single determinants built on the ground state MOs was found to be technically preferable alternative to state-specific MO optimization. This alternative is known as CI, and is widely used. In CI method, one or more orbitals in the HF determinant are substituted with unoccupied orbitals to form “excited configurations”. Then wavefunction of the system is expressed as a linear combination of these configurations, and

electronic states are found by diagonalization of the Hamiltonian. All possible substitutions in the HF determinant yield the full CI (FCI) method. It gives an exact solution to the Schrödinger equation for a given atomic basis. The exponential growth of the computational effort with the size of the system makes FCI attainable only for very small molecular systems, and for practical reasons various truncation schemes are introduced. The single or double excited states can be approximately described by a Slater determinant where respectively one or two ground state MOs are substituted with the vacant HF orbitals. However, more accurate description is obtained when the wavefunction is built as a linear combination of several single (or single and double) substituted determinants. These approach are known as CIS (and CISD), and are widely used. The MOs that can be used for substitution are often limited to so called "active space". An approximation, labeled CISd, consists of limiting the active orbital space, where double substitutions are performed. When all (not just single and double) substitutions within a small active space are included in the wavefunction, the method is called the complete active space CI (CASCI). When CASCI wavefunction is used instead of HF reference, and single and double substitutions from this reference are included in the wavefunction variationally, it is called multi-reference single and double CI (MRCI).

2.2 Semiempirical Hamiltonians

The methods described in the previous section may be highly accurate; however they are computationally expensive and become intractable when applied to the molecules of practical interest. For this reason, various semiempirical Hamiltonians (AM1, PM6, INDO, ZINDO/1, ZINDO/S) had been used in combination with WFT methods. As a result of semiempirical

parameterization, the accuracy varied from one class of the materials to another, and at best only the quantitative picture is obtained.

Below we detail Zerner's Intermediate Neglect of Differential Overlap (ZINDO) formalism as a representative example. ZINDO is an extension of INDO semiempirical Hamiltonian.[105, 106] First one seeks the solutions of the HF equations in the form

$$F^k C^k = \Delta C^k \varepsilon^k \tag{2.3}$$

where the superscript k either designates α or β spin, F is the Fock or energy matrix, Δ the overlap matrix,

$$\Delta_{\mu\nu} = \langle \mu | \nu \rangle = \left\langle X^{\mu} \middle| X^{\nu} \right\rangle = \delta_{\mu\nu} \tag{2.4}$$

$\boldsymbol{\varepsilon}$ is the diagonal matrix of MO energies; and C is a square matrix the columns of which are the MO coefficients.

$$\left(\Phi_1, \Phi_2, ..., \Phi_n\right) = \Phi = XC \tag{2.5}$$

Here, Φ is a row matrix of MOs and X is a row matrix of atomic orbitals. The basic parameters for this model are expressed with a single Fock operator with no loss in generality.

$$F^k_{\mu\nu} = \beta_{\mu\nu} - P^k_{\mu\nu}\gamma_{\mu\nu} + \Delta G^{AB}_{\mu\nu} \qquad \mu \neq \nu \tag{2.6}$$

$$\beta^{AB}_{\mu\nu} = \overline{S}_{\mu\nu}\left(\beta^A_{\varpi} + \beta^B_{\mu}\right)/2 \tag{2.7}$$

$$\Delta G^{AB}_{\mu\nu} = \left\{ \sum_{\sigma,\lambda}^{A} \left[P_{\sigma\lambda}\left(\mu\nu|\sigma\lambda\right) - Pk_{\sigma\lambda}\left(\mu\sigma|\nu\lambda\right) \right] + P^k_{\mu\nu}\gamma_{\mu\nu} - \sum P_{\sigma\sigma}\gamma_{\mu\sigma}\delta_{\mu\nu} \right\} \delta_{AB} \tag{2.8}$$

P is the first-order density matrix with the elements given by

$$P^k_{\mu\nu} = \sum_{a}^{MO} N^k_a C_{\mu A} C_{\nu A} \tag{2.9}$$

with N_a^k = 0 or 1, the occupancy of the a^{th} MO in the k^{th} shell. The only pure empirical parameter introduced to correct for the neglect of integrals are the resonance integrals β_μ^A of Equation 2.7. $\overline{S}_{\mu\nu}$ is related to the overlap matrix $\Delta_{\mu\nu}$.

$$\overline{S}_{\mu\nu} = \sum f_{l,m} g_{l.m} \Delta_{\mu(m)\nu(m)} \tag{2.10}$$

in which $f_{l,m}$ are the Eulerian transformation matrices required to transform the orbitals from the localized coordinate system to the molecular system, $g_{l,m}$ are empirical factors to better order the σ and π type orbitals, and $\Delta_{\mu(m)\nu(m)}$ are the σ or π or δ components of the overlap integrals in the local system, where appropriate. They may be empirically adjusted to fit the experimental data, and the most important ones for the π-conjugated systems are Slater-Condon factors for ($g_{1,\sigma}$) p-type σ orbitals and ($g_{1,\pi}$) p-type π orbitals.

2.3 Density Functional Theory (DFT) Methods

Density functional theory (DFT) involves the first principle approach to solve Schrödinger equation and an alternative to WFT methods described above.[107, 108] It is widely applicable tool to study the ground state properties of many-body systems. Within DFT, the ground state of the system with correlated electrons is described similar to HF equations. Unlike semiempirical methods, no overlap is assumed to be zero, but the exchange integrals in Equation 2.3 are replaced (completely or partly) with electron-density dependent expressions, derived in Fermi uniform electron gas model (local density approximation, LDA), or their gradient-dependent improvements (general gradient approximation, GGA). After such a replacement, Fock Hamiltonian is called Kohn-Sham (KS) Hamiltonian, and MOs are called KS orbitals. The key variable here is the particle density given by

$$n(\vec{r}) = N\int d^3r_2 \int d^3r_3 .....\int d^3r_N \Psi(\vec{r},\vec{r}_2,.....,\vec{r}_N)\Psi(\vec{r}_1,\vec{r}_2,.....,\vec{r}_N) \tag{2.11}$$

It is possible to calculate the ground-state observables using this density, in particular, ground-state energy E_0, which is also a functional of n_0

$$E_0 = E[n_0] = \langle \Psi[n_0] | \hat{T} + \hat{V} + \hat{U} | \Psi[n_0] \rangle \tag{2.12}$$

And the final energy can be minimized as

$$E[n] = T[n] + U[n] + \int V(\vec{r}) n(\vec{r}) d^3r \tag{2.13}$$

The Kohn-Sham equations[109] to solve for non-interacting particles, are given by

$$\left[-\frac{\hbar^2}{2m}\nabla^2 + V_s(r) \right] \phi_i = \varepsilon_i \phi_i \tag{2.14}$$

$$n(\vec{r}) = \sum_i |\phi_i(r)|^2 \tag{2.15}$$

which yields the orbitals ϕ_i and effective single-particle potential V_s as

$$V_s(\vec{r}) = V(\vec{r}) + \int \frac{e^2 n_s(\vec{r}')}{|\vec{r} - \vec{r}'|} d^3r' + V_{XC}[n_s(\vec{r})] \tag{2.16}$$

Here, the second term denotes the so-called Hartree term describing the electron-electron Coulomb repulsion, while the last term V_{xc} is called the exchange-correlation (XC) potential, which replaces exact exchange in HF method and includes all the many-particle interactions.

Complete replacement, introducing electron correlation interactions, corresponds to so-called "pure" DFT, and partial replacement retaining a fraction of HF exchange, is called "hybrid" DFT. This fraction can vary with electron-electron distance, which is known as "range-separated hybrid", variations including long-range corrected and coulomb-attenuated hybrids. The expression replacing HF exchange is known as XC functional given as

$$E_{XC} = aE_X^{HF} + (1-a)E_X^{GGA} + E_C^{GGA} \tag{2.17}$$

where *a* is the fraction of HF exchange in the XC functional. The long range corrected functionals behave as typical hybrid or GGA at short range. However they have increasing HF components at longer distances up to a maximum value of 100%.

2.3.1 Linear Response Time-Dependent TD-DFT

Time-dependent DFT (TD-DFT) is analogous to DFT in replacing wave function with the density, except this time the excited states can be described.[110, 111] Once the stationary ground state system of correlated electrons is described by KS orbitals, the evolution of the system in oscillating laser field can be described with real time dependent formalism. The corresponding KS equations in TD-DFT are written as

$$\left[-\frac{\hbar^2}{2m}\nabla^2 + \upsilon_s(r,t)\right]\phi_i(r,t) = i\frac{\partial}{\partial t}\phi_i(r,t) \tag{2.18}$$

$$n_s(r,t) = \sum_{i=1}\left|\phi_i(r,t)\right|^2 \tag{2.19}$$

Approximations including the response approach are often introduced in order to reduce the computational expense. In these approximations, one truncates Taylor expansion series for the equations of motion for the single electron density matrix ρ(t) in the powers of the field.

$$i\frac{\partial\rho(t)}{\partial t} = \left[F(\rho),\rho\right] - \zeta(t).\left[\mu.\rho\right] \tag{2.20}$$

Often only the first order is retained, an approximation known as linear response (LR) time-dependent DFT or just TD-DFT. Prediction of NLO properties requires going beyond LR-DFT.

For instance, in quadratic response (QR) one can predict two photon absorption (2PA) by calculating transition dipole moments and restricting SOS summation by the lowest few states.

Unlike the WFT methods, adiabatic TD-DFT in the KS approximation may be computationally efficient method for studying the optical response of molecules. This method is based on the response of one-electron density matrix to an external field. When equations of motion are solved in the first order in external field (LR), their solutions yield the excitation energies and ground to excited state transition dipoles. Preserving the terms describing the response up to the second order in external field (QR), is required to obtain the permanent dipole moments of excited states as well as state-to-state transition dipoles.

In linear approximation, the equation of motion is reduced to a non-Hermitian eigenvalue problem as follows

$$\begin{bmatrix} A & B \\ -B & -A \end{bmatrix} \xi = \Omega \xi \,;\; \xi = \begin{bmatrix} \hat{X} \\ \hat{Y} \end{bmatrix} \tag{2.21}$$

Excitation energies Ω_α and transition density matrices ξ_α for ground to excited state transitions are its solutions. In the basis of occupied (i,j) and vacant (a,b) KS orbitals of σ,τ subsets (σ,τ = α,β), transition density is block-diagonal with occupied-vacant $X = (\xi)_{ia}$ and vacant-occupied $Y = (\xi)_{ai}$ blocks being nonzero. Matrices A and B are defined as

$$A_{ai\sigma,bj\tau} = \delta_{ab}\delta_{ij}\delta_{\sigma\tau}(\varepsilon_a - \varepsilon_i) + K_{ai\sigma,bj\tau}\,,\; B_{ai\sigma,bj\tau} = K_{ai\sigma,jb\tau} \tag{2.22}$$

For the hybrid DFT with c_{HF} fraction of HF exchange, the coupling matrix K is expressed through the second derivative of XC functional w, Coulomb and exchange integrals as

$$K_{ai\sigma,bj\tau} = (1 - c_{HF})(ia \mid w \mid jb) + (ia \mid jb) - c_{HF}\delta_{\sigma\tau}(ab \mid ij) \tag{2.23}$$

The matrix A consists of interactions between two singly-excited configurations $(a \leftarrow i \,|\, H \,|\, b \leftarrow j)$, also known as CIS Hamiltonian. The matrix B includes, by virtue of swapping indexes, the excitations from virtual to occupied molecular orbitals (deexcitations) of the form $(a \leftarrow i \,|\, H \,|\, j \leftarrow b)$. Mathematically, they are equivalent to the matrix elements between the ground and the doubly excited states.[112] Thus, LR-DFT accounts for double excitations implicitly through the XC functional and explicitly through the deexcitation matrix B. The transition dipole moments between the ground and the excited states are easily obtained using LR-DFT as a convolution of the dipole moment operator μ with transition densities ξ_α

$$\mu_{0,\alpha} = Tr(\mu \xi_\alpha) \tag{2.24}$$

However, the analytical expressions for the state-to state transition dipoles and the permanent dipoles of the excited states do not appear in this formalism. Though, the permanent dipole moments can be evaluated numerically, by performing two sets of LR-DFT calculations at different values of the external electric field.

2.3.2 Nonlinear Response Time Dependent TD-DFT

The challenges in theoretical prediction of the NLO properties are routed in the increasing importance of the electron correlation for description of excited states, often making prediction of their properties inaccurate. There are at least three distinct DFT formalisms which can be used to calculate these second order properties (state-to-state transition and permanent dipoles of excited states). In the subsequent subsections, we shall be briefly discussing these formalisms, including coupled-electronic oscillator (CEO), *a posteriori* Tamm-Dancoff

approximation (ATDA) and quadratic response (QR). We will detail each of these approaches below.

2.3.2.1 Coupled-Electronic Oscillator (CEO) Formalism

In CEO formalism,[113, 114] the Hamiltonian-Liouville classical equations of motion for the density matrix are solved. Anharmonic coupling terms between LR excitations constitute the transition dipoles between the excited states and are expressed as explicit summations over these states. The CEO approach is equivalent to the TD-DFT method in the LR approximation.

When terms up to the second order in external field are retained in the equations of motion, the transition densities obtained at the first-order CEO are used as the basis to solve them. In addition to the LR states α, their combinations αβ, known as doubly excited states, also appear in the second order formalism.[113] Their excitation energies are equal to the sum of the single excitations as

$$\Omega_{\alpha\beta} = \Omega_\alpha + \Omega_\beta \tag{2.25}$$

and the transition densities are the products of single excitation densities $\xi_\beta \xi_\alpha$. The second order CEO gives the transition dipole between the ground and this doubly excited state as

$$\mu_{0,\alpha\beta} = \sum_{\alpha\beta}^{perm} Tr(\mu(I-2\rho)\xi_\alpha\xi_\beta) + \sum_{\gamma>0}\left(\frac{V_{\alpha\beta-\gamma}\mu_\gamma}{\Omega_\alpha+\Omega_\beta-\Omega_\gamma} - \frac{V_{\alpha\beta\gamma}\mu_{-\gamma}}{\Omega_\alpha+\Omega_\beta+\Omega_\gamma}\right) \tag{2.26}$$

Here the first summation runs over symmetrized permutations of the indexes, I is the identity matrix, ρ is ground state density matrix, and $V_{\alpha\beta\text{-}\gamma}$ is the XC coupling term, expressed via KS operators $V(\xi)$ on transition densities

$$V_{\alpha\beta-\gamma} = \frac{1}{2}\sum_{\alpha\beta\gamma}^{perm} Tr((I-2\rho)\xi_\alpha\xi_\beta V(\xi_\gamma)) \tag{2.27}$$

Further, the transition dipole between a doubly excited state and any other excited state is zero unless the other state represents one of the components of this doubly excited state

$$\mu_{\alpha,\alpha\beta} = \mu_{0,\beta}\,,\ \mu_{\alpha,\beta\gamma} = 0 \tag{2.28}$$

The transition dipole between two singly excited states is

$$\mu_{\alpha,\beta} = \mu_{-\alpha\beta} + \sum_{\gamma>0}\left(\frac{V_{-\alpha\beta-\gamma}\mu_{\gamma}}{-\Omega_{\alpha}+\Omega_{\beta}-\Omega_{\gamma}} + \frac{V_{\alpha-\beta-\gamma}\mu_{-\gamma}}{\Omega_{\alpha}-\Omega_{\beta}-\Omega_{\gamma}}\right) \tag{2.29}$$

and the permanent dipole of the excited state α (less permanent dipole of the ground state) is

$$\Delta\mu_{\alpha} = \mu_{-\alpha\alpha} + \sum_{\gamma>0}\left(\frac{V_{-\alpha\beta-\gamma}\mu_{\gamma}}{-\Omega_{\gamma}} + \frac{V_{\alpha-\beta-\gamma}\mu_{-\gamma}}{-\Omega_{\gamma}}\right) \tag{2.30}$$

where

$$\mu_{-\alpha\beta} = \sum_{-\alpha,\beta}^{perm} Tr(\mu(I-2\rho)\xi_{\alpha}^{*}\xi_{\beta}) \tag{2.31}$$

Thus, linear excitations remain unchanged in this formalism and combined states $\xi_{\beta}\xi_{\alpha}$ of doubly excited nature are added as a second order response.

2.3.2.2 *a posteriori* Tamm-Dancoff Approximation (ATDA) Formalism

a posteriori Tamm-Dancoff Approximation (ATDA) to the second order CEO was introduced in Ref.[33] in order to simplify implementation and reduce the computational expense. It will be described in the following.

TDA[115, 116] is a well-known approximation introduced in LR formalism which consists in neglecting the deexcitation matrix *B* in the non-Hermitian eigenvalue equation (Equation 2.21).

With this approximation, the equation is then simplified to the form as

$$\begin{bmatrix} A & 0 \\ 0 & -A \end{bmatrix} \begin{bmatrix} \hat{X} \\ \hat{Y} \end{bmatrix} = \Omega \begin{bmatrix} \hat{X} \\ \hat{Y} \end{bmatrix} \Rightarrow A\hat{X} + A\hat{Y} = \Omega\hat{X} + \Omega\hat{Y} \tag{2.32}$$

and also called the CIS equation when applied to the HF ground state. Its solution yields the excitation energies Ω_α and transition density matrices ξ_α. These excitation energies are typically higher than the ones obtained by solution of the full LR equation (Equation 2.21). The double excitation character is included in the TDA formalism only implicitly through the approximate XC potential. The TDA description of the excited states was found to be more accurate.[117] In TDA, the state-to-state transition dipoles $\mu_{\alpha,\beta}$ and differences between the permanent and ground state dipole moments ($\Delta\mu_\alpha = \mu_{\alpha,\alpha} - \mu_0$) are readily available as

$$\mu_{\alpha,\beta} = Tr(\mu(I - 2\rho)\xi_\alpha^* \xi_\beta) \tag{2.33}$$

$$\Delta\mu_\alpha = Tr(\mu(I - 2\rho)\xi_\alpha^* \xi_\alpha) \tag{2.34}$$

However, ATDA[33] corresponds to the annihilation of the Y component of the transition density in the TDA equation (Equation 2.32) and then represented as

$$A\hat{X} = \Omega\hat{X} \tag{2.35}$$

In ATDA, excitation energies and ground to excited transition dipoles remain identical to those of the full LR-DFT, while Equation 2.33 is used to obtain state-to-state transition dipole moments and Equation 2.34 is used to obtain the permanent dipole moments of the excited states. TDA does not contain doubly excited states in its manifold of states. These are added to the manifold of states of ATDA, characterized by the excitation energies from Equation 2.25 and the transition dipoles

$$\mu_{0,\alpha\beta} = Tr(\mu(I-2\rho)\xi_\alpha\xi_\beta),\ \mu_{\alpha,\alpha\beta} = \mu_\beta,\ \mu_{\alpha,\beta\gamma} = 0 \qquad (2.36)$$

Thus, we observe the neglect of XC coupling terms $V_{\alpha\beta\text{-}\gamma}$ as an approximation to the second order CEO. Henceforth, ATDA is intermediate between TDA and the full second order CEO. In Ref.,[33] the accuracy of the transition dipole moments predicted with ATDA, compared to *ab initio* values was demonstrated. However the accuracy of the ATDA predictions of 2PA cross-sections was not yet systematically benchmarked, until now.

2.3.2.3 Quadratic Response (QR) Formalism

In QR-DFT formalism, the single (SR) and double residues (DR) of the QR function at the resonant frequencies can be used to determine the 2PA matrix elements directly or via SOS. These approaches allow one to calculate the expectation value of one operator in the presence of the perturbation operators.

2.3.2.3 (a) Quadratic Response Single Residue (QRSR)

This quadratic approximation uses the states obtained in the LR approximation as the basis, and involves summation over infinite number of these states implicitly. The resonant two-photon transition probability δ(ω) for each of the excited states is calculated as a single residue at the singularity (pole) of the QR function $\langle\langle \mu^a; \mu^b, \mu^c \rangle\rangle_{-\omega_b\omega_c}$,[26, 118]

$$\lim_{\omega_c \to \omega_Y} (\omega_c - \omega_Y)\langle\langle \mu^a; \mu^b, \mu^c \rangle\rangle_{-\omega_b\omega_c} = -\sum_X \left[\frac{<0|\mu^a|X><X|\mu^b - <0|\mu^b|0>|Y>}{(\omega_{0X} - (\omega_{0Y} - \omega_{0b}) - i\Gamma_{X0}} \right.$$

$$\left. + \frac{<0|\mu^b|X><X|\mu^a - <0|\mu^a|0>|Y>}{(\omega_{0X} - \omega_{0b}) - i\Gamma_{X0}} \right] \langle Y|\mu^c|0\rangle \qquad (2.37)$$

$$\lim_{\omega_c \to \omega_Y} (\omega_c - \omega_Y)\langle\langle \mu^a ; \mu^b, \mu^c \rangle\rangle_{-\omega_b \omega_c} = \delta(\omega)\left\langle Y \mid \mu^c \mid 0 \right\rangle \tag{2.38}$$

Here $\langle\langle \mu^a ; \mu^b, \mu^c \rangle\rangle_{-\omega_b \omega_c}$ is the μ^a, μ^b and μ^cth component of the electric dipole hyperpolarizability tensor at frequencies ω_b and ω_c. However μ^a, μ^b and μ^c represent the dipole moment operator for the homogenous electric field of frequencies ω_a, ω_b and ω_c, respectively. |0> is the ground state, |X> and |Y> are 1PA and 2PA states respectively and Γ_{X0} is the damping constant. $\delta(\omega)$ is obtained with a QRSR run which is then substituted in the SOS expression[119] to obtain the 2PA cross-section at resonance ($\omega_{Y0} = 2\omega$). The expression for the cross-section simplifies to the form as

$$\sigma^{(2)}(\omega) = \frac{4\pi^3 \omega^2 \delta(\omega)}{15 c^2 n^2} g_Y(2\omega) \tag{2.39}$$

2.3.2.3 (b) Quadratic Response Double Residue (QRDR)

Double residues of the QR function[118] $\langle\langle \mu^a ; \mu^b, \mu^c \rangle\rangle_{-\omega_b \omega_c}$ are evaluated at the poles as

$$\lim_{\omega_b \to \omega_X} \left[\lim_{\omega_c \to \omega_Y} (\omega_c - \omega_Y)\langle\langle \mu^a ; \mu^b, \mu^c \rangle\rangle_{-\omega_b \omega_c} \right] (\omega_b - \omega_X) =$$

$$- < 0 \left| \mu^b \right| X >< X \mid \mu^a - < 0 \mid \mu^a \mid 0 > \mid Y > \left\langle m \mid \mu^c \mid 0 \right\rangle \tag{2.40}$$

The transition dipoles between excited states |X> and |Y> are obtained with the QR function (Equation 2.38).

The calculated transition dipole values are used in the SOS expression[119] for the calculation of 2PA cross-sections.

$$M^Y_{\alpha\beta} = \frac{1}{2\hbar} \sum_X \frac{< Y \left| \mu_\alpha \right| X >< X \left| \mu_\beta \right| 0 >}{\left(\omega_{0X} - \frac{\omega_{0Y}}{2} \right) - i\Gamma_{X0}} + \frac{< Y \left| \mu_\beta \right| X >< X \left| \mu_\alpha \right| 0 >}{\left(\omega_{0X} - \frac{\omega_{0Y}}{2} \right) - i\Gamma_{X0}} \tag{2.41}$$

where $M_{\alpha\beta}$ corresponds to the two-photon transition matrix element, α and β run over x, y and z spatial directions. Here, the ground state is represented by |0> whereas 1PA and 2PA excited states by |X> and |Y>, respectively. The factor $\left(\omega_{0X} - \frac{\omega_{0Y}}{2}\right)$ is called the detuning between the 1PA state and the virtual state midway in energy between the ground and 2PA state and Γ_{X0} is the damping constant (taken to be 0.1eV). The transition (X≠Y) and permanent (X=Y) dipole between X and Y excited states is defined as

$$<Y|\bar{\mu}_\alpha|X> = <Y|\mu_\alpha|X> - <0|\mu_\alpha|0>\delta_{YX} \tag{2.42}$$

The orientationally averaged 2PA cross-section for linearly polarized beam is then computed by substituting the transition matrix components obtained from SOS expression[119] (Equation 2.41) in the formula given as

$$\sigma^{(2)}(\omega) = \frac{16\pi^3\omega^2}{15c^2n^2}\sum_Y^{x,y,z}\sum_\beta^{x,y,z}\sum_\alpha^{x,y,z}(M^Y_{\alpha\alpha}M^Y_{\beta\beta}{}^* + 2M^Y_{\alpha\beta}M^Y_{\alpha\beta}{}^*)\,g_Y(2\omega) \tag{2.43}$$

Here $\omega = \frac{\omega_{0Y}}{2}$ and $g_Y(2\omega)$ is the lorentzian line shape function given by

$$g_Y(2\omega) = \frac{1}{\pi}\frac{\Gamma_{Y0}}{(\omega_{Y0} - 2\omega)^2 + \Gamma_{Y0}^2} \tag{2.44}$$

The linewidth Γ_{Y0} accounts for the experimentally observed homogeneous and inhomogeneous broadening and usually taken as an empirical constant (0.1eV in our calculations). The specific choice of the damping constant Γ_{X0} and the lorentzian line shape function Γ_{Y0} was suggested in an experimental study,[120] for the same family of molecules, and had been used in the previous CEO studies performed on these molecules.[121] We used the same linewidth in order to be consistent in the comparison of the 2PA cross-sections calculated with all different DFT formalisms. The use of the uniform damping constant is admittedly the simplest way to account

for experimentally observed inhomogeneous lineshape broadening, which is typically in the order of 0.1 eV (owed to various factors affecting both 1PA and 2PA spectra). Thus, the proper choice of this parameter should roughly reproduce experimentally observed linewidths. However, the main purpose of using the empirical broadening is not to achieve the optimal comparison with experiment in terms of the absolute magnitudes of nonlinear response, but to better analyze the profiles of experimental spectra to identify the essential electronic states contributing to the response. The optimal parameters are molecule-specific and dependent on solvent, energy interval, type of spectra, lineshape profile (e.g., Gaussian or Lorentzian), *etc*. A proper accounting of vibronic progression, including non-Condon effects, is numerically demanding but feasible, it produces improved description of the gas-phase 2PA spectra.[122] On the other hand, the solvent dependence of the lineshapes can be captured by averaging over representative snapshots of molecular dynamics trajectories,[123, 124] which is also computationally demanding when done at DFT level of theory. Both methods expand beyond the scope of the present work, but can be used in the future studies.

Substitution of the LR values in place of dipoles evaluated with the exact states leads to summation over large number of states, similar to the CEO formalism. However, in QR-DFT this explicit summation is replaced by iterative solution of the linear equations[118], which may be recast[125] in a form, similar to Equation 2.21. Although the response formalism is general enough to describe the higher order corrections to the excitation energies obtained from the LR approximation, to the best of our knowledge this was never attempted.

Thus, the SOS formalism can be combined with ATDA or QRDR methods to calculate the second hyperpolarizabilities and 2PA cross-sections. SOS requires the explicit calculation of permanent and transition dipole moments. It is more general, straightforward and amenable to

easy interpretation. In QRSR, on the other hand, the complete manifold of excited states from LR is taken into account (as opposed to necessarily truncated SOS series). CEO also includes the truncation, but the doubly excited states that appear in the second order are considered along with the singly excited states from LR. ATDA inherits these doubly excited states from the second order CEO.

CHAPTER 3 PREDICTION OF TWO-PHOTON ABSORPTION SPECTRA WITH DFT METHODS

Accurate theoretical methods are becoming increasingly helpful in the design of new nonlinear optical (NLO) materials with improved one- and two-photon absorption (1PA and 2PA) properties. In this chapter, we compare the ability of various density functional theory (DFT) formalisms to predict the 2PA spectra with sufficiently useful accuracy for an important class of organic materials compared to the experimental[13, 120, 126] measurements. Molecules studied here belong to a specific class of PPV (*p*-phenylene vinylenes) derivatives substituted in donor-π-donor, donor-acceptor-donor and acceptor-donor-acceptor patterns as shown in Figure 3.1. The quadratic response (QR) methods are compared with the recently proposed[33] *a posteriori* Tamm-Dancoff approximation (ATDA) and the previously benchmarked[121] third-order coupled-electronic oscillator (CEO) results. QR is found to overestimate the cross-sections in all the cases. We trace the reasons to unreliable excited states above the ionization threshold. In addition, quadratic response lacks the double excitations so that their contributions to the 2PA spectra are redistributed over the nearest single excitations. This distorts the individual contributions to the 2PA response and affects the overall picture. For this reason, we do not recommend QR for the essential state analysis, while ATDA can be used both for the 2PA predictions and the structure-property correlations. We also study the effect of the orbital exchange fraction on the 2PA excitation energies and cross-sections. Higher exchange (BMK and M05-2X) and range-separated (CAM-B3LYP) hybrid functionals are found to yield the inaccurate predictions both quantitatively and qualitatively. The results obtained with the long-range-corrected functional LC-BLYP do not seem to be useful at all. This failure of the exchange-correlation (XC) functionals with correct asymptotic is traced to inaccurate transition

dipoles between the valence states, where functionals with low HF exchange succeed. A new cut-off procedure is proposed to compensate for the collapse of the higher-lying excited states obtained with the latter functionals. These results are discussed in detail in the upcoming sections.

3.1 Computational Details

We predict 1PA and 2PA properties by three different DFT formalisms: (a) ATDA, (b) QRSR and (c) QRDR for molecules under study and compare our results with the published[32] (d) CEO predictions. The DFT methods considered in this work were introduced in Chapter 2. In method (a) we used the developmental version of Gaussian 09 Rev. A.1[5] suite of programs modified with the code implementing ATDA method.[33] In method (b) we used Dalton 2.0[127] to calculate the 2PA directly. In method (c) we extracted ground to excited state and excited-to-excited state transition dipole moments from the linear response (LR) and QR-DFT runs of Dalton 2.0, and explicitly fed them into in-house script that implements the sum-over-state (SOS) formalism (Equation 2.41) to calculate the 2PA cross-section using Equation 2.43for given 1PA and 2PA states. For comparison of the formalisms, we only considered six singlet excited states for ATDA, three 1PA and three 2PA for QRDR and three 2PA states for QRSR as the complete manifold of 1PA states is already included implicitly in that formalism. For consistency with CEO results[32] the geometry was optimized at HF/6-31G level with planar constraint and excited states were calculated at TD-B3LYP/6-31G level. To study the effect of SOS series truncation on 2PA cross-sections, we varied the number of excited states from six to thirty for ATDA calculations.

The effect of different basis sets, geometrical constraints, optimization and excitation levels were investigated using ATDA calculations for molecules under study. To determine the effect of the larger basis set, we chose the same geometry and calculation level as used for the comparison of varied formalisms, changing it to 6-31G* from 6-31G. The change in the 2PA predictions is studied by using different optimized geometries with or without planar constraint, we used B3LYP/6-31G*//B3LYP/6-31G*, M05/6-31G*//M05/6-31G* and B3LYP/6-31G*//M05-2X/6-31G* levels. For comparison of XC functionals, we chose M05-2X/6-31G* to be the optimization level and performed the excited state calculations at HSE06[128], B3LYP[129-131], M05[132], BMK[133], M05-2X[134] CAM-B3LYP[135], LC-BLYP[136] levels. The basis set used for all these calculations was 6-31G*.

Geometries of the molecules shown on Figure 3.1 were optimized with the planar constraint possessing C_{2h} point group symmetry and those with no additional constraint belong to C_2 or C_s symmetry. According to the dipole selection rules, only B_u states are 1PA allowed and A_g states are 2PA allowed for planar geometries of C_{2h} symmetry, whereas for molecules belonging to the C_s symmetry group, the A_u states are 1PA allowed and A_g are forbidden (2PA allowed). The n-butyl and dodecyl group in the molecules studied experimentally were replaced by methyl group. In preliminary calculations we included the solvent effects (toluene) using polarizable continuum model (PCM), but found almost no effect on the 2PA cross-section values. This could be attributed to the centrosymmetric geometry of the molecules studied with zero dipole moments for both ground and excited states. For this reason, we do not report the results obtained with PCM in this study.

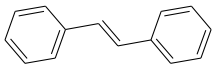	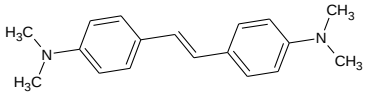
(1)	**(2)**
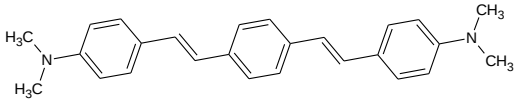	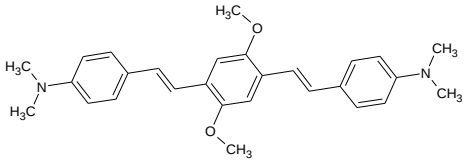
(3)	**(4)**
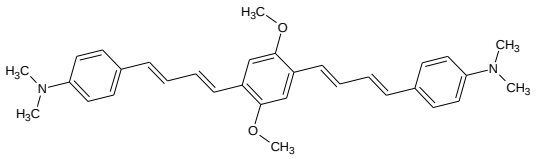	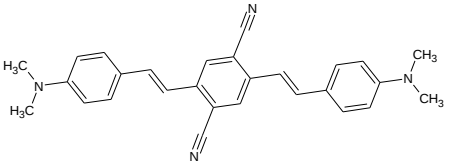
(5)	**(6)**
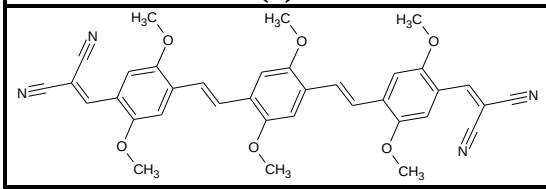	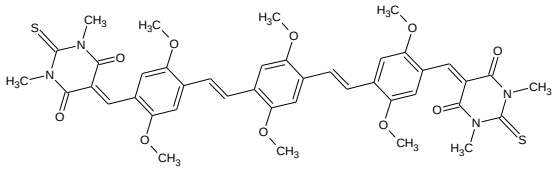
(7)	**(8)**
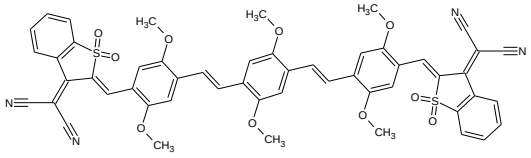	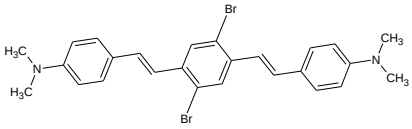
(9)	**(10)**
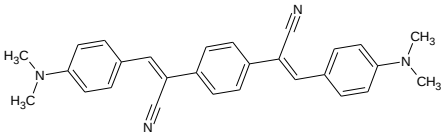	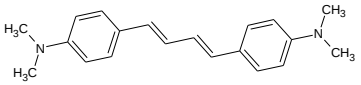
(11)	**(12)**
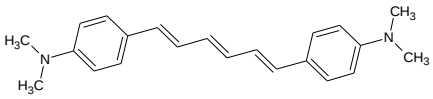	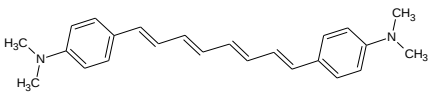
(13)	**(14)**
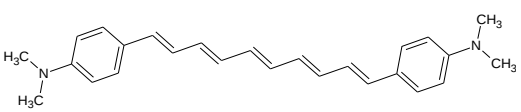	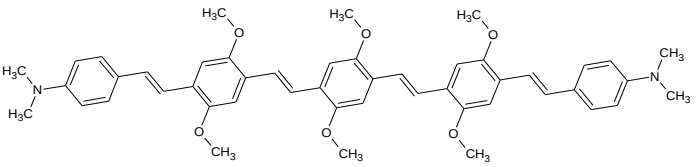
(15)	**(16)**

Figure 3.1: Molecules studied in this work.

3.2 Excitation Energies

Our TD-DFT predictions for 1PA and 2PA transition energies are presented in Tables 3.1, 3.2 and 3.3, 3.4 respectively. The previously published theoretical predictions[121] and experimental measurements[13, 120, 126] are also shown for comparison. In order to reproduce the best predictions from the Ref.[32] we optimize the geometry at HF/6-31G theory level under planar constraint and compare the root mean square deviation (RMSD) values for the predicted 1PA excitation energies from the experimental ones. RMSD is a predictive measure of the differences between calculated (x_1) and experimentally observed (x_2) values given as

$$RMSD = \sqrt{\frac{\sum_{i=1}^{n} (x_{1,i} - x_{2,i})^2}{n}} \tag{3.1}$$

As one can infer from the RMSD values shown in Table 3.1, we observe a considerable improvement with the use of polarization function in the basis set (column D vs. A). For this reason, we use 6-31G* basis in the rest of this study. The planar geometrical constraint helps to improve the agreement with the experiment somewhat when B3LYP and M05 optimization levels are used (column F vs. E and column I vs. J). When the same theory level is used with different geometries, M05-2X presents an improvement over B3LYP (column G vs. F), but HF remains the best. We notice that the B3LYP/6-31G* geometries with larger basis set provide slight deterioration in the RMSD values when compared to B3LYP/6-31G level from Ref.[121] This could be attributed to the underestimated bond length alternation (BLA) parameters in B3LYP geometries, in the basis set limit, which was reported previously.[137, 138] Essentially, smaller basis set counteracts electron over delocalization inherent in DFT methods.

Table 3.1: Comparison of 1PA excitation energies (eV) for different basis sets, geometry optimization constraints and theory levels.

Excitations	⟹	B3LYP/6-31G			B3LYP/6-31G*				M05/6-31G*	
Geometry	⟹	Popt[e] HF	HF/ nonplanar[d]	Popt[e] B3LYP[d]	Popt[e] HF	Popt[e] B3LYP	B3LYP	Popt[e] M05-2X	Popt[e] M05	M05
Mol. #	Exp	A	B	C	D	E	F	G	H	I
1	4.18[a,b]	4.23	4.34	4.07	4.18	4.02	4.01	4.08	4.00	4.00
2	3.32[a,b]	3.61	3.67	3.46	3.59	3.44	3.46	3.50	3.50	3.50
3	3.04[a,b,c]	3.06	3.15	2.89	3.05	2.87	2.88	2.94	2.96	2.97
4	2.90[a,b]	2.92	3.04	2.76	2.91	2.73	2.77	2.80	2.80	2.87
5	2.72[a,b]	2.67	2.74	2.52	2.68	2.43	2.44	2.53	2.52	2.53
6	2.53[c]	2.65	2.67	2.49	2.67	2.51	2.51	2.58	2.62	2.63
7	2.42[a]	2.30	2.35	2.22	2.29	2.09	2.09	2.17	2.19	2.19
8	2.24[a]	2.06	2.14	2.00	2.13	1.96	1.96	2.03	2.09	2.10
9	2.01[a]	1.71	1.68	1.62	1.80	1.66	1.66	1.72	1.79	1.81
10	2.92[a,f]	2.90	2.90	2.75	2.90	2.73	2.75	2.80	2.84	2.90
11	2.83[c]	2.86	3.07	2.80	2.86	2.70	2.80	2.76	2.82	2.94
12	3.18[b]	3.32	3.32	3.14	3.32	3.13	3.14	3.21	3.19	3.20
13	3.01[b]	3.08	3.08	2.88	3.10	2.87	2.87	2.96	2.93	2.94
14	2.88[b]	2.89	2.89	2.66	2.91	2.65	2.66	2.76	2.72	2.73
15	2.76[b]	2.73	2.73	2.48	2.76	2.47	2.48	2.59	2.56	2.55
16	2.65[b]	2.55	2.55	2.36	2.56	2.34	2.23	2.42	2.47	2.33
RMSD		0.132	0.161	0.198	0.115	0.223	0.228	0.159	0.151	0.162

[a] Ref[13] , [b] Ref[120], [c] Ref[126], [d] Ref[121], [e] Partial optimization with planar constraint , [f] Measured for NPh_2 analog.

This energy corresponds to state with the highest oscillator strength. Same basis set are used for geometry optimization and energy predictions. The numbering of the molecules is specified in Figure 3.1.

Table 3.2: Comparison of excitation energies (eV) of 1PA for different XC functionals for the same optimized geometries with experiment and benchmarked results.

Excitations	⟹	HSE06	B3LYP	M05	BMK	M05-2X	CAM-B3LYP
Geometry	⟹	M05-2X/6-31G*					
Mol. #	Exp[a,b,c]	A	B	C	D	E	F
1	4.18	4.13	4.10	4.07	4.36	4.42	4.39
2	3.32	3.55	3.53	3.57	3.82	3.90	3.91
3	3.04	3.00	3.01	3.10	3.37	3.49	3.51
4	2.90	2.91	2.91	2.98	3.25	3.37	3.37
5	2.72	2.58	2.59	2.67	2.94	3.06	3.08
6	2.53	2.58	2.60	2.72	2.99	3.13	3.16
7	2.42	2.20	2.23	2.35	2.62	2.78	2.77
8	2.24	2.05	2.08	2.22	2.47	2.64	2.63
9	2.01	1.67	1.74	1.90	2.15	2.34	2.35
10	2.92[f]	2.90	2.93	3.03	3.29	3.42	3.45
11	2.83	2.87	2.89	3.01	3.26	3.39	3.41
12	3.18	3.25	3.24	3.28	3.53	3.62	3.63
13	3.01	2.96	2.96	3.02	3.25	3.36	3.37
14	2.88	2.78	2.78	2.84	3.08	3.19	3.21
15	2.76	2.61	2.58	2.68	2.92	3.04	3.06
16	2.65	2.41	2.45	2.56	2.84	2.99	3.00
RMSD		0.155	0.137	0.115	0.305	0.423	0.434

[a] Ref[13], [b] Ref[120], [c] Ref[126], [f] Measured for NPh_2 analog.

Same basis set is used for geometry optimization and energy predictions.

The accuracy of different XC functionals can be analyzed from the data presented in Table 3.2. As one can see from the RMSD values reported in this table, M05-2X/6-31G* geometry combined with the M05 functional for calculation of 1PA excitation energies give the similar agreement with the experimental measurements (column C in Table 3.2), as the best result obtained from the HF/6-31G* optimization level (column D in Table 3.1), without the artificial constraints. We attribute this to the superior description of the BLA parameter with M05-2X functional, reported recently.[7] We also observe here that an enhancement in the fraction of the HF exchange from 20% (B3LYP) to 28% (M05) improves the agreement with the experiment. However, further increase in orbital exchange component such as 42% (BMK) or 56% (M05-2X) as well as long-range-corrected functional such as CAM-B3LYP (20%-65%) quickly deteriorate the energy predictions. This is in contrast with the reports that 50% HF exchange improves the description of the charge-transfer component in conjugated chromophores.[139] The screened hybrid functional like HSE06 (25%-0%) deteriorates these predictions from B3LYP ones.

The trends observed for 2PA excitation energies presented in Table 3.3 are similar to those of 1PA. The conclusions about the larger basis set, geometrical constraints and optimization levels for 1PA excitation energies hold true for the 2PA energies too. However, the comparison of different XC functionals for the 2PA excitation energies reported in Table 3.4 demonstrates that B3LYP performs considerably better than M05 and other higher exchange functionals. This observation may be useful in the future development of the frequency-dependent functionals. Again the unconstrained M05-2X/6-31G* geometries are as good as planar constrained HF/6-31G* ones.

Table 3.3: Excitation energies (eV) of 2PA maxima.

Excitations	⇨	B3LYP/6-31G			B3LYP/6-31G*				M05/6-31G*	
Geometry	⇨	Popt[e] HF	HF/ nonplanar[d]	Popt[e] B3LYP[d]	Popt[e] HF*	Popt[e] B3LYP*	B3LYP*	Popt[e] M05-2X*	Popt[e] M05*	M05*
Mol. #	Exp[a,b,c]	A	B	C	D	E	F	G	H	I
1	2.41	2.68	2.69	2.60	2.65	2.58	2.57	2.61	2.67	2.67
2	2.05	2.19	2.19	2.13	2.19	2.13	2.14	2.16	2.23	2.24
3	1.70	1.77	1.79	1.69	1.77	1.70	1.70	1.73	1.82	1.82
4	1.70	1.73	1.77	1.65	1.74	1.66	1.68	1.69	1.77	1.80
5	1.60	1.56	1.58	1.47	1.57	1.45	1.46	1.50	1.58	1.58
6	1.50	1.52	1.52	1.46	1.54	1.47	1.48	1.50	1.58	1.58
7	1.32	1.33	1.65	1.52	1.32	1.23	1.22	1.27	1.35	1.35
8	1.28	1.19	1.21	1.15	1.23	1.16	1.16	1.19	1.30	1.30
9	1.27	1.01	1.21	1.25	1.01	0.96	0.95	0.98	1.07	1.06
10	1.55[f]	1.67	1.69	1.60	1.67	1.61	1.62	1.64	1.72	1.74
11	1.57	1.63	1.68	1.55	1.64	1.56	1.58	1.59	1.70	1.73
12	1.94	1.98	1.98	1.91	1.99	1.92	1.92	1.95	2.02	2.03
13	1.75	1.82	1.82	1.73	1.83	1.74	1.74	1.78	1.85	1.85
14	1.70	1.69	1.69	1.59	1.71	1.60	1.60	1.65	1.71	1.71
15	1.70	1.59	1.59	1.47	1.61	1.48	1.48	1.54	1.60	1.60
16	1.48	1.44	1.46	1.34	1.45	1.35	1.31	1.39	1.47	1.43
RMSD		0.123	0.132	0.114	0.110	0.128	0.131	0.113	0.123	0.131

[a] Ref[13], [b] Ref[120], [c] Ref[126], [d] Ref[121], [e] Partial optimization with planar constraint , [f] Measured for NPh2 analog.
Same basis set is used for geometry optimization and energy predictions.

Table 3.4: Comparison of 2PA excitation energies at different XC functionals.

Excitations	⇨	HSE06	B3LYP	M05	BMK				M05-2X	CAM-B3LYP
Geometry	⇨	M05-2X/6-31G*								
Mol. #	Exp[a,b,c]	A	B	C	D		E		F	
1	2.41	2.63	2.61	2.70	2.97	-	3.12	-	3.10	-
2	2.05	2.17	2.17	2.26	2.49	2.85	2.60	2.95	2.59	2.93
3	1.70	1.72	1.76	1.87	2.07	2.29	2.51	-	2.53	-
4	1.70	1.71	1.74	1.85	2.05	2.25	2.45	-	2.46	-
5	1.60	1.48	1.53	1.65	2.02	-	2.19	-	2.22	-
6	1.50	1.48	1.51	1.61	1.81	2.24	1.93	2.38	1.95	-
7	1.32	1.23	1.28	1.41	1.68	1.99	1.87	2.11	1.88	2.11
8	1.28	1.15	1.20	1.34	1.60	-	1.80	-	1.80	-
9	1.27	0.91	0.98	1.09	1.41	-	1.61	1.83	1.83	-
10	1.55[f]	1.64	1.68	1.78	1.97	2.27	2.05	2.47	2.08	2.49
11	1.57	1.58	1.63	1.76	2.07	-	2.28	-	2.32	-
12	1.94	1.95	1.96	2.06	2.29	2.60	2.41	2.70	2.41	2.69
13	1.75	1.76	1.78	1.88	2.09	2.42	2.21	2.51	2.22	2.51
14	1.70	1.63	1.66	1.77	1.99	2.20	2.11	2.30	2.12	2.38
15	1.70	1.51	1.55	1.66	1.88	2.09	2.01	2.21	2.22	-
16	1.48	1.35	1.42	1.63	1.89	-	2.11	-	2.16	-
RMSD		0.136	0.113	0.156	0.374	0.566	0.564	0.725	0.598	0.712

[a] Ref[13], [b] Ref[120], [c] Ref[126], [f] Measured for NPh_2 analog.

Same basis set is used for geometry optimization and energy predictions.

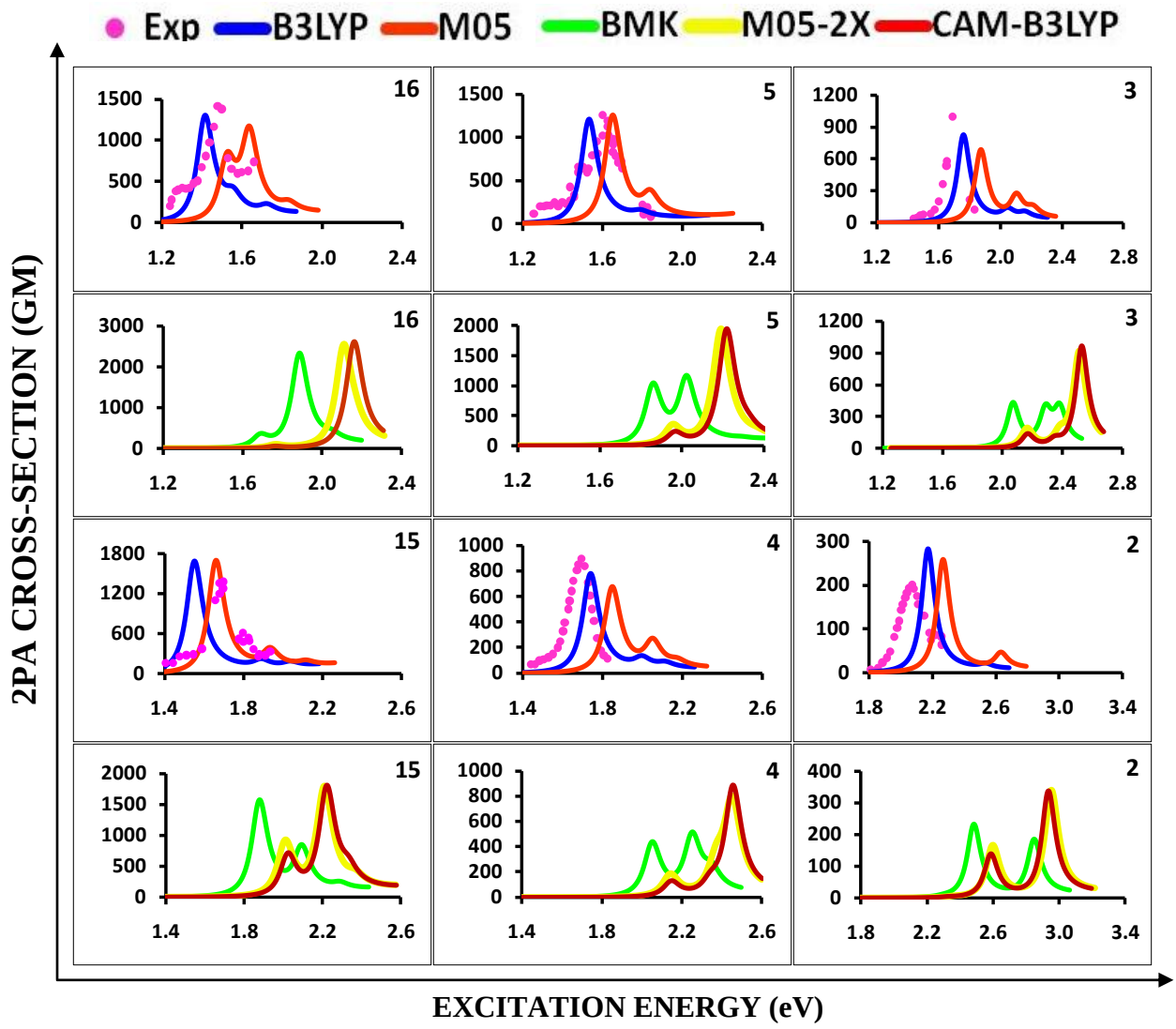

Figure 3.2: Comparison of calculated 2PA profiles using ATDA formalism at various exchange-correlation levels with the experimentally measured ones.

All calculations use ATDA-DFT/6-31G*//M05-2X/6-31G* theory level, six lowest states, and exchange-correlation functionals with different fraction of Hartree-Fock exchange (E_X^{HF}): B3LYP with 20%, M05 with 28%, BMK with 42%, M05-2X with 56%, and CAM-B3LYP with 20-65% . While B3LYP performs the best for 2, 4, 3 and 16, M05 is better for 5 and 15; the functionals with higher fraction of E_X^{HF}, as well as Coulomb-attenuated B3LYP predictions are too much blue-shifted; they predict multiple maxima in disagreement with experiment. In addition, increase in E_X^{HF} results in cross-section to be transferred to the higher lying states. The predictions obtained using the functional with correct asymptotic behavior LC-BLYP with 18-100% E_X^{HF} are so out of range, they could not be plotted on the same scale of energies and can't be considered meaningful. Molecule number is specified in the upper right corner of all the graphs.

BMK and M05-2X functionals with higher HF exchange not only overestimate the excitation energy values with significant blue shifts, but also predict multiple maxima on 2PA absorption profiles, in clear disagreement with experiment (Figure. 3.2), which made the energy comparison somewhat ambiguous. The performance of long-range-corrected XC functional CAM-B3LYP is also poor, and similar to M05-2X. Performance of HSE06 is again close to B3LYP, but not as good. Figure 3.2 presents a graphical comparison of calculated 2PA profiles with the experimentally measured ones for some of the molecules (2, 3, 4, 5, 15 and 16) under study. The calculated results are shown for B3LYP, M05, BMK, M05-2X and CAM-B3LYP levels with increasing fraction of HF exchange using ATDA formalism. We observe a gradual blue shift in the excitation energies with the increase in the HF exchange component. A low HF exchange functional B3LYP performs closest to the experiment for all the molecules considered except for 5 and 15. For these molecules, M05 functional exhibits the best match. Higher HF and long-range-corrected functionals predict multiple maxima for all the molecules.

3.3 Comparison of Different Nonlinear Formalisms

The 2PA cross-sections, calculated using different DFT formalisms are reported in Table 3.5 in units of Goeppert-Mayer (1GM=10^{-50} cm^4 s). For fair comparison, with the CEO predictions,[32] we use B3LYP/6-31G theory level and HF/6-31G geometries with planar constraints. Let us first discuss the results when only six lowest states are taken into account by the SOS procedure. Predictions obtained with the ATDA formalism differ from the exact CEO results by less than 7% on an average.

Table 3.5: Two-photon cross-sections (GM) using different TD-DFT formalisms.

Mol. #	Exp[a,b,c,g]	TD/CEO[d]	ATDA/SOS		QRSR/SOS	QRDR/SOS
		(NStates=6)	(NStates=6)	(NStates=30)	(NStates=3AG)	(NStates=3AG,3BU)
1	12	186	129	117	137	156
2	210	218	279	233	306	378
3	995	780	848	573	1030	1565
4	900	1145	828	610	1002	1394
5	1250	960	1125	1135	2047	2295
6	1750	650	468	447	658	708
7	620	1180	1339	1011	1674	2283
8	1750	1546	2277	1524	2879	3758
9	4400	2230	2262	1738	2803	3671
10[f]	450	845	682	588	886	1344
11	890	729	528	525	930	943
12	260	385	507	407	547	705
13	320	537	700	634	876	999
14	425	765	1028	916	1314	1519
15	1300	1180	1428	1253	1881	2198
16	1420	1736	1703	1024	2596	4478
RMSD		660	704	788	786	1197

[a] Ref[13], [b] Ref[120], [c] Ref[126], [d] Ref[121], [e] Partial optimization with planar constraint, [f] Measured for NPh_2 analog. [g] All experimental values tabulated are determined with nanosecond pulses.

Calculations done at TD-DFT/B3LYP/6-31G level using Popt[e] HF/6-31G geometries.

The calculated value for molecule 1 deviates by approximately 100GM from the experiment, which in this weak 2PA absorber amounts to an order of magnitude. For the rest of the molecules the experimental trends are well reproduced. One of the reasons for the trend not being reproduced by TD-DFT for 1 could be the unusually large configuration mixing in the 2PA state for this unsubstituted molecule, which was addressed by Zojer *et al.*[15] earlier. The reason for the large disagreement for 6 and 9 with experiment can be attributed to the prediction of three- and two-fold maxima for 2PA profiles in disagreement with the experiment. This might have resulted in nearly equal redistribution of the two-photon intensities over three or two calculated 2PA states, thus underestimating 2PA cross-section for the lowest 2PA state. In addition, for 9 a large uncertainty has also been reported in the experimental estimate of 2PA cross-section value arising from the uncertainty in the measurement of its reported fluorescence quantum yield.[13]

At the same time, QRDR calculations using exact to the second order transition dipoles (reported in the last column of Table 3.5) overestimate the cross-sections for each of the molecules by 20-150%. When the complete manifold of 1PA excited states is taken into account instead of just 3 states (QRSR column), this overestimation is largely corrected and the average agreement with experiment improves so that it becomes comparable with ATDA, yet not as good (Figure 3.3). Figure 3.3 compares the experimentally measured and the calculated 2PA profiles for molecules 2, 3, 4, 5, 15 and 16 using ATDA, QRSR and QRDR formalisms. All calculations were performed at B3LYP/6-31G//HF/6-31G theory level for consistency with CEO results. For molecule 16, ATDA performs almost identical to CEO. The experimentally observed two peaks are reproduced for this molecule with all the methods considered in this work. For the rest of the molecules only ATDA results are shown which is closest to the experiment.

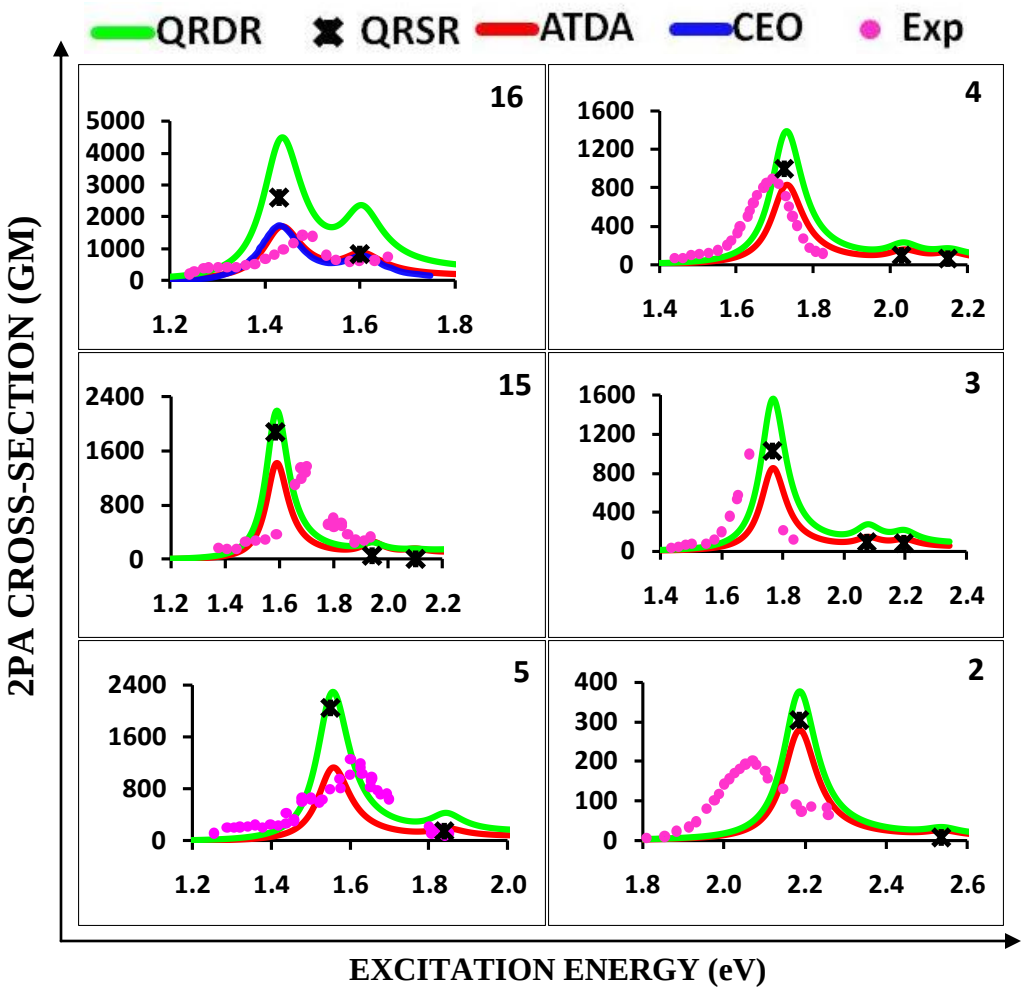

Figure 3.3: Comparison of experimentally measured and calculated 2PA profiles using different DFT formalisms.
All calculations are performed at B3LYP/6-31G//HF/6-31G theory level for molecules 2, 3, 4, 5, 15 and 16. While ATDA and CEO predictions nearly coincide and stay close to the experimental measurements in all cases, QRDR always overestimate 2PA cross-sections, sometimes by a factor of three (16).

QRDR highly overestimates the cross-sections in all cases, while QRSR results are always intermediate between ATDA and QRDR. When SOS approach is used explicitly, the summation can be truncated to inlcude only those states below ionization threshold. This is not possible, however in QR formalisms, where summation is done implicitly. Unreliable states above

ionization threshold are the likely reason for overestimated values obtained with QR-DFT methods. We can further rationalize these results as following.

While overall density response to the external field is somewhat accuretely predicted by the QR-DFT formalism, the partitioning of this response into individual contributions of the states is rather incorrect due to the absence of double resonances in this formalism. On the other hand, double resonances (also known as doubly excited states) are explicitly present both in CEO and ATDA formalisms; an approximation to CEO. As a result, the contribution to the overall response from these double resonances is distributed over available single resonances closest to it in energy. This feature of QR-DFT formalism was particularly apparent in case of butadiene.[33] The detailed analysis of the higher excited states of nA_g symmetry in polyenes shows an interesting trend. When compared to the coupled-cluster benchmarked values for the transition dipole moments from $1B_u$ to nA_g state, the QR-DFT predicted values typically demonstrate twice larger disagreement than the ATDA ones. However, for selected states near double resonances, the QR-DFT transition dipoles exceed the accurate coupled-cluster values by an order of magnitude or more.[33] This situation results in the qualitatively incorrect interpretation of the electronic structure obtained with QR-DFT. Given that selection of essential states is less than obvious in CEO formalism, the ATDA remains the only choice for the DFT study of the structure-property relationships and rational design of the improved NLO chromophores.

These trends are further analyzed in terms of the transition dipole moments obtained with ATDA and QRDR formalisms as reported in Table 3.6. It also includes the analysis of the excited states in terms of the leading Slater determinants. The nature of the electronic transitions are analyzed in terms of the Kohn-Sham (KS) orbitals as depicted in the last two columns of the table.

Table 3.6: Scalar values for transition dipole moments (a.u.) for essential states and their electronic structures in terms of the leading configurations using different TD-DFT formalisms at B3LYP/6-31G theory level.

Mol. #	B3LYP/6-31G//Popt[e]HF/6-31G					
	X	ATDA/SOS		QRDR/SOS	Leading configurations in 1PA and 2PA states	
		$\langle S_0\|\mu\|S_1\rangle$	$\langle S_1\|\mu\|S_X\rangle$	$\langle S_1\|\mu\|S_X\rangle$	S_1	S_X
1	4	3.10	3.20	3.53	80%(1-1')	3% (1-3') + 37% (1-4') + 60%(4-1')
2	4	3.98	4.08	4.77	82%(1-1')	10%(1-4') + 85%(2-1')
3	2	5.31	6.07	8.25	86%(1-1')	9%(1-2') + 86%(2-1')
4	2	5.30	5.56	7.20	84%(1-1')	10%(1-2') + 86%(2-1')
5	2	6.43	6.88	9.36	84%(1-1')	14% (1-2') + 82%(2-1')
6	3	4.52	6.10	7.73	85%(1-1') + 3%(1-2')	3%(1-3') + 87%(2-1') + 5%(2-2')
7	2	5.90	7.34	9.59	86%(1-1')	76%(1-2') + 21%(2-1')
8	4	6.80	8.02	11.14	86%(1-1')	80%(1-2') + 15%(4-1')
9	2	6.46	9.57	12.32	87%(1-1')	88%(1-2') + 3%(2-1')
10	2	5.30	6.16	8.03	86%(1-1')	6%(1-2') + 88%(2-1')
11	2	5.16	6.57	9.00	86%(1-1')	23%(1-2') + 75%(2-1')
12	2	4.82	4.83	5.71	81%(1-1')	3%(1-2') + 11%(1-4') + 82%(2-1')
13	2	5.52	5.52	6.62	80%(1-1')	10% (1-2') + 4%(1-4') + 82%(2-1')
14	2	6.15	6.20	7.58	80%(1-1')	16%(1-2') + 81%(2-1')
15	2	6.72	6.86	8.57	80%(1-1')	17%(1-2') + 80%(2-1')
16	2	6.74	7.80	12.63	89%(1-1')	3%(1-2') + 91%(2-1')

[e] Partial optimization with planar constraint.

Here S_0 denotes the ground state, S_1 is 1PA excited state, and S_X is 2PA excited state. HOMO, HOMO-1, etc. are abbreviated as 1, 2, … and LUMO, LUMO+1, etc. are abbreviated as 1', 2', … respectively; thus, HOMO-LUMO excited Kohn-Sham determinant is denoted as (1-1').

We observe that the dramatic overestimation of 2PA cross-section values obtained with the QRDR formalism is due to the overestimation of the calculated excited-to-excited state transition dipoles for this method as illustrated in Table 3.S1. The 1PA state in all the molecules is the lowest excitation of highest occupied molecular orbital (HOMO) to lowest unoccupied molecular orbital (LUMO) type, as it often happens in polyenes.

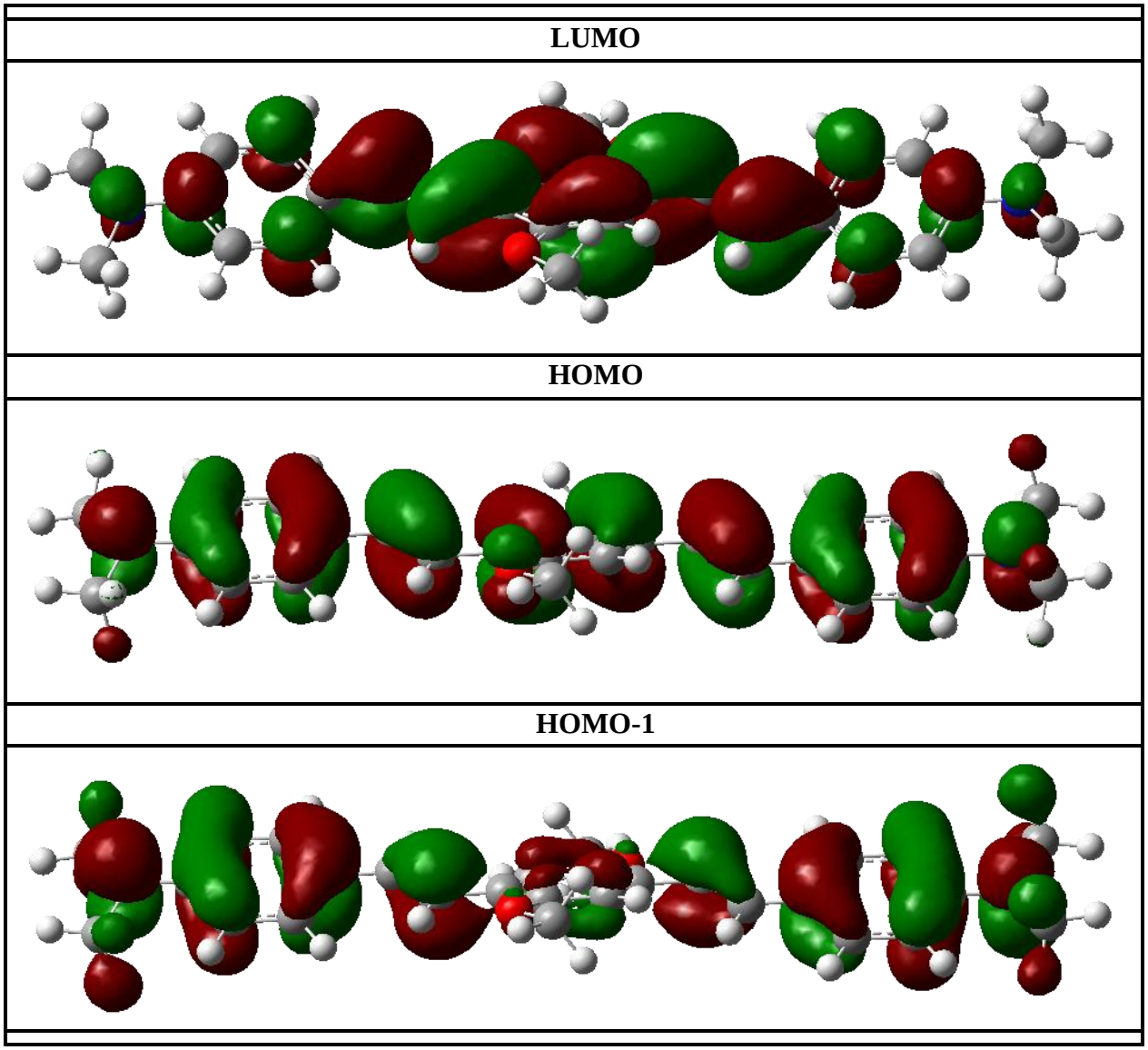

Figure 3.4: Plot of isosurfaces of 0.02a.u. value for HOMO-1, HOMO, and LUMO for molecule 4.

The 2PA state was found to be HOMO to LUMO+1 type for 7, 8 and 9, and HOMO-1 to LUMO type for the rest of the molecules.

We can rationalize this as following. The molecules 7, 8 and 9 belong to the acceptor-donor-acceptor type, which means they carry two terminal substituents with a low-lying vacant orbital. As a result, symmetric and antisymmetric combinations of these fragment orbitals, somewhat delocalized over the rest of the molecule make up the LUMO and LUMO+1 orbitals of the entire chromophore. While the transition from the ground to 1PA state consists of electron promotion from HOMO to LUMO, the transition from 1PA to 2PA state is then accompanied by the promotion of the electron from the LUMO (singly occupied in 1PA state) to LUMO+1. The latter transition has a large transition dipole, since the KS orbitals involved are composed of the same fragment orbitals. Similarly, remaining molecules are of donor-π-donor and donor-acceptor-donor types. Their terminal substitutes bring high-lying occupied fragment orbitals to form HOMO and HOMO-1 upon their symmetric and antisymmetric combinations. Hence 1PA to 2PA transition dipoles are also large here. We plot the HOMO-1, HOMO, and LUMO for the molecule 4 in Figure 3.4 as an illustration. Molecule 1 is an unsubstituted stilbene; it has neither donor, nor acceptor substituents and demonstrates the lowest 2PA cross-section of the set.

3.4 Effect of Higher Lying States on Cross-Sections

Increasing the number of states from 6 to 30 for ATDA formalism uniformly reduce the absolute cross-section values from 5-66% which improves the agreement with experiment for most of the molecules (Table 3.5). The reduction is due to the negative contribution of the higher excited states to the nonlinear response values. Further increase in the number of excited states was not attempted for the following reason. According to Epifanovsky *et al.*,[140] wavefunction

based correlated methods introduce significant errors in description of the valence states located above the ionization threshold. Such high-lying states are surrounded by the ionized states describing free electron scattered in the field of molecular cation. In the hypothetical case of the complete basis set, these ionized states would form a continuum. In practice, only limited number of discrete ionized states appear in the calculation and their energies are severely distorted by the absence of the plane waves in the standard gaussian basis set. These ionized states mix in with the bright valence states, resulting in several states with appreciable dipole moments. These states can no longer be predicted reliably, their energies strongly depend on the basis set used and approach the ionization potential as the basis is increased. In the TD-DFT method these difficulties are compounded by the incorrect asymptotics of the common XC potentials. Transitions to the continuum predicted with TD-DFT were shown to be strongly functional-dependent.[141] In the molecules considered here the vertical ionization energy (calculated as energy difference between the neutral and the radical-cation) falls in the range of about 5.1-7.2 eV, depending on the system. The individual number of states lying below the ionization threshold for all the molecules are reported in Table 3.S2. Table 3.S2 shows the exact number of reliable states do not exceed 30 for most of the molecules under study. At the same time, the cross-section values predicted for 30 singlet excited states for all the molecules are observed to be similar to the ones computed using their corresponding exact states below ionization. Therefore, it makes sense to limit the number of states uniformly to 30 for the entire set of molecules to obtain the best predictions for the cross-section values. We argue that most of the continuum states, represented in the Gaussian basis results, which are unphysically mixed with the true valence states (including the bright ones) are eliminated by this procedure.

Table 3.7: Essential state analysis using SOS formalism for the calculation of 2PA cross-sections at B3LYP/6-31G//Popt[e]HF/6-31G level.

Mol. #	# of states included in SOS	State # i	Detuning $\left(\omega_{0i} - \frac{\omega_{02}}{2}\right)$ (eV)	1PA oscillator strength	2PA cross-section $\sigma^{(2)}\left(\frac{\omega_{02}}{2}\right)$ x_i (GM)	% Dev. $\left(\frac{x_i - x_2}{x_i}\right)\times 100$
4	**-**	**S_1**	**1.20**	**2.011**	**-**	**-**
(x_2 = 900GM)[a,b]	**2**	**S_2**	**1.73**	**0.000**	**778**	**-16**
	3	**S_3**	**2.04**	**0.036**	**824**	**-9**
	5	**S_5**	**2.49**	**0.039**	**827**	**-9**
	6	**S_6**	**2.58**	**0.000**	**828**	**-9**
	7	**S_7**	**2.72**	**0.303**	**696**	**-29**
	8	**S_8**	**2.88**	**0.123**	**620**	**-45**
	30	**S_{30}**	**4.48**	**0.000**	**610**	**-47**
12	**-**	**S_1**	**1.35**	**1.889**	**-**	**-**
(x_2 = 260 GM)[b]	**2**	**S_2**	**1.98**	**0.000**	**510**	**49**
	4	**S_4**	**2.24**	**0.089**	**513**	**49**
	6	**S_6**	**2.97**	**0.012**	**507**	**49**
	8	**S_8**	**3.04**	**0.178**	**439**	**41**
	24	**S_{24}**	**4.85**	**0.444**	**408**	**36**
	30	**S_{30}**	**5.01**	**0.000**	**407**	**36**

[a] Ref[13], [b] Ref[120], [e] Partial optimization with planar constraint.

The effective elimination of continuum states thus is serving as the compensation for deficiencies in continuum description by the Gaussian basis sets and existing approximate DFT functionals The SOS expression (Equation 2.41) depicts that the contribution of each intermediate state to the 2PA cross-section is inversely proportional to the detuning factor $\left(\omega_{01} - \frac{\omega_{02}}{2}\right)$ and proportional to the product of the transition dipoles to and from this intermediate state.

In Table 3.7, we perform the essential-state-analyses for molecules 4 and 12 for illustrating the importance of these factors in the accurate prediction of cross-section values. In the substituted PPV dyes considered in this work there is only one bright 1PA state (the lowest one) with the large transition dipole and oscillator strength (essentially, the square of transition dipole from the ground state). Detuning, on the other hand, is larger than 1 eV for all the states, and cannot serve as the major criterion for the intermediate state selection. As a result, no matter how many states are close in energy to the half-2PA excitation, only bright 1PA states with appreciable transition dipoles from the ground state contribute significantly to the 2PA cross-section values. Whereas, the higher lying 1PA states (with relatively weaker oscillator strengths) result in the much larger detuning. We clearly observe the cross-section values being sensitive to the inclusion of the bright 1PA states (states with significant oscillator strengths) for these molecules. Some of these states have transition dipoles to 2PA state of the opposite sign compared to S_1 to 2PA transition dipole. Therefore, the cross-sections somewhat decrease with the inclusion of the higher excited states into SOS. This underestimation deteriorates the agreement with experiment for molecule 4 wherein improves for 12.

Table 3.8: Two-photon cross-sections (GM) using different theory levels for geometry and excitations.

Excitations	⇨	B3LYP/6-31G*				M05/6-31G*	
Geometry	⇨	Popt[e]HF	Popt[e]B3LYP	B3LYP	Popt[e]M05-2X	Popt[e]M05	M05
Mol. #	Exp[a,b,c,g]	ATDA/SOS (NStates=6)					
1	12	127	143	143	134	143	142
2	210	274	314	308	293	288	286
3	995	830	1005	992	921	860	850
4	900	824	1012	963	923	918	837
5	1250	1096	1596	1582	1367	1626	1587
6	1750	488	631	628	554	601	598
7	620	1331	1563	1564	1367	1602	1598
8	1750	2149	2919	2880	2587	2657	2616
9	4400	2073	3202	2749	2685	2171	1642
10	450	687	860	844	788	754	694
11	890	529	619	455	586	650	458
12	260	496	535	530	541	531	526
13	320	682	895	894	800	886	880
14	425	994	1371	1360	1203	1366	1359
15	1300	1365	1979	1964	1705	2004	1983
16	1420	1668	2323	2158	1988	1586	1884
RMSD		729	704	746	674	799	901

[a] Ref[13], [b] Ref[120], [c] Ref[126], [d] Ref[121], [e] Partial optimization with planar constraint, [g] All experimental values tabulated are determined with nanosecond pulses.

Same basis set used for geometry optimization and energy predictions.

Table 3.9: Comparison of 2PA cross-sections (GM) using different XC functionals.

Excitations	⇨	HSE06	B3LYP	M05	BMK		M05-2X		CAM-B3LYP	
Geometry	⇨	M05-2X/6-31G*								
Mol. #	Exp[a,b,c,g]	ATDA/SOS (NStates=6)								
1	12	131	130	127	137	-	98	-	76	-
2	210	287	283	258	233	186	166	339	139	336
3	995	623	827	684	437	424	920	-	968	-
4	900	796	782	680	441	518	802	-	887	-
5	1250	1189	1216	1258	1165		1951	-	1947	-
6	1750	529	505	495	552	747	405	367	337	-
7	620	1097	1280	1280	1214	683	1085	1018	873	1182
8	1750	2248	2115	1502	1576	-	1224	-	865	-
9	4400	2122	2229	1720	1318	-	1864	1653	1955	-
10	450	585	640	607	432	452	242	698	182	766
11	890	372	388	391	413	-	599	-	633	-
12	260	513	523	470	424	313	307	549	259	556
13	320	784	799	788	721	454	436	839	329	884
14	425	1150	1184	1183	1097	510	669	943	528	1041
15	1300	1605	1687	1701	1580	854	926	1795	1812	-
16	1420	1311	1301	1174	2337	-	2555	-	2611	-
RMSD		730	717	818	924	878	825	884	835	873

[a] Ref[13], [b] Ref[120], [c] Ref[126], [d] Ref[121], [g] All experimental values tabulated are determined with nanosecond pulses.

Sub-columns are used for the functionals that predict multiple 2PA maxima. Same basis set used for geometry optimization and energy predictions.

3.5 Effect of Basis Sets and Geometrical Constraints on Cross-Sections

The effects of the variations in other computational details are presented in Table 3.8. The change of the geomerty optimization method from HF to B3LYP leads to almost uniform increase in the cross-sections. The M05-2X geometry also leads to the increase (though not as pronounced) and improves the RMSD to give the best agreement. In contrast to the trends observed for transition energies, the cross-sections calculted with M05 optimized geometries are not improving the agreement. Nevertheless, the planar constraint helps to improve the agreeement with the experiment for 2PA cross-sections as observed for excitation energies as well.

3.6 Effect of Higher Orbital Exchange on Cross-Sections

The effect of various XC functionals on 2PA cross-sections is tabulated in Table 3.9. For consistency, the same optimization level (M05-2X/6-31G*) is used for all the computations. As one can see from the table, the excited state calculations using the higher exchange (BMK and M05-2X) and long-range (CAM-B3LYP) hybrid functionals not only overstimate the cross-sections but predict multiple maxima, in disagreement with the experiment. Surprisingly, the B3LYP functional provides the best agreement. The use of the screened hybrid functional like HSE06 comes as the close second. The predictions obtained using the functional with the correct asymptotic behavior (long-range-corrected BLYP), LC-BLYP (18% -100%) is so out of range that they could not be plotted on the same scale of energies and cannot be considered meaningful.

Table 3.10 reports the transition dipole moments at B3LYP/6-31G* and CAM-B3LYP/6-31G* levels for M05-2X/6-31G* optimized geometries using ATDA method.

Table 3.10: Scalar values for transition dipole moments (a.u.) using ATDA formalism at B3LYP/6-31G* and CAM-B3LYP/6-31G* levels for M05-2X/6-31G* optimized geometry.

Mol. #	B3LYP/6-31G*//M05-2X/6-31G*			CAM-B3LYP/6-31G*//M05-2X/6-31G*				
	ATDA/SOS							
	L	$\langle S_0\|\mu\|S_1\rangle$	$\langle S_1\|\mu\|S_L\rangle$	M	N	$\langle S_0\|\mu\|S_1\rangle$	$\langle S_1\|\mu\|S_M\rangle$	$\langle S_1\|\mu\|S_N\rangle$
1	4	3.09	3.15	6	-	3.02	1.88	-
2	4	4.00	3.93	4	5	3.93	2.28	2.35
3	2	5.32	5.83	6	-	5.27	3.44	-
4	2	5.18	5.29	6	-	5.02	3.26	-
5	2	6.56	6.62	4	-	6.36	4.02	-
6	3	4.62	5.85	3	-	5.25	3.38	-
7	2	5.94	7.34	4	6	6.13	3.38	2.60
8	2	6.73	4.94	6	-	6.83	2.90	-
9	2	6.66	9.30	6	-	6.89	2.55	-
10	2	5.18	5.98	2	6	5.24	2.55	3.06
11	2	4.94	6.47	3	-	5.22	3.48	-
12	2	4.90	4.66	4	5	4.78	2.57	2.56
13	2	5.71	5.33	2	5	5.57	2.38	2.72
14	2	6.39	5.94	2	5	6.21	2.78	2.45
15	2	7.05	6.55	3	-	6.84	3.47	-
16	2	7.06	7.42	6	-	6.98	4.12	-

Here S_0 is the ground state, S_1 is 1PA excited state and S_L, S_M, S_N are 2PA excited states.

Table 3.11: Comparison of ground-to-excited (μ_{01}) and excited-to-excited (μ_{1Y}, μ_{1X}) state transition dipole moments (a.u.), detuning (D) factors (eV), and 2PA cross-sections (σ) (GM) of ATDA/CAM-B3LYP/6-31G* and ATDA/B3LYP/6-31G* methods for M05-2X/6-31G* geometries.

Mol. #	ATDA/SOS (NStates=6)			
	$\sigma_{CAM\text{-}B3LYP}/\sigma_{B3LYP}$	$\lvert\mu_{01}\rvert^2_{CAM\text{-}B3LYP}/\lvert\mu_{01}\rvert^2_{B3LYP}$	$\lvert\mu_{1Y}\rvert^2_{CAM\text{-}B3LYP}/\lvert\mu_{1X}\rvert^2_{B3LYP}$	$D^2_{B3LYP}/D^2_{CAM\text{-}B3LYP}$
1	**0.58**	**0.96**	**0.36**	**1.33**
2	**0.49**	**0.97**	**0.34**	**1.06**
3	**1.17**	**0.98**	**0.35**	**1.63**
4	**1.13**	**0.94**	**0.38**	**1.65**
5	**1.60**	**0.94**	**0.37**	**1.52**
6	**0.67**	**1.29**	**0.33**	**0.81**
7	**0.68**	**1.06**	**0.21**	**1.14**
8	**0.41**	**1.03**	**0.34**	**1.12**
9	**0.88**	**1.07**	**0.08**	**2.14**
10	**0.28**	**1.02**	**0.18**	**0.83**
11	**1.63**	**1.12**	**0.29**	**1.34**
12	**0.50**	**0.95**	**0.30**	**1.10**
13	**0.41**	**0.95**	**0.20**	**1.05**
14	**0.45**	**0.94**	**0.22**	**1.06**
15	**1.07**	**0.94**	**0.28**	**1.50**
16	**2.01**	**0.98**	**0.31**	**1.50**

Here, X=1PA and Y=2PA states and the detuning D is defined as $\left(\omega_{1PA} - \frac{\omega_{2PA}}{2}\right)$.

We observe that the ground-to-excited state transition dipole moments reported at M05-2X level are in good agreement with the B3LYP ones. Whereas, the excited-to-excited state transition dipole values are highly underestimated for the CAM-B3LYP functional. Table 3.11 further investigates the factors responsible for the incorrect prediction of the 2PA cross-sections using the CAM-B3LYP functional in comparison to B3LYP predictions. Here, we report the ratios of ground- and excited- state transition dipoles, detuning between the 1PA and 2PA states and 2PA cross-section values of the ATDA/CAM-B3LYP/6-31G* method with the ATDA/B3LYP/6-31G* one for M05-2X/6-31G* geometries. The 2PA cross-sections calculated using CAM-B3LYP functional do not follow a specific trend for deviations from B3LYP. We observe that the excited-to-excited state transition dipoles moments are underestimated for CAM-B3LYP in comparison to B3LYP for all the molecules. However, this leads to the underestimation in their corresponding cross-section values only if the excitation energies are not much overestimated. The overestimation of the cross-section values at CAM-B3LYP level for few molecules is attributed to huge underestimation in their detuning values in comparison to B3LYP. The reason for this may be the stronger dependence of the detuning factor (denominator in Equation. 2.39) on the ratio of 1PA and 2PA excitation energies, which are not predicted correctly by this functional.

3.7 Conclusions

We tested different second and third order formalisms within TD-DFT theory for their accuracy in prediction of the 2PA spectra for the chromophores of substituted PPV types. The ATDA method[33] was found to give the best agreement with benchmarked[121] and experimental[13, 120, 126] data. Its results presented almost no change from the full CEO ones, while providing

greater computational efficiency and the ease of interpretation. We recommend ATDA for both quantitative predictions and qualitative analysis of 2PA properties. On the other hand, QRSR and especially QRDR formalisms implemented in DALTON are not recommended for qualitative analysis of the state-specific contributions, although overall quality of 2PA cross-sections for QRSR are close to ATDA ones.

We also studied the influence of different geometry, optimization levels and XC functionals on excitation energies and cross-sections. We conclude that adjusting the fraction of the exact exchange in the functionals does not improve the agreement with the experiment within the habitual approximations (the vertical excitations and empirical linewidths). A higher fraction of HF exchange (BMK and M05-2X functionals) leads to the blue shift and splitting of the 2PA bands (overestimated excitation energies and prediction of the multiple maxima) not observed in experiments. The asymptotically corrected functional LC-BLYP did not produce reasonable results; while range-separated CAM-B3LYP was similar to the M05-2X. We found that B3LYP is still the best for the spectral predictions, while M05-2X optimized geometry gives the best agreement with the experiment among the methods considered. The influence of the incorrect asymptotes is analyzed for the B3LYP functional. It leads to the collapse of the higher excited states to the ionization limit, but can be effectively mitigated by the use of the moderate basis sets and the neglect of the unreliable excited states above ionization threshold in the SOS series. The erroneous contribution of these unreliable states is not possible to prevent in QRSR, however.

Table 3.S1: Scalar values for transition dipole moments (a.u.) for essential states using different TD-DFT formalisms at B3LYP/6-31G theory level.

Mol. #	B3LYP/6-31G//Popt^{e}HF/6-31G					
	X	ATDA/SOS		QRDR/SOS	$\|\mu_{1X}\|^2_{QRDR}$ / $\|\mu_{1X}\|^2_{ATDA}$	σ_{QRDR} / σ_{ATDA}
		$\langle S_0\|\mu\|S_1\rangle$	$\langle S_1\|\mu\|S_X\rangle$	$\langle S_1\|\mu\|S_X\rangle$		
1	4	3.10	3.20	3.53	1.22	1.21
2	4	3.98	4.08	4.77	1.37	1.36
3	2	5.31	6.07	8.25	1.84	1.85
4	2	5.30	5.56	7.20	1.68	1.68
5	2	6.43	6.88	9.36	1.85	2.04
6	3	4.52	6.10	7.73	1.61	1.51
7	2	5.90	7.34	9.59	1.71	1.70
8	4	6.80	8.02	11.14	1.93	1.65
9	2	6.46	9.57	12.32	1.66	1.62
10	2	5.30	6.16	8.03	1.70	1.97
11	2	5.16	6.57	9.00	1.88	1.79
12	2	4.82	4.83	5.71	1.40	1.39
13	2	5.52	5.52	6.62	1.44	1.43
14	2	6.15	6.20	7.58	1.49	1.48
15	2	6.72	6.86	8.57	1.56	1.54
16	2	6.74	7.80	12.63	2.62	2.63

Here S_0 denotes the ground state, S_1 is 1PA excited state, and S_X is 2PA excited state. μ_{1X} is the transition dipole between 1PA to 2PA excited state and σ is 2PA cross-section.

Table 3.S2: Two-photon cross-sections using CEO and ATDA formalisms.

Mol. #	Exp	TD/CEO all terms	ATDA/SOS			
		(NStates=6)	(NStates=6)	(NStates=30)	# States below IP (X)	(NStates=X)
1	12	186	129	117	16	135
2	210	218	279	233	7	279
3	995	780	848	573	17	576
4	900	1145	828	610	15	604
5	1250	960	1125	1135	18	1140
6	1750	650	468	447	27	444
7	620	1180	1339	1011	79	1014
8	1750	1546	2277	1524	>102	-
9	4400	2230	2262	1738	>32	-
10	450	845	682	588	27	588
11	890	729	528	525	30	525
12	260	385	507	407	10	441
13	320	537	700	634	11	632
14	425	765	1028	916	13	919
15	1300	1180	1428	1253	14	1260
16	1420	1736	1703	1024	42	1021
RMSD		660	704	788		790

Including exact number of reliable excited states (those below Ionization limit) in SOS does not change the results obtained with 30 states included.

CHAPTER 4 PREDICTION OF TWO-PHOTON ABSORPTION SPECTRA WITH SEMIEMPIRICAL METHODS

The performance of various density functional theory (DFT) methods for the prediction of one- and two-photon absorption (1PA, 2PA) properties for a specific class of substituted PPV [poly (p-phenylene vinylene)] oligomers with donor-π-donor, donor-acceptor-donor and acceptor-donor-acceptor motifs has been studied in Chapter 3 However, an alternative to previously studied DFT methods is the use of semiempirical Hamiltonians within the wavefunctional theory (WFT) making them highly computationally inexpensive. In this chapter, different correlated semiempirical WFT methods are applied to the same set of molecules (Figure 3.1) and compared them to the experiment[13, 120, 126] and the previously reported results of the DFT methods. Here we use two types of semiempirical parameterizations: (a) the general purpose PM6 and (b) the spectroscopic ZINDO/S. The ZINDO/S[105] spectroscopic parameterization of Hamiltonian combined with single configuration interaction (CIS) method performs much better than the general purpose PM6 Hamiltonian[142] combined with different CI methods, but its accuracy is still trailing behind the DFT methods. The poor performance in the prediction of 2PA cross-sections at PM6 level is attributed to the incorrect description of the transition dipoles between 1PA and 2PA states. The 2PA cross-sections predicted by the ZINDO/S method are comparable to the best DFT predictions only when the overestimation in the 2PA energies is somehow corrected. So, we observe the semiempirical parameterizations can at best be used for quantitative analysis of the 2PA properties for this class of organic molecules. The ZINDO/S method combined with multi-reference configurations not only improves the prediction of the energetics but provide a good description of the intensities of 1PA and 2PA

excitations. However, the results are shown to be highly sensitive on the choice of the reference configurations, order of excitation and active space considered.

4.1 Computational Details

We use the general purpose semiempirical Hamiltonian PM6[142] with various CI methods as coded in MOPAC 2008 (molecular orbital package) computer program[143] for calculating the one- and two- photon excitations. The geometries are optimized either at DFT (HF/6-31G with planar constraint or M05-2X/6-31G*) or semiempirical (PM6) level. The DFT optimizations are performed using Guassian09[144] suite of programs whereas the semiempirical ones are using MOPAC 2008. The excitation energies calculated at PM6 level are compared to the TD-B3LYP/6-31G level for planar HF/6-31G geometries and TD-B3LYP/6-31G* for M05-2X/6-31G* geometries. We extracted ground-to-excited and excited-to-excited transition dipole moments from the semiempirical PM6 runs, and explicitly fed them into in-house script that implements sum-over-state (SOS) formalism (Equation 2.41) to calculate the 2PA cross-sections. They are compared to *a posteriori* Tamm-Dancoff approximation (ATDA) method within DFT implementations using six singlet excited states by SOS formalism.

The CI methods considered in this work were introduced in Chapter 2. Of those, the CIS and CISD methods are standard in the MOPAC 2008, whereas the customized list of configurations were used for the CISd and MRCIS ones. They differ in their order of excitations and the size of active space. The ground and excited state wavefunctions consist of Slater determinants with different order of excitations taking place within the active space comprising of the fixed number of MOs around the Fermi level. For CIS and MRCIS methods, we choose to restrict the active space to ten highest occupied and ten lowest unoccupied MOs (HOMO and

LUMO). The active space for single and double excitations for CISD method is varied from three to five HOMO and LUMO levels each. For CISd calculations, the active space is confined to ten HOMO and ten LUMO levels for single excitations, while only five HOMO and five LUMO levels are used for double excitations. The excitations for the MRCIS method are calculated from seven singly and doubly excited reference determinants added to the HF ground state determinant. The reference configurations are listed in Figure 4.S1. In the following subsections, the active space chosen for different CI methods is shown in the parenthesis following the method as "(m,n)" where the single excitations are restricted to "m" MOs around the Fermi level and double excitations to "n" MOs, if any.

The ZINDO/S method[105] parameterized for spectroscopic measurements supplemented by the CIS scheme is used for two-photon predictions using Gaussian09 software[144]. The geometries are optimized at HF/6-31G level under planar constraint for the direct comparison of the published results of TD-DFT methods with the ZINDO/S method. The results obtained with quadratic response single and double (QRSR and QRDR) methods are also shown along with the ATDA. The semiempirical parameterization for this method involves various fitting procedures for CI active space, number of singlet excited states and Slater-Condon (SC) factors for ($g_{1,\sigma}$) p-type σ or ($g_{1,\pi}$) p-type π orbitals. One of these are varied at a time, keeping rest fixed for obtaining the best fit for individual molecules. The CI active space is chosen for every molecule so that the further increase in size of active space does not affect the magnitude of predicted 1PA excitation energies. We observe that the 1PA energy values do not vary for the number of excited states from ten through forty for the computed CI active space for all the molecules individually. As a result, we choose to calculate the 2PA properties for forty singlet excited states. Finally, the empirical SC factor for ($g_{1,\pi}$) p-type π orbitals is varied from its default value

of 0.585 to close fit the experimental 1PA energies for computed active space individually for all the considered molecules. For ($g_{1,\sigma}$) p-type σ orbitals, the default SC value of 1.267 is taken unchanged.

4.2 General Purpose Parameterization (PM6)

4.2.1 One-Photon Excitation Energies using Different Orders of Excitation and Active Spaces in Configuration Interaction (CI) Methods

Here, we investigate the influence of the choice of the geometry optimization level, different orders of excitation and size of active space on 1PA and 2PA predictions using various CI methods at PM6 level. For comparison of different semiempirical WFT methods and the earlier reported TD-DFT results (Chapter 3), we compare the root mean square deviation (RMSD) of the 1PA and 2PA predictions from the experimental[13, 120, 126] data (Equation 3.1). Table 4.1 illustrates the dependence of 1PA energetics on the size of the CI active space and the method of geometry optimization. In Chapter 3, the 2PA cross-sections obtained using different DFT methods at TD/B3LYP/6-31G level for HF/6-31G geometries under planar constraint were presented. So, we choose to perform the semiempirical PM6 calculations at the same optimization level for comparing the ability of the two methods to predict the excited electronic states. At the same time, the effect of the choice of the optimization level on the PM6 predictions is studied by obtaining the 1PA energies for geometries optimized using PM6 Hamiltonian. The 1PA excitation energies using various CISD/PM6 methods for planar HF/6-31G and PM6 geometries are also reported in this table. Predictions obtained with the CISD method for different sizes of active space are extremely poor in comparison to the TD-DFT ones for the same geometry exhibiting a large deviation from the experiment. But the RMSD values for the

1PA energies suggest an overall improvement of around 0.2eV with an increase in the size of the active space from six to ten for both single and double excitations. Interestingly, the geometries optimized at PM6 level improves the agreement (< 0.1eV) with the experiment in comparison the HF ones. Still, the 1PA energies reported in this table are overestimated for the entire set of molecules in comparison to the experimental and TD-DFT values.

Table 4.2 represents the influence of different order of excitations in CI methods at PM6 level on 1PA energies for PM6 geometries. The PM6 geometries are chosen for their improved performance over planar HF ones (Table 4.1). The 1PA energies predicted at CIS(20) level offers a considerable improvement of about 0.2eV from the CISD(10,10) level. This indicates that the larger active space plays more prominent role in improving the agreement with the experiment than the inclusion of the double excitations within a smaller active space. For CISd(20,10) and MRCIS(20) methods, the energies relative to the HF ground state are also reported in addition to the ones with reference to their corresponding CI states. We observe a considerable improvement in the energies (of about 0.15-0.2eV) w.r.t to the ground state of the CI level than that of HF. Therefore, one can see that our ground state is not being "over correlated" at semiempirical CI levels. The energies relative to the HF state are substantially underestimated for the entire set of molecules. For the same size of the active space, inclusion of double excitations CISd(20,10) further improves the agreement with the experiment by about 0.1eV. Employing more than one reference determinant state in the ground state wavefunction for the calculation of excited states restricted by single substitutions MRCIS(20) perform close to that of the single and double excitations for one reference state CISd(20,10). The CISd(20,10) method shows the best agreement with the experiment for geometries optimized at PM6 level, while MRCIS(20) being the second best.

Table 4.1: Comparison of 1PA excitation energies (eV) for CISD method at PM6 level for geometries optimized at DFT and semiempirical levels. The effect of varying the size of the active space for a CI calculation is studied.

Excitations	⟹	CISD(10,10)/PM6	CIS(20)/PM6	CISd(20,10)/PM6		MRCIS(20)/PM6	
Geometry	⟹	PM6					
Mol. #	Exp[a,b,c]	$E(E_0^{CISD})$	$E(E_0^{CIS})$	$E(E_0^{HF})$	$E(E_0^{CISd})$	$E(E_0^{HF})$	$E(E_0^{MRCIS})$
1	4.18	4.27	3.11	2.93	4.22	3.01	3.41
2	3.32	3.45	2.74	2.50	3.25	2.50	2.91
3	3.04	3.49	2.66	2.59	3.03	2.57	2.79
4	2.90	3.06	2.56	2.45	2.78	2.42	2.63
5	2.72	2.96	2.54	2.45	2.69	2.44	2.58
6	2.53	3.24	2.60	2.49	2.92	2.49	2.92
7	2.42	2.87	2.44	2.36	2.63	2.34	2.51
8	2.24	2.86	2.58	2.53	2.65	2.51	2.61
9	2.01	3.05	2.60	2.57	2.63	2.59	2.61
10	2.92[d]	3.75	2.99	2.96	3.15	3.00	3.08
11	2.83	3.53	3.03	2.93	3.25	2.94	3.08
12	3.18	3.46	2.71	2.47	3.34	2.52	2.84
13	3.01	3.46	2.67	2.50	3.30	2.49	2.78
14	2.88	3.20	2.67	2.49	3.04	2.51	2.73
15	2.76	3.21	2.63	2.50	2.98	2.51	2.70
16	2.65	3.73	3.16	3.13	3.31	3.18	3.20
RMSD		0.584	0.429	0.522	0.320	0.513	0.366

[a] Ref[13], [b] Ref[120], [c] Ref[126], [d] Measured for NPh_2 analog, [e] TD-DFT results in Chapter 3 , [f] Partial optimization with planar constraint.
The active space chosen is shown in the parenthesis following the method as "(m,n)" where single excitations are restricted to "m" molecular orbitals (MOs) around the Fermi level and double excitations to "n" MOs, if any.

Table 4.2: Comparison of 1PA excitation energies E (eV) for different orders of excitation in CI methods at PM6 level for PM6 optimized geometries.

Excitations	⇨	CISD(10,10)/PM6	CIS(20)/PM6	CISd(20,10)/PM6		MRCIS(20)/PM6	
Geometry	⇨	PM6					
Mol. #	Exp[a,b,c]	$E(E_0^{CISD})$	$E(E_0^{CIS})$	$E(E_0^{HF})$	$E(E_0^{CISd})$	$E(E_0^{HF})$	$E(E_0^{MRCIS})$
1	4.18	4.27	3.11	2.93	4.22	3.01	3.41
2	3.32	3.45	2.74	2.50	3.25	2.50	2.91
3	3.04	3.49	2.66	2.59	3.03	2.57	2.79
4	2.90	3.06	2.56	2.45	2.78	2.42	2.63
5	2.72	2.96	2.54	2.45	2.69	2.44	2.58
6	2.53	3.24	2.60	2.49	2.92	2.49	2.92
7	2.42	2.87	2.44	2.36	2.63	2.34	2.51
8	2.24	2.86	2.58	2.53	2.65	2.51	2.61
9	2.01	3.05	2.60	2.57	2.63	2.59	2.61
10	2.92[d]	3.75	2.99	2.96	3.15	3.00	3.08
11	2.83	3.53	3.03	2.93	3.25	2.94	3.08
12	3.18	3.46	2.71	2.47	3.34	2.52	2.84
13	3.01	3.46	2.67	2.50	3.30	2.49	2.78
14	2.88	3.20	2.67	2.49	3.04	2.51	2.73
15	2.76	3.21	2.63	2.50	2.98	2.51	2.70
16	2.65	3.73	3.16	3.13	3.31	3.18	3.20
RMSD		0.584	0.429	0.522	0.320	0.513	0.366

[a] Ref[13], [b] Ref[120], [c] Ref[126], [d] Measured for NPh_2 analog.

The accuracy with the multi-reference wavefunctions can be improved in two ways: (a) including double excitations and (b) considering higher order excited reference determinants, for the calculation of optical properties.

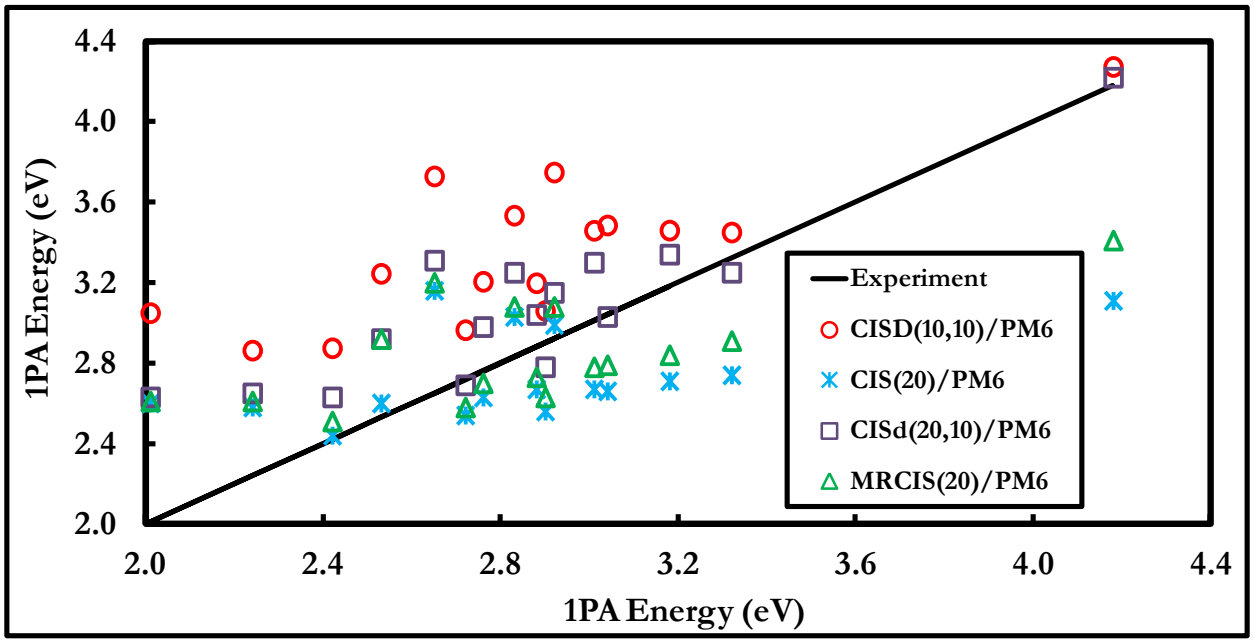

Figure 4.1: Scattered 1PA energy plots relative to experimental values for different orders of excitation and active spaces in CI methods at PM6 level for PM6 optimized geometries. The active space chosen is shown in the parenthesis following the method as "(m,n)" where single excitations are restricted to "m" molecular orbitals (MOs) around the Fermi level and double excitations to "n" MOs, if any.

Figure 4.1 plots the 1PA energies for various CI methods at PM6 level for PM6 optimized geometries in addition to the experimental values for molecules under study. We observe the energies to be overestimated at CISD(10,10) level for the entire set. However, CIS(20) method underestimates them for most of the molecules, although improving the overall agreement with the experiment. The predicted values for CISd(20,10) stay either close to the experimental line or are slightly overestimated and offer the best agreement amongst all the methods considered in this figure. The slight deterioration for the MRCIS(20) method as compared to the CISd(20,10) is mainly due to the highly underestimated predicted energy value

for molecule 16 in the former case. The more accurate prediction of 1PA energies for molecule 16 for CISd(20,10) and CISD(10,10) methods focus on the importance of the double substitutions for prediction of 1PA observables for organic molecules of donor-π-donor types. The 1PA energies at MRCIS(20,10) level stay fairly close to the experimental line though does not follow any specific trend.

In Chapter 3, we witnessed the best agreement with the experiment for the equilibrium geometries obtained at the M05-2X/6-31G* level without any additional constraint amongst all the other DFT optimization levels. For this reason, we choose to calculate the 1PA excitation energies at PM6 level for different CI methods for M05-2X/6-31G* geometries as depicted in Table 4.3. The M05-2X geometries are indeed observed to perform better than the PM6 ones at PM6 level but not as good as the corresponding TD-DFT predictions. The agreement with the experiment improves for about 0.05-0.1eV for different CI methods considered in comparison to the PM6 geometries. However, the trends shown for PM6 geometries hold true for M05-2X ones as well. We observe the overall improvement of around 0.1eV with the increase in the size of the active space from ten to twenty. For the same size of the active space, inclusion of the double excitations CISd(20,10) seem to play a major role in improving the agreement by 0.14eV. At the same time, single electronic substitutions in the multi-reference HF determinant MRCIS(20) improves the agreement over single reference CIS(20) method. In summary, the 1PA energetics are highly sensitive to the order of excitation and the size of the active space considered. The choice of the geometry is also observed to affect the energy predictions.

Table 4.3: Comparison of 1PA excitation energies E (eV) for different orders of excitation in CI methods using PM6 Hamiltonian for geometries optimized at M05-2X/6-31G* level.

Excitations	⇨	TD/B3LYP*[e]	CISD(10,10)/PM6	CIS(20)/PM6	CISd(20,10)/PM6		MRCIS(20)/PM6	
Geometry	⇨	M05-2X/6-31G*						
Mol. #	Exp[a,b,c]	$E(E_0^{B3LYP})$	$E(E_0^{CISD})$	$E(E_0^{CIS})$	$E(E_0^{HF})$	$E(E_0^{CISd})$	$E(E_0^{HF})$	$E(E_0^{MRCIS})$
1	4.18	4.10	4.32	3.17	3.00	4.27	3.07	3.47
2	3.32	3.53	3.48	2.78	2.53	3.35	2.56	2.96
3	3.04	3.01	3.64	2.73	2.67	3.13	2.63	2.85
4	2.90	2.91	3.16	2.64	2.55	2.85	2.52	2.73
5	2.72	2.59	2.98	2.57	2.48	2.70	2.47	2.62
6	2.53	2.60	3.16	2.64	2.54	2.90	2.53	2.63
7	2.42	2.23	2.92	2.49	2.41	2.68	2.40	2.56
8	2.24	2.08	2.89	2.63	2.58	2.70	2.58	2.67
9	2.01	1.74	2.86	2.51	2.46	2.57	2.46	2.50
10	2.92[d]	2.93	3.32	2.77	2.72	2.93	2.68	2.78
11	2.83	2.89	3.41	2.73	2.63	3.05	2.58	2.77
12	3.18	3.24	3.48	2.73	2.52	3.36	2.53	2.88
13	3.01	2.96	3.44	2.66	2.49	3.29	2.47	2.76
14	2.88	2.78	3.11	2.63	2.47	2.93	2.46	2.70
15	2.76	2.58	3.10	2.57	2.45	2.87	2.43	2.63
16	2.65	2.45	3.03	2.70	2.65	2.84	2.74	2.81
RMSD		0.137	0.462	0.384	0.483	0.244	0.477	0.298

[a] Ref[13], [b] Ref[120], [c] Ref[126], [d] Measured for NPh_2 analog, [e] TD-DFT results in Chapter 3.

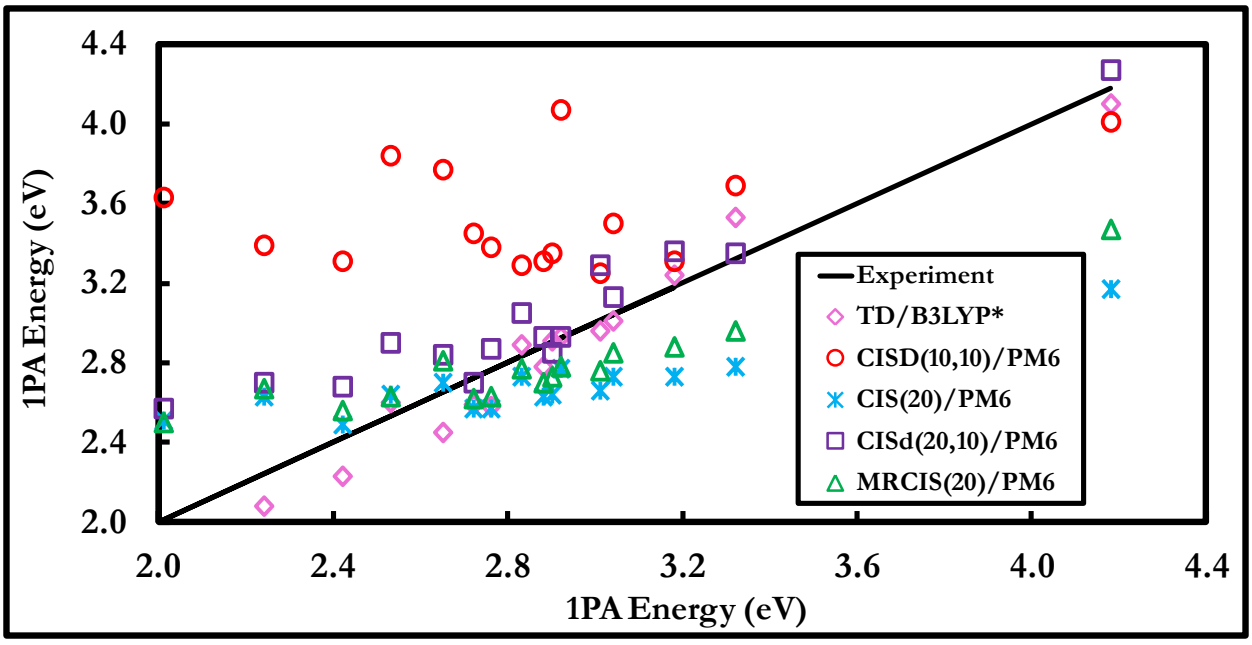

Figure 4.2: Scattered 1PA energy plots for different CI methods at PM6 and TD-DFT calculations at B3LYP/6-31G* level for M05-2X/6-31G* optimized geometries compared to experimental values.

The scattered 1PA energy plots are shown in Figure 4.2 for different CI/PM6 schemes for the unconstrained M05-2X/6-31G* geometry. The corresponding TD-DFT predictions at B3LYP/6-31G* level are also shown for comparison. The trends observed for CISD(10,10) and CIS(20) methods are similar to the ones shown in Figure 4.1. The CISd(20,10) method stay on the experimental line whereas the energies are predicted to be slightly underestimated by the MRCIS(20) method. Thus, CISd(20,10) method for M05-2X/6-31G* geometries offers the best agreement with the experiment for prediction of 1PA energetics amongst all the other semiempirical choices considered so far whereas the overall agreement for MRCIS(20) method for the same geometry is only off by 22%.

4.2.2 Two-Photon Excitation Energies and Cross-Sections for Different CI Methods

Table 4.4 represents the 2PA energies calculated using CISd(20,10) and MRCIS(20) methods at PM6 level for M05-2X/6-31G* geometries. In contrast to the trends observed for the 1PA energetics, the MRCIS(20) method now largely improves the agreement by about 30% (0.2eV) over CISd(20,10) method. However, the agreement with the experiment is deteriorated in comparison to the 1PA energies. On the other hand, the 2PA cross-sections calculated for both CISd(20,10) and MRCIS(20) methods are so out of range and they could not be plotted on the same scale as demonstrated in Table 4.5. They are not considered meaningful for most of the molecules to compare to the experiment and the TD-DFT/ATDA predictions for the same geometry. The overall RMSD for CISd(20,10) and MRCIS(20) methods differ by two and three orders of magnitude from the ATDA, respectively. Although both the methods overestimate the cross-sections, the MRCIS(20) does improve the agreement in comparison to the CISd(20,10) for some of the molecules. To our surprise, the CISd(20,10) method shows fairly good improvement of the cross-sections than ATDA for molecules 1, 6, 10 and 13. We know from Table 4.3 that the CISd(20,10) method predicts the 1PA excitation energies closest to the experiment. Hence, the overall improvement of the CISd(20,10) method over MRCIS(20) suggests the importance of the correct description of 1PA states for the calculation of 2PA cross-sections. The effect due to the underestimated detuning factors for different CI methods are somewhat neglected by multiplying the 2PA cross-sections with the squares of the ratios of their detuning to the experimental one. The cross-sections reported with an explicit (not included in the SOS formalism) correction to the detuning improves the agreement with the experiment to about 62% for CISd(20,10) and 76% for MRCIS(20) methods.

Table 4.4: Comparison of 2PA excitation energies E (eV) for different orders of excitation in CI methods at PM6 level for M05-2X/6-31G* geometries.

Excitations	⇨	TD/B3LYP/6-31G*[e,g]	CISd(20,10)/PM6	MRCIS(20)/PM6
Geometry	⇨	M05-2X/6-31G*		
Mol. #	Exp[a,b,c]	$E(E_0^{B3LYP})$	$E(E_0^{CISd})$	$E(E_0^{MRCIS})$
1	2.41	2.61	3.46	2.41
2	2.05	2.17	2.91	1.99
3	1.70	1.76	2.32	2.15
4	1.70	1.74	2.06	2.00
5	1.60	1.53	1.94	1.98
6	1.50	1.51	2.06	1.87
7	1.32	1.28	1.97	1.94
8	1.28	1.20	1.87	1.85
9	1.27	0.98	1.93	1.91
10	1.55[d]	1.68	2.13	1.99
11	1.57	1.63	2.25	2.03
12	1.94	1.96	2.13	1.92
13	1.75	1.78	2.13	1.86
14	1.70	1.66	1.93	1.87
15	1.70	1.55	1.92	1.88
16	1.48	1.42	2.13	2.25
RMSD		0.113	0.586	0.416

[a] Ref[13], [b] Ref[120], [c] Ref[126], [d] Measured for NPh_2 analog, [e] TD-DFT results in Chapter 3, [g] NStates=6.

Table 4.5: Comparison of 2PA cross-sections $\sigma(\omega_{2PA})$ (GM) for different orders of excitation in CI methods at PM6 level for M05-2X/6-31G* geometries.

Excitations	⟹	ATDA/B3LYP/6-31G*[e,g]	CISd(20,10)/PM6		MRCIS(20)/PM6	
Geometry	⟹	M05-2X/6-31G*				
Mol. #	Exp[a,b,c]	$\sigma(\omega_{2PA})$	$\sigma(\omega_{2PA})$	$\sigma(\omega_{2PA})(D^2_{CISd}/D^2_{Exp})$	$\sigma(\omega_{2PA})$	$\sigma(\omega_{2PA})(D^2_{MRCIS}/D^2_{Exp})$
1	12	130	93	19	51	6
2	210	283	963	116	46	8
3	995	827	13068	4775	2958	302
4	900	782	5967	2586	1270	161
5	1250	1216	16442	7571	109339	12137
6	1750	505	978	650	467	85
7	620	1280	16051	6687	24508	3039
8	1750	2115	5110	3820	7571	1989
9	4400	2229	31332	23436	57137	10523
10	450[d]	640	2294	782	1122	152
11	890	388	6417	2587	3822	501
12	260	523	396	390	648	122
13	320	799	446	378	524	93
14	425	1184	4653	3342	7296	1220
15	1300	1687	12760	10249	22070	3401
16	1420	1301	171664	63216	667515	57351
RMSD		717	43692	16530	169419	39790

[a] Ref[13], [b] Ref[120], [c] Ref[126], [d] Measured for NPh_2 analog, [e] TD-DFT results in Chapter 3, [g] NStates=6.

The second columns for each of the CI methods shown depict the cross-sections neglecting the effect of the underestimated detuning factors (D) defined as $\left(\omega_{1PA} - \frac{\omega_{2PA}}{2}\right)$.

Table 4.6: Scalar values of transition dipole moments μ (a.u.) using different orders of excitations in CI methods at PM6 level for M05-2X/6-31G* optimized geometries.

Excitations	ATDA/B3LYP/6-31G*[e,g]		CIS(20)/PM6	CISd(20,10)/PM6	MRCIS(20)/PM6	
Geometry	M05-2X/6-31G*					
Mol. #	$\langle S_0\|\mu\|S_1\rangle$	$\langle S_1\|\mu\|S_X\rangle$	$\langle S_1\|\mu\|S_Y\rangle$			$\langle S_Y\|\mu\|S_Z\rangle$
1	3.09	3.15	1.49	2.22	2.01	7
2	4.00	3.93	1.77	2.21	2.32	14
3	5.32	5.83	2.37	4.73	4.65	34
4	5.18	5.29	5.43	3.08	3.02	42
5	6.56	6.62	3.62	5.05	5.61	94
6	4.62	5.85	6.88	3.39	3.28	26
7	5.94	7.34	4.06	5.90	5.98	83
8	6.73	4.94	7.16	7.80	7.17	49
9	6.66	9.30	8.39	7.69	7.87	91
10	5.18	5.98	8.91	3.38	3.29	39
11	4.94	6.47	3.96	5.03	5.27	41
12	4.90	4.66	5.83	3.82	4.13	30
13	5.71	5.33	4.62	3.48	3.91	28
14	6.39	5.94	4.61	5.29	6.23	59
15	7.05	6.55	7.54	5.95	7.32	80
16	7.06	7.42	8.94	7.22	8.16	248
RMSD			1.95	1.29	1.18	77

[e] TD-DFT results in Chapter 3, [g] NStates=6.

The ground-to-excited state transition dipoles are reported for CIS(20), CISd(20,10) and MRCIS(20) methods whereas excited-to-excited state dipoles are shown only for MRCIS(20) method. Here S_0 is ground, S_1 is 1PA and S_X is 2PA excited state for ATDA method, S_1, S_Y and S_Z are ground, 1PA and 2PA states for the CI methods, respectively. The RMSDs are obtained relative to ATDA predictions at B3LYP/6-31G*//M05-2X/6-31G* level.

Still, the RMSD values for both these methods differ by two orders of magnitude from the ATDA predictions. From Equation 2.41, we know that the SOS formalism employs ground-to-excited and excited-to excited state transition dipole moments and the detuning between the 1PA and 2PA states. This suggests the incorrect description of the state transition dipoles at PM6 level to be the prime factor resulting in the deviation of the calculated cross-sections from the experiment and the ATDA predictions.

Table 4.6 presents the ground-to excited and excited-to-excited state transition dipoles for these methods at PM6 level for M05-2X/6-31G* geometries. The ground-to-excited state dipoles are tabulated for CIS(20), CISd(20,10) and MRCIS(20) methods whereas the excited-to-excited dipole moments are only illustrated for the MRCIS(20) method. The RMSDs of the transition dipoles are reported w.r.t the TD-DFT/ATDA formalism at B3LYP/6-31G* level for comparison. The ground-to-excited transition dipoles obtained for CIS(20) method are largely deviated from the ATDA predictions in comparison to CISd(20,10) and MRCIS(20) methods. Whereas, MRCIS(20) exhibits the closest agreement with the ATDA predictions. At the same time, the excited-to-excited state transition dipoles are largely overestimated varying by at least an order of magnitude for the entire set of molecules except for molecule 1. The closest agreement of the 2PA cross-section value to the experiment for molecule 1 and the largest deviation for molecule 16 can be understood easily in terms of their excited-to-excited transition dipole moments. The dipole value for molecule 1 is of the same order as for ATDA whereas for molecule 16 is off by two orders in magnitude. Thus, we can see that the highly overestimated excited-to-excited state transition dipole moments predicted at PM6 level for the considered set of molecules result in the huge overestimation of their cross-section values.

Table 4.7: Comparison of 2PA energies E (eV) for ZINDO/S/CIS method with TD-DFT level for planar HF/6-31G geometries.

Excitations	⇨	TD/B3LYP/6-31G[e]	CISd(20,10)/PM6	MRCIS(20)/PM6	ZINDO/S/CIS	
Geometry	⇨	POpt[f]HF/6-31G	M05-2X/6-31G*		POpt[f]HF/6-31G	
Mol. #	Exp[a,b,c]	$E(E_0^{B3LYP})$	$E(E_0^{CISd})$	$E(E_0^{MRCIS})$	$(g_{1,\pi})p^h$	$E(E_0^{ZINDO/S})$
1	2.41	2.68	3.46	2.41	0.626	3.02
2	2.05	2.19	2.91	1.99	0.507	2.41
3	1.70	1.77	2.32	2.15	0.498	2.24
4	1.70	1.73	2.06	2.00	0.478	2.16
5	1.60	1.56	1.94	1.98	0.464	2.04
6	1.50	1.52	2.06	1.87	0.416	2.10
7	1.50	1.33	1.97	1.94	0.413	1.92
8	1.28	1.19	1.87	1.85	-	1.19[i]
9	1.27	1.01	1.93	1.91	0.381	1.69
10	1.55[d]	1.67	2.13	1.99	-	1.67[i]
11	1.57	1.63	2.25	2.03	0.483	2.09
12	1.94	1.98	2.13	1.92	0.517	2.30
13	1.75	1.82	2.13	1.86	0.505	2.18
14	1.70	1.69	1.93	1.87	0.496	2.10
15	1.70	1.59	1.92	1.88	0.481	2.02
16	1.48	1.44	2.13	2.25	0.450	2.03
RMSD		0.123	0.586	0.416	-	0.439

[a] Ref[13], [b] Ref[120], [c] Ref[126], [d] Measured for NPh_2 analog, [e] TD-DFT results in Chapter 3, [f] Partial optimization with planar constraint, [h] Slater-Condon factors, [i] Calculated from the TD-DFT calculations at B3LYP/6-31G//POpt[f]HF/6-31G level in Chapter 3.

The energy predictions for CISd(20,10)/PM6 and MRCIS(20)/PM6 methods are also shown for M05-2X/6-31G* geometries. 2PA excitations are computed by fitting 1PA energies to experiment by varying the Slater-Condon factors for $(g_{1,\pi})$ p-type π orbitals from its default value of 0.585.

4.3 Spectroscopic Parameterization (ZINDO/S)

4.3.1 Two-Photon Excitation Energies

Table 4.7 compares the 2PA excitation energies calculated with the semiempirical ZINDO Hamiltonian supplemented with the CIS scheme for planar HF/6-31G geometries to the corresponding TD/B3LYP/6-31G and experimental measurements.[13, 120, 126] The predicted values from CISd(20,10) and MRCIS(20) methods at PM6 level for M05-2X/6-31G* are also reported for completeness. The ZINDO/S/CIS calculations improve over CISd(20,10)/PM6 method by about 25%, while the 2PA energy predictions are deteriorated by 5% in comparison to the MRCIS(20)/PM6 method.

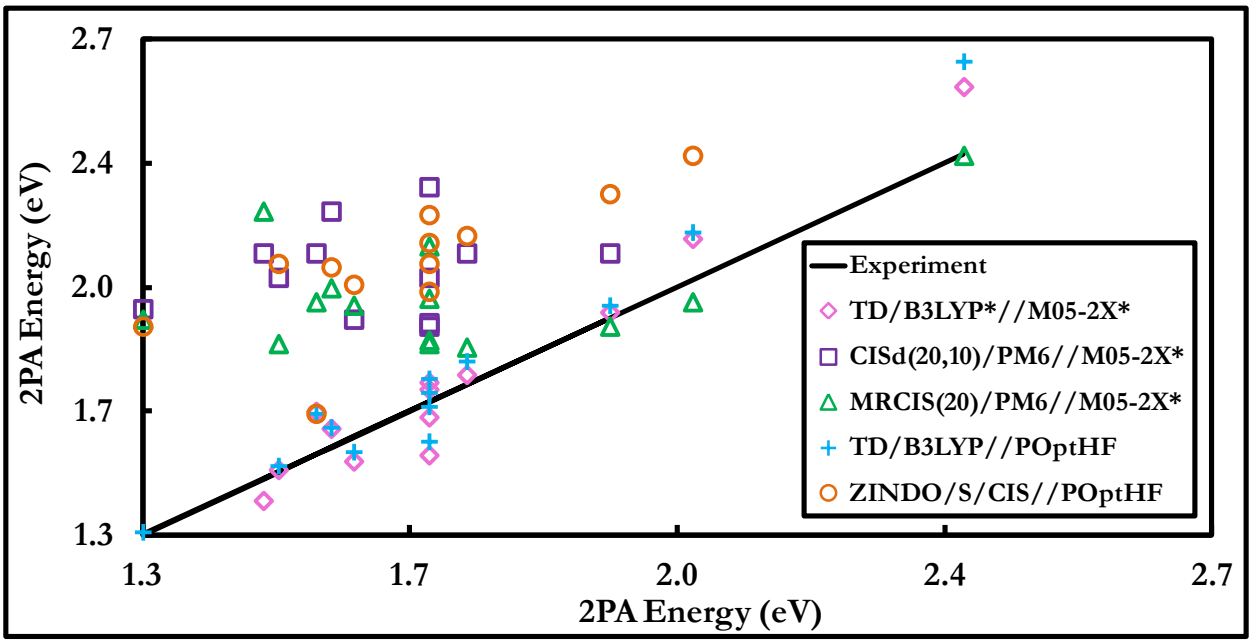

Figure 4.3: Scattered 2PA energy plots relative to experiment using different orders of excitation in CI methods at PM6 level for PM6 geometries and ZINDO/S/CIS method for M05-2X/6-31G* ones.
The "functional1//functional2" indicates, first the DFT model used for the calculation of the energetics, and second the functional used to obtain the geometry of the molecule.

The slight improvement of the MRCIS(20)/PM6 method over ZINDO/S/CIS for 2PA energy predictions is attributed to the choice of the DFT method used for geometry optimization.

Figure 4.3 depicts the scattered 2PA energies for different semiempirical methods with their respective geometry equivalent TD-DFT ones. The various CI methods at PM6 level are demonstrated for unconstrained M05-2X/6-31G* geometries whereas the ZINDO/S/CIS method is for planar HF/6-31G geometries. The 2PA excitation energies calculated at CISd(20,10)/PM6 level are overestimated for the entire set of molecules. This overestimation is somewhat corrected by the ZINDO/S/CIS method. However, MRCIS(20)/PM6 method further corrects this overestimation in the energies in agreement with the experiment. The TD-DFT predictions at B3LYP/6-31G and B3LYP/6-31G* level for HF/6-31G and M05-2X/6-31G* geometries stay close to the experimental line, respectively.

4.3.2 Two-Photon Cross-Sections

Table 4.8 compares the 2PA cross-sections obtained using the ZINDO/S/CIS method with predicted TD-DFT (ATDA, QRSR, QRDR) ones at B3LYP/6-31G level for planar HF/6-31G geometries. The cross-sections calculated using ZINDO/S/CIS method vary by an order of magnitude for most of the molecules under study. This results in the overall RMSD to be twice in disagreement in comparison to the various DFT methods. However, they are still in the same range and are vaguely comparable to the DFT formalisms unlike the CI predictions at PM6 level. The effect arising due to the deviation in the detuning factors from the experiment is somewhat neglected by multiplying the cross-sections with the squares of the ratios of their detuning to the experimental one as shown in the last column of Table 4.8.

Table 4.8: Comparison of 2PA cross-sections σ(ω2PA) (GM) for ZINDO/S/CIS method with different DFT formalisms for planar HF/6-31G geometries.

Excitations	⇨	TD/B3LYP/6-31G[e]				ZINDO/S/CIS	
Geometry	⇨	POpt[f]HF/6-31G					
# of States	⇨	N=6	N=30	N=3AG	N=3AG,3BU	N=40	
Mol. #	Exp[a,b,c]	ATDA		QRSR	QRDR	$\sigma(\omega_{2PA})$	$\sigma(\omega_{2PA})(D^2_{ZINDO/S}/D^2_{Exp})$
1	12	129	117	137	156	653	280
2	200	279	233	306	378	1077	553
3	995	848	573	1030	1565	2611	931
4	900	828	610	1002	1394	2441	928
5	1250	1125	1135	2047	2295	3990	1471
6	1750	468	447	658	708	1424	248
7	620	1339	1011	1674	2283	5897	1218
8	1750	2277	1524	2879	3758	2277[j]	2724[j]
9	4400	2262	1738	2803	3671	8325	1557
10	450[d]	682	588	886	1344	682[j]	568[j]
11	890	528	525	930	943	2038	703
12	260	507	407	547	705	1751	882
13	320	700	634	876	999	2521	1094
14	425	1028	916	1314	1519	3435	1501
15	1300	1428	1253	1881	2198	4382	2136
16	1420	1703	1024	2596	4478	6224	1748
RMSD		704	788	786	1197	2590	965

[a] Ref[13], [b] Ref[120], [c] Ref[126], [d] Measured for NPh_2 analog, [e] TD-DFT results in Chapter 3, [f] Partial optimization with planar constraint, [j] Calculated from the ATDA method at B3LYP/6-31G//POpt[f]HF/6-31G level with NStates=6 in Chapter 3.The last column of the table shows 2PA cross-sections for ZINDO/S/CIS method with the neglect of the effect of the underestimated detuning factors (D)..

Table 4.9: Comparison of scalar values of ground-to-excited and excited-to-excited state transition dipole moments μ (a.u.) for ZINDO/S/CIS method with ATDA/B3LYP/6-31G predictions for planar HF/6-31G geometries.

Excitations	⇨		ATDA/B3LYP/6-31G[e]		ZINDO/S/CIS	
Geometry	⇨		Popt[f]HF/6-31G			
Mol. #	X	Y	$\langle S_0\|\mu\|S_1\rangle$	$\langle S_1\|\mu\|S_X\rangle$	$\langle S_0\|\mu\|S_1\rangle$	$\langle S_1\|\mu\|S_Y\rangle$
1	4	9	3.10	3.20	3.34	4.52
2	4	6	3.98	4.08	3.73	5.19
3	2	7	5.31	6.07	4.93	5.87
4	2	7	5.30	5.56	4.72	5.57
5	2	8	6.43	6.88	5.69	4.52
6	3	16	4.52	6.10	4.25	1.70
7	2	16	5.90	7.34	5.80	4.97
8	4	-	6.80	8.02	6.80[j]	8.02[j]
9	2	21	6.46	9.57	6.06	4.70
10	2	-	5.30	6.16	5.30[j]	6.16[j]
11	2	9	5.16	6.57	4.97	4.91
12	2	6	4.82	4.83	4.45	5.72
13	2	6	5.52	5.52	5.05	6.06
14	2	6	6.15	6.20	5.58	6.34
15	2	6	6.72	3.92	6.04	6.50
16	2	11	6.74	7.80	6.37	6.05
RMSD					0.41	2.10

[e] TD-DFT results in Chapter 3, [f] Partial optimization with planar constraint, [j] Calculated from the ATDA method at B3LYP/6-31G//POpt[f]HF/6-31G level with NStates=6 in Chapter 3.

Here S_0 is ground and S_1 is 1PA excited state for both methods, while S_X and S_Y are 2PA excited states for ATDA and ZINDO/S/CIS methods, respectively. The RMSDs are calculated relative to ATDA predictions.

Table 4.10: Comparison of ground-to-excited (μ_{01}) and excited-to-excited (μ_{1Y}, μ_{1X}) state transition dipole moments (a.u.), detuning (D) factors (eV), and 2PA cross-sections (σ) (GM) of ZINDO/S/CIS and ATDA/B3LYP/6-31G methods for planar HF/6-31G geometries.

Mol. #	$\lvert\mu_{01}\rvert^2_{ZINDO/S}/\lvert\mu_{01}\rvert^2_{ATDA}$	$\lvert\mu_{1Y}\rvert^2_{ZINDO/S}/\lvert\mu_{1X}\rvert^2_{ATDA}$	$D^2_{ATDA}/D^2_{ZINDO/S}$	$\sigma_{ZINDO/S}/\sigma_{ATDA}$
1	1.16	2.00	1.79	5.06
2	0.88	1.62	2.43	3.86
3	0.86	0.94	2.60	3.08
4	0.79	1.00	2.59	2.95
5	0.78	0.43	2.66	3.55
6	0.88	0.08	6.91	3.04
7	0.97	0.46	3.76	4.40
8	-	-	-	-
9	0.88	0.24	4.79	3.68
10	-	-	-	-
11	0.93	0.56	2.76	3.86
12	0.85	1.40	2.32	3.45
13	0.84	1.21	2.30	3.60
14	0.82	1.05	2.37	3.34
15	0.81	2.75	2.37	3.07
16	0.89	0.60	3.21	3.65

The agreement of these corrected 2PA cross-section values with the experiment improve largely by about 63% in comparison to the ones predicted otherwise. Thus, the cross-sections with the neglect of deviation due to the overestimated 2PA energies follow the same order as experiment for most of the molecules. In addition, molecules 3, 4 and 11 are observed to exhibit the closest agreement to the experiment in comparison to all the other methods shown in the table. The overall RMSD for the corrected 2PA cross-sections improve over the QRDR method by about 19%. However, it is still deteriorated from the QRSR and the ATDA methods by less than 20%. From the observed trends, we can infer that the deviation of the predicted 2PA cross-sections from the experiment is mainly due to the overestimation of the 2PA excitation energies calculated using the ZINDO/S/CIS method. However, the discrepancies in the 2PA cross-section values from the experiment and the best TD-DFT predictions even after the neglect of the deviation in the energetics is attributed to the level of accuracy in the prediction of ground- or excited- state transition dipoles by this method.

Table 4.9 compares the ground-to-excited and excited-to-excited state transition dipole moments at ZINDO/S/CIS level to ATDA/B3LYP/6-31G for planar HF/6-31G geometries. The RMSDs of the transition dipoles are reported w.r.t to the ATDA method in this table. The ground-to-excited and excited-to-excited state transition dipoles deviate by 0.4D and 2.1D, from the corresponding ATDA predictions, respectively. Table 4.10 further investigates the factors responsible for the incorrect prediction of the 2PA cross-sections for the ZINDO/S/CIS method by employing the SOS formalism (Equation 2.41). Here, we report the ratios of the ground- and excited- state transition dipoles, detuning between the 1PA and 2PA states and 2PA cross-section values of the ZINDO/S/CIS method to the ATDA. The ground-to-excited state dipole moments for the ZINDOS/S/CIS method are very close to the ATDA ones. At the same time, the amount

of deviation from the ATDA method for excited-state transition dipoles is much smaller in comparison to the observed deviation in their cross-section values. However, we notice that the ratios of the detuning factors for both the methods are close to the inverse of the measured ratios of their cross-sections. This confirms that the major cause of the disagreement of the 2PA cross-sections using the ZINDO/S/CIS method is the overestimation in the prediction of 2PA excitation energies by this method in comparison to the experiment and the best TD-DFT predictions.

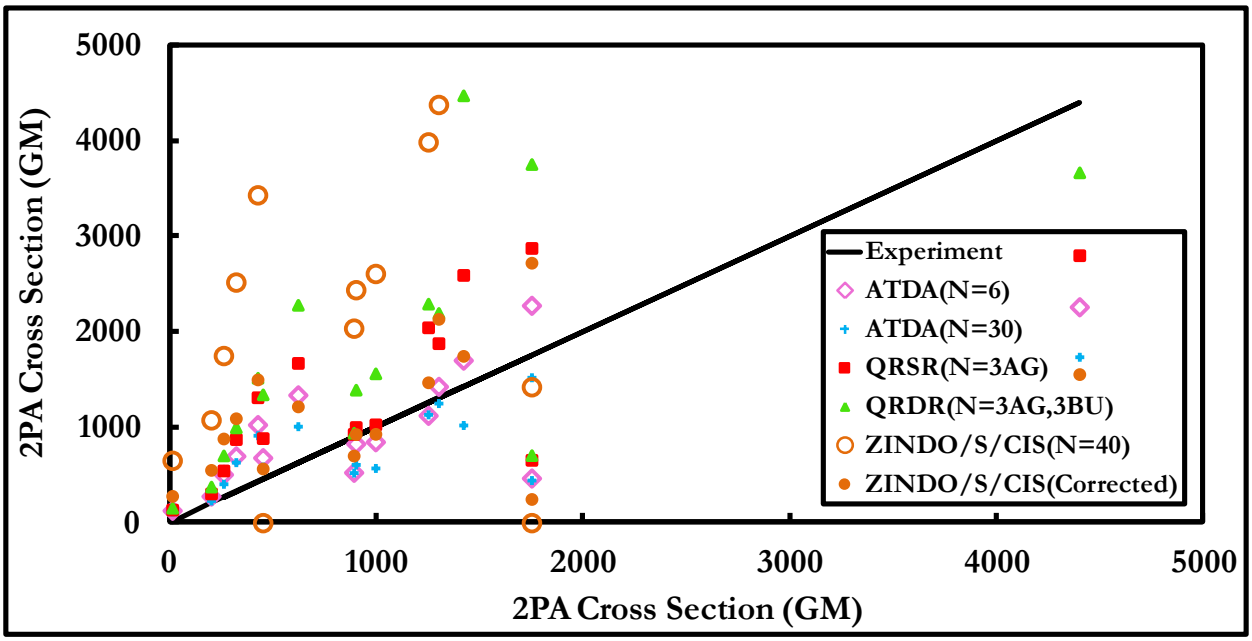

Figure 4.4: Scattered 2PA cross-section plots relative to experiment using ZINDO/S/CIS method for POpt HF/6-31G geometries.
The ZINDO/S/CIS(Corrected) plots the cross-section values with the neglect of the deviation of the detuning factor in comparison to experiment. The TD-DFT computations using ATDA, QRSR and QRDR methods at B3LYP/6-31G//POptHF/6-31G level are also represented. Number of singlet excited states employed by SOS formalism is depicted in the parenthesis following the method.

Figure 4.4 illustrates the scattered 2PA cross-sections for ZINDO/S/CIS method with different DFT formalisms at TD/B3LYP/6-31G level for the planar HF/6-31G geometry. The cross-sections obtained at the ZINDO/S/CIS level are overestimated for most of the molecules

under study. However, the cross-sections calculated with the neglect of the overestimation in excitation energies for this method largely corrects the deviation from the experimental line for all the molecules, bringing them closer to the best TD-DFT (ATDA and QRSR) predictions.

We demonstrate the ground-to-excited state transition dipole moments for different semiempirical methods with their geometry equivalent TD-DFT predictions in Figure 4.5. The different CI methods at PM6 level are shown for unconstrained M05-2X/6-31G* geometries, while the ZINDO/S/CIS method is for planar HF/6-31G geometries. The ground-to-excited transition dipoles predicted at CISd(20,10)/PM6 level are meagerly underestimated for the entire set of molecules. The dipole moments for the MRCIS(20)/PM6 method are close to the ones calculated at ZINDO/S/CIS level, while CISd(20,10)/PM6 being closest to the TD-DFT/ATDA predictions.

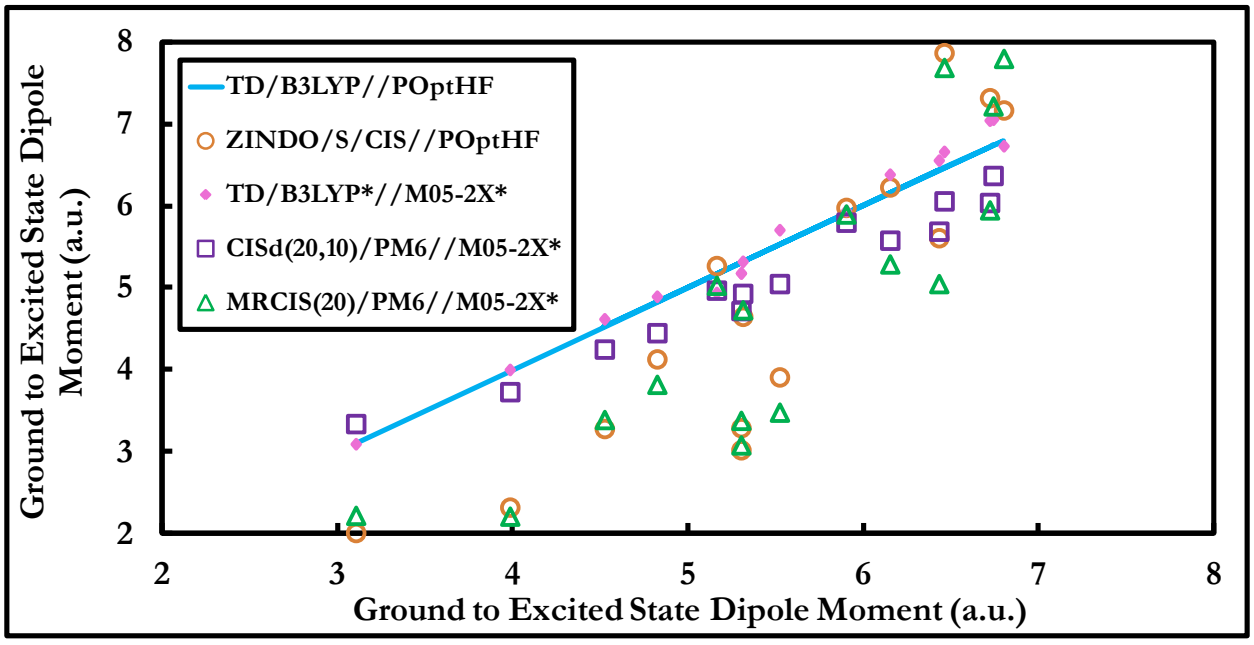

Figure 4.5: Scattered plots for scalar values of ground-to-excited state transition dipole moments (a.u.) for different CI methods at PM6 level for PM6 geometries and ZINDO/S/CIS method for M05-2X/6-31G* ones.

Figure 4.6 presents the excited-to-excited state transition dipoles for the ZINDO/S/CIS and ATDA/B3LYP/6-31G methods for planar HF/6-31G geometries. The moments calculated using ZINDO/S/CIS method are scattered averagely above and below the TD-DFT/ATDA dipole line. The dipoles for most of the molecules are either overestimated or underestimated with few on the line. Overall the agreement with the experiment is good.

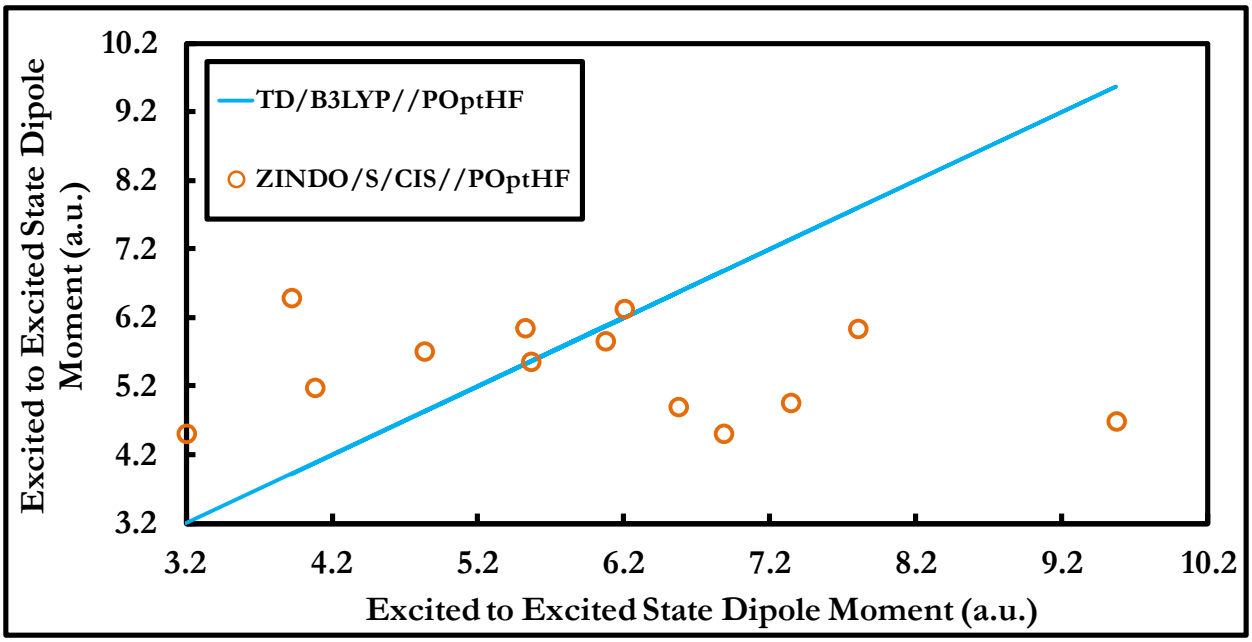

Figure 4.6: Scattered plots for scalar values of excited-to-excited state transition dipole moments (a.u.) for ZINDO/S/CIS method for POpt HF/6-31G geometries.
The transition dipoles predicted for CISd(20,10)/PM6 and MRCIS(20)/PM6 methods are so out of range that they could not be plotted on the same scale and cannot be considered meaningful.

The excited-to-excited dipoles for CISd(20,10)/PM6 and MRCIS(20)/PM6 methods are so high and out of range and they could not be even plotted on the same scale.

4.4 Comparison of Semiempirical Theory Levels

Here, we compare the performance of different semiempirical theory levels for 1PA and 2PA predictions. The spectroscopic parameterized ZINDO/S/CIS method[105] implemented in

Gaussian09[144] allows to choose a large CI active space. However, Zojer *et al.*[15] suggested to include the doubly, triply and quadruply excited determinants in the CI configurations for more quantitative 2PA predictions in π-conjugated molecules. Therefore, we choose molecule 3 as a representative example to calculate the 1PA and 2PA properties using different orders of excitation within the CI methods, as implemented in Zerner's code[145] performing INDO[106] type of calculations (ZINDO/S). The detailed comparison of the ZINDO/S method[145] for different orders of excitation and active space with spectroscopic parameterized ZINDO/S/CIS method[105] and general purpose PM6 calculations[142] with different CI methods is presented in Table 4.11 for molecule 3. The table reports the 1PA and 2PA excitation energies, ground-to-excited and excited-to-excited transition dipole moments for the ZINDO/S[145] method with CIS(20), CISd(10,5) and MRCIS(10) schemes using M05-2X/6-31G* optimized geometries. The excitations for the MRCIS(10) method are calculated from two to seven singly and doubly excited reference configurations added to the ground state HF wavefunction as listed in Figure 4.S2. The TD-DFT predictions reported in Chapter 3 for the same geometry are also shown for comparison.

We focus on the dependence of results on the order of excitation, size of active space and choice of reference determinants as applied to molecule 3. We observe the excited states formed by the single excitations within the larger active space for ZINDO/S/CIS(20) method plays an important role for the prediction of 1PA and 2PA excitation energies in agreement with the experiment and the best TD-DFT predictions as opposed to the inclusion of the double excitations within a relatively smaller active space for ZINDO/S/CISd(10,5). The use of more than one reference determinant for ZINDO/S/MRCIS(10) method is shown to improve the agreement for 2PA observables (excitation energies and excited-to-excited state transition dipole

moments). However, it is not merely the inclusion of more reference determinants for the excited state calculation, but their specific choice involving the transitions from the unoccupied set of orbitals to the occupied ones which are useful for improved predictions. We observe a relative deterioration in the 1PA excitation energy value when the electronic configuration built by simultaneously promoting one electron from HOMO-1 to LUMO and one from HOMO to LUMO+1 as represented by "H-1, H to L, L+1" configuration in Table 4.S2. Still, the choice for the proper reference configuration remains an open question as discussed earlier.[17, 19] The best predictions are purely obtained on the trial and error basis.

We observe the best predictions using the ZINDO/S method[145] combined with MRCIS(10,5) scheme are comparable to the earlier discussed ZINDO/S/CIS method[105] for molecule 3. However, the results can be further improved by allowing: (a) larger size of the active space, (b) higher order excitations (c) triply and quadruply excited determinants in the CI wavefunction. At the same time, the ZINDO/S method[145] drastically improves over the PM6 method[142] combined with the same CI configurations. The excited-to-excited state transition dipole moments obtained using ZINDO/S method[145] are much closer to the ones obtained at ZINDO/S/CIS[105] and earlier reported TD-DFT predictions than the ones calculated at PM6 level.[142] Owing to the lack of a consistent criterion for the choice of reference configurations reported , we are unable to suggest the use of this method for the 2PA predictions for all class of conjugated compounds at its present level of formulation and application. The detailed study of the 2PA spectra for the same set of molecules with ZINDO/S method[145] combined with different multi-reference schemes will form a separate study to benchmark its performance within the semiempirical domain.

Table 4.11: Comparison of 1PA and 2PA energies E(ω) (eV), ground-to-excited and excited-to-excited transition dipole moments μ (a.u.), and 2PA cross-sections σ(ω/2) (GM) for molecule 3 calculated using different semiempirical theory levels.

Excitations	Geometry	No. of Ref. Config.	X	Y	Z	$E(\omega_{XY})$	$E(\omega_{XZ}/2)$	$\langle S_X \mid \mu \mid S_Y \rangle$	$\langle S_Y \mid \mu \mid S_Z \rangle$	$\sigma(\omega_{XZ}/2)$
Exp[a,b,c]		1	-	-	-	3.04	1.7	-	-	995
TD/B3LYP*[e]	M05-2X*	1	0	1	2	3.01	1.76	5.32	5.83	827[j]
ZINDO/S/CIS	Popt[f]HF	1	0	1	7	3.04[k]	2.24	4.93	5.87	2611
CISD(10,10)/PM6	M05-2X*	1	1	7	-	3.64	-	4.69	-	-
CIS(20)/PM6		1	1	7	-	2.73	-	2.37	-	-
CISd(20,10)/PM6		-	1	7	26	3.53	2.23	4.73	84.31	13068
MRCIS(20)/PM6		-	1	7	25	4.17	2.15	4.65	34.28	2958
ZINDO/S/CIS(20)	M05-2X*	1	1	2	7	3.53	2.47	5.20	6.92	-
ZINDO/S/CISd(10,5)		1	1	2	6	4.17	2.79	4.77	5.05	-
ZINDO/S/MRCIS(10)		3	1	2	3	3.71	2.18	4.53	5.00	-
		4	1	2	3	3.50	2.12	4.53	4.10	-
		5	1	2	3	3.93	2.20	4.44	4.90	-
		6	1	2	3	3.78	2.15	4.48	5.24	-
		8	1	2	3	3.73	2.14	4.47	5.15	-

[a] Ref[13], [b] Ref[120], [c] Ref[126], [d] Measured for NPh_2 analog, [e] TD-DFT results in Chapter 3, [f] Partial optimization with planar constraint, [k] Empirically fitted to match experimental 1PA energy, [j] Calculated from the ATDA method at B3LYP/6-31G//POpt[f]HF/6-31G level with NStates=6 in Chapter 3.

Here, S_X, S_Y and S_Z are the ground, 1PA and 2PA states, respectively.

Now, we provide a detailed one-to-one correspondence of 1PA and 2PA observables calculated using the ZINDO/S[145] and PM6[142] methods combined with various CI schemes in comparison to the experiment[13, 120, 126] and more accurate TD-DFT predictions. The 1PA excitation energy calculated by the ZINDO/S/CIS(20) method is overestimated by 0.5eV with the experiment. At the same time, the ground-to-excited transition dipole moment is observed to be very close to the best TD-DFT predictions. Whereas, the CIS(20)/PM6 method although improves the agreement for the excitation energy (by 0.2eV) but deteriorates highly in its prediction of ground-to-excited transition dipole moment. Comparing the ZINDO/S/CISd(10,5) method with that of CISd(20,10)/PM6, we observe that the 1PA and 2PA energies are largely overestimated at the ZINDO/S level. This can be attributed to the smaller size of the active space considered for single and double excitations for ZINDO/S calculations. The ground-to-excited transition dipoles predicted by both the methods are closer in agreement with the TD-DFT results. But the ZINDO method largely corrects the overestimation in the excited-to-excited state transition dipole moments reported at PM6 level. On comparison of ZINDO/S/CISd(10,5) method with the CISD(10,10)/PM6 one, we observe the 1PA energies to be closer to the experiment for PM6 methods. This is due to the larger active space for the double excitations at PM6 level although the space for the single excitations is the same for both the methods. This in turn suggests the importance of size of active space for the correct prediction of excitation energies. The use of multi-reference determinants using ZINDO program[145] is observed to be highly advantageous. Not only it helps improve the agreement for 1PA and 2PA excitation energies but provides the correct description of the state and transition dipole moments. However, these predictions are extremely sensitive to the choice of reference configurations which still remains an ambiguity.

4.5 Conclusions

We tested the performance of different semiempirical WFT methods for the prediction of 1PA and 2PA spectra for π-conjugated chromophores of substituted PPV types. The 2PA cross-sections calculated using the spectroscopic parameterized ZINDO/S[105] with single CI method provides much better agreement in comparison to the general purpose PM6[142] calculations using different CI schemes. We have shown the PM6 model Hamiltonian combined with different CI methods is not recommended for qualitative 2PA predictions and can at best be used for making quantitative predictions for various 1PA and 2PA observables. The deterioration in 2PA cross-section values for this method is primarily due to the overestimated excited-to-excited transition dipole moments. At the same time, the deviation in the 2PA cross-sections obtained with the ZINDO/S/CIS method is attributed to the overestimation in the prediction of 2PA excitation energies as compared to more accurate TD-DFT results. Also, the different parameterizations involved with the ZINDO/S/CIS method makes it difficult to establish the accuracy for general class of molecules. Apparently, the methods parameterized to reproduce 1PA spectra with the CIS fail to describe the 2PA states. The ZINDO/S method[145] combined with different orders of multi-reference CI configurations seem to provide not only an improved description of the 1PA and 2PA excited states but estimates the transition dipoles of these excitations better. However, the results are observed to be highly dependent on the specific choice for the active space, order of excitation and reference configuration.

Table 4.S1: Reference configurations considered for MRCIS(20)/PM6 method in addition to the HF ground state configuration.

Total # of Reference Configurations	Choice of Reference Configurations	
	Singly Excited	Doubly Excited
5	H to L	H,H to L,L
	H to L+1	
	H-1 to L	

Table 4.S2: Reference configurations considered for ZINDO/S/MRCIS(10) method in addition to the HF ground state configuration.

Total # of Reference Configurations	Choice of Reference Configurations	
	Singly Excited	Doubly Excited
3	H to L	H,H to L,L
4	H to L	H,H to L,L
		H-1, H to L, L+1
5	H to L	H,H to L,L
	H-1 to L	
	H to L+1	
6	H to L	H,H to L,L
	H-1 to L	H-1, H to L, L+1
	H-1 to L+1	
8	H to L	H,H to L,L
	H-1 to L	H-1, H to L, L+1
	H-1 to L+1	H,H to L, L+1
		H,H to L,L

CHAPTER 5 LOCALIZATION OF ELECTRONIC EXCITATIONS STUDIED BY DFT

In Chapters 3 and 4, we have reported the accuracy of different second and third order time dependent density functional theory (TD-DFT), and semiempirical wavefunction theory (WFT) methods for the prediction of two-photon absorption (2PA) spectra of a special class of substituted PPV [poly (p-phenylene vinylene)] oligomers. Here, we focus our attention to the study of nonlinear neutral (excitonic) and charged (polaronic) excitations responsible for electronic transport in π-conjugated organic molecules. Spin responses in π-conjugated polymer films elucidated the role of hyperfine interactions (HFI) in various organic magneto-electronic devices and the influence of hydrogen isotope exchange in MEH-PPV [poly{2-methoxy-5-(2-ethyl-hexyloxy)-PPV}] PPV on the magnetic response of spin-dependent processes. This allowed experimental evaluation of the polaronic spin density in MEH-PPV to be spread over two to three repeat units (about 10 C-H bonds).[146] This motivated us to present a linear response TD-DFT study to benchmark the ability of existing functional models to describe the extent of self-trapped neutral singlet (S_1) and triplet (T_1) excitons and positive (P^+) and negative (P^-) polarons for PPV and MEH-PPV. We observe an explicit correlation between the spatial extent of the electronic states and the fraction of the orbital exchange interaction in DFT functionals. While solvent effects are found to be negligible for neutral (S_1 and T_1) excitons, they play an important role for charged (P^+ and P^-) species. S_1 states are observed to be spatially less localized compared to the polaronic wavefunctions (P^+ and P^-). This is in contrast to the T_1 states, which exhibit more spatial confinement in comparison to P^+ and P^- states. Therefore in this study, we emphasize the crucial role played by the amount of long-range orbital exchange in the density functional and the surrounding dielectric medium in studying the spatial confinement of the

wavefunctions in accordance with experimental studies[146, 147] performed in these polymers. Interestingly, unsubstituted PPV was found to behave very similarly to MEH-PPV in its trans-isomeric form. Hence, we chose only to discuss MEH-PPV hereafter.

5.1 Computational Details

We have investigated the vibrational and electronic properties of MEH-PPV oligomer using several modern density functionals. In addition to the ground state (charge=0, spin=0) denoted as S_0, we considered four electronic excitations, namely, first singlet excited state S_1 (charge=0, spin=0), first triplet excited state T_1 (charge=0, spin=1), and positive P^+ (charge=+1, spin=1/2) and negative P^- (charge=-1, spin=1/2) polarons. Cationic P^+ and anionic P^- species correspond to the presence of a hole and an electron on the chain, respectively. Fully relaxed geometries of all five states (S_0, S_1, T_1, P^+ and P^-) have been obtained using five different DFT functionals without imposing any symmetry constraints. In particular, we use DFT models ranging from pure GGA to long range corrected hybrids, namely, PBE[148] (a=0), B3LYP[130] (a=20), BHandHLYP[130] (a=50), CAM-B3LYP[135] (a=20-65) and LC-wPBE (a=0-100)[149], where parameter *a* is the fraction of Hartree-Fock (HF) exchange in the exchange-correlation (XC) functional (Equation 2.17). To explore the effects of polymer's highly polarizable dielectric environment, we use the conductor-like polarizable continuum model (CPCM) and a moderately polar solvent, acetonitrile (ε=37.5) as implemented in Gaussian 09 software package.[130] Optimal geometries of S_0, T_1, P^+ and P^- states have been obtained using standard self-consistent force (SCF) scheme, whereas S_1 has been calculated using TD-DFT methodology. All the computations were performed using Gaussian09 suite[130] and the 6-31G* basis set. As expected,

we found negligible effects of the dielectric environment on the properties of neutral states S_0, S_1, and T_1 and hereafter we will discuss only gas-phase calculations of these excitations.

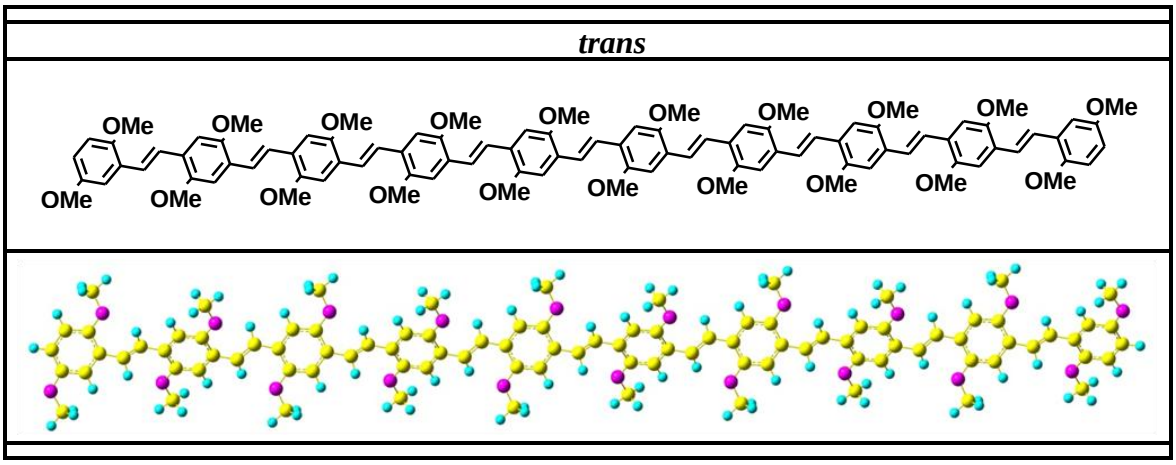

Figure 5.1: The panels display MEH-PPV oligomer in trans-isomeric form consisting of ten repeat units.

5.2 Orbital Analysis for Electronic Excitations

The panels in Figure 5.1 depicts the ten repeat units of MEH-PPV oligomer in its trans-isomeric geometrical form (alternate up and down dihedrals along the backbone of the chain). Each repeat unit consists of a phenyl ring attached to a vinylene linkage. The last two repeat units share the vinyl bridge. In our model the side chain groups OC_8H_{17} in MEH-PPV have been replaced by OCH_3 to speed up the quantum calculations. The top panels in Figure 5.2 show characteristic natural transition orbitals (NTOs) for the hole and electron of the photo-excited S_1 excitons. The NTO analysis allows for orbital representation of the electronic transition density matrix.[150] Figure 5.3 represents selected atomic spin density distributions for T_1, P^+ and P^- species. NTOs and spin distributions are calculated using two DFT models; one with low fraction of HF exchange (B3LYP) and the other one with full HF exchange at long range (LC-wPBE). The orbital and spin distributions clearly emphasize the localization of electronic

excitations at their fully relaxed geometries in the middle of the chain with the higher fraction of orbital exchange in DFT functionals. Inclusion of the dielectric environment also tends to increase the localization of the charged excitations (P^+ and P^-). These observations will be explained in much greater detail in the following sections.

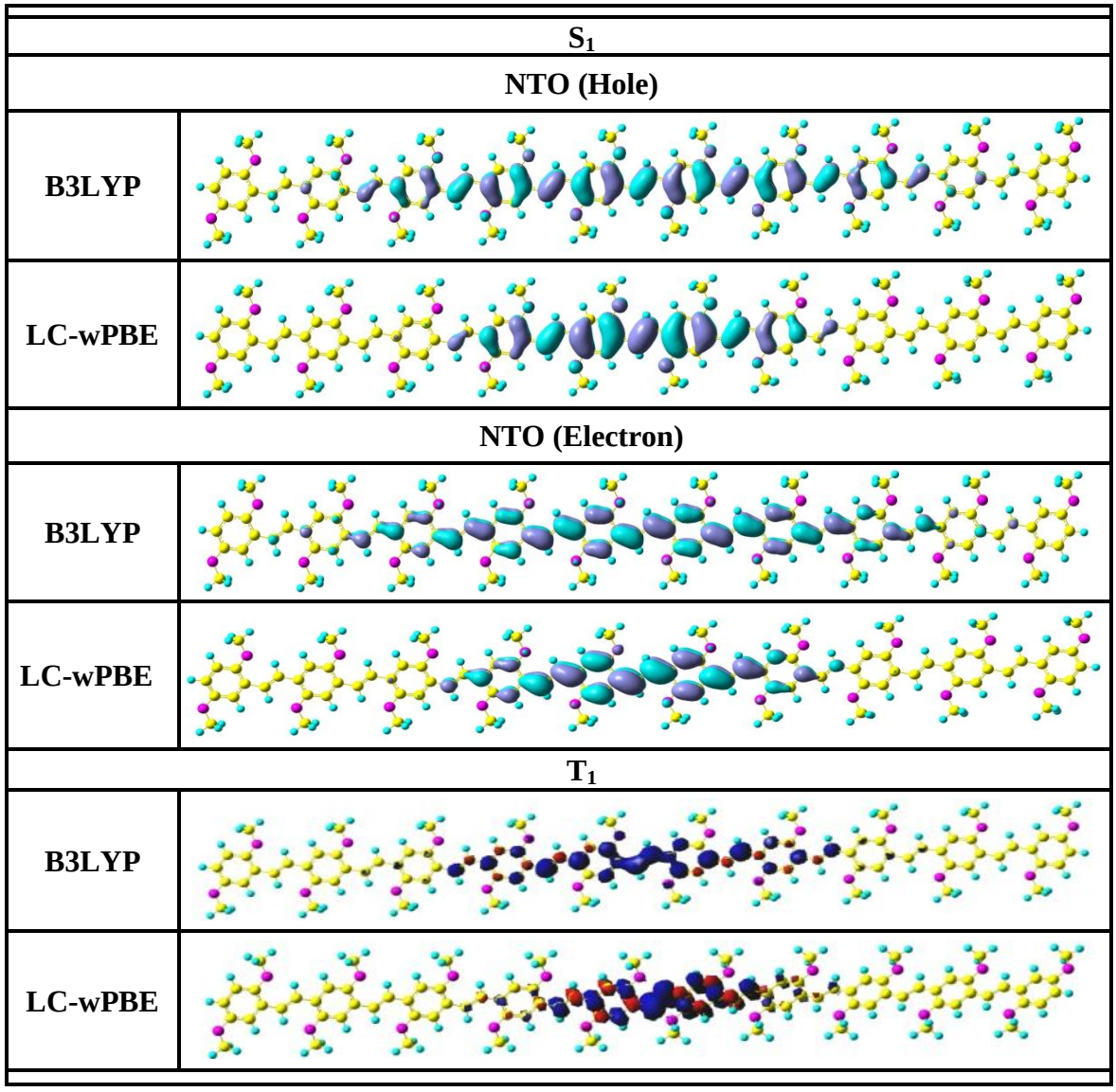

Figure 5.2: Orbital plots show natural transition orbitals (NTOs) and Mulliken atomic spin density distribution calculated at B3LYP/6-31G* and LC-wPBE/6-31G* optimized levels. The NTOs are obtained for hole and electron for the first singlet excited state (S_1), while the spin density for the first triplet excited state (T_1).

P^+	
Vacuum	
B3LYP	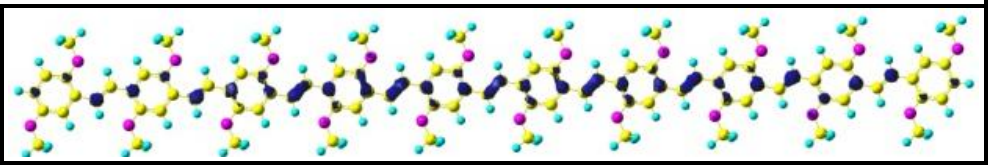
LC-wPBE	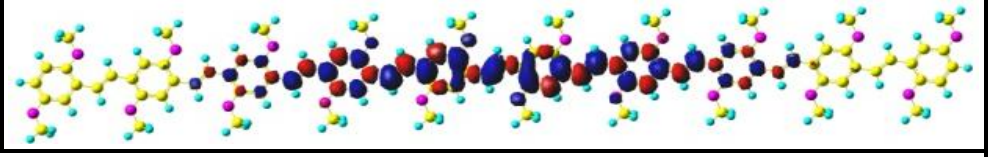
Solvent	
B3LYP	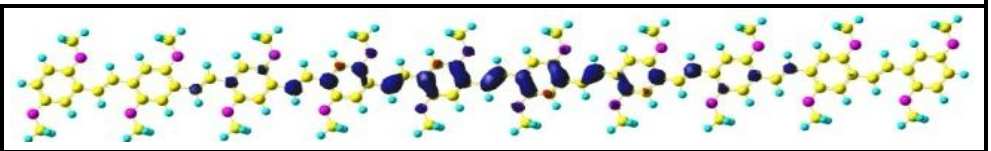
LC-wPBE	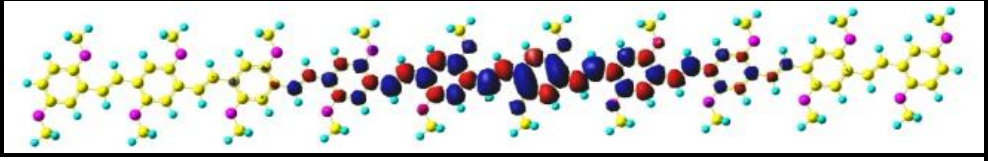
P^-	
Vacuum	
B3LYP	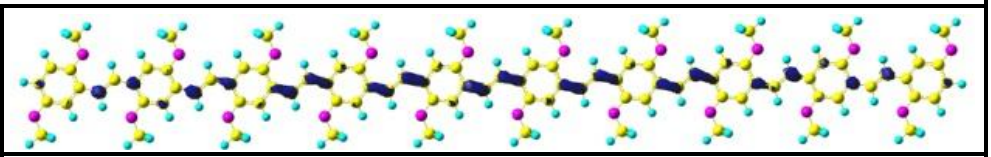
LC-wPBE	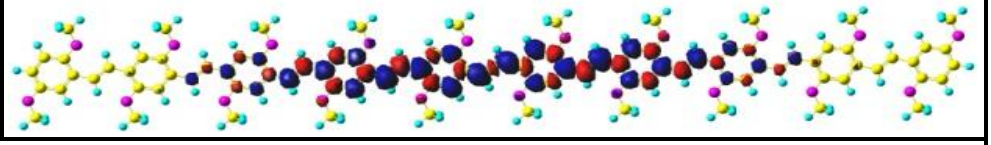
Solvent	
B3LYP	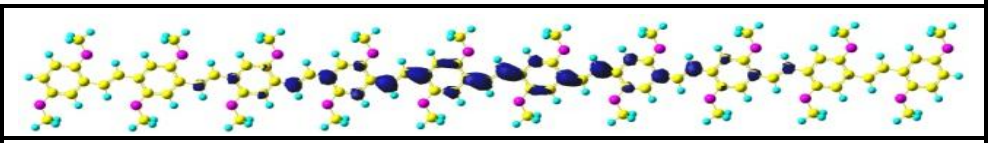
LC-wPBE	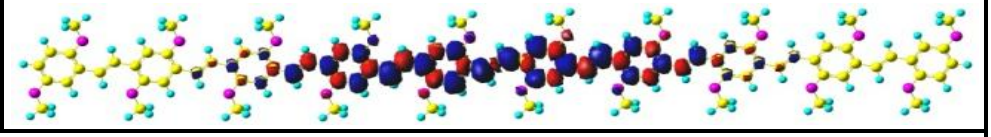

Figure 5.3: Orbital plots show Mulliken atomic spin density distribution for positive polaronic (P^+) and negative polaronic (P^-) species calculated at B3LYP/6-31G* and LC-wPBE/6-31G* optimized levels.

5.3 Two Distinct Origins of Localization

Neutral excitations and the injection of an excess charge or spin into organic polymers relax the lattice geometry and electronic orbitals over the limited section of the π-conjugated chain due to their strong electron-phonon coupling. To quantify this phenomenon, we use one geometric parameter, namely, the bond length alternation (BLA) defined as the difference between carbon-carbon single and double bond lengths in the vinyl linkage along the backbone of the polymer. BLA is a useful parameter in predicting the degree of localization of distortion in conjugated molecular chains.[79] Charge or spin density distributions are other helpful tools to estimate the spatial extent of the excitation.

5.3.1 Localization due to Vibrational Dynamics

5.3.1.1 Influence of Orbital Exchange on Localization

Figure 5.4 shows the calculated BLA along the chain for all states in question (S_0, S_1, T_1, P^+ and P^-). For neutral S_0 geometry, we observe an overall increase in the BLA corresponding to the increase in the fraction of HF exchange uniform over all the repeat units, which promotes Peierls dimerization in the π-electron systems. The BHandHLYP with 50% exchange is close to the CAM-B3LYP (20-65%). LC-wPBE (0-100%) exhibits the highest overall BLA compared to other XC functionals considered. For S_1 excitation, we find an explicit correlation between the degree of localization and the percent of HF component in the functionals. The rings at either end of the polymer chains are not perturbed with this exciton; their BLA is almost identical to the one found in the corresponding neutral polymer at its S_0 state optimized at the same level of theory. As we proceed to the middle of the chain from both the ends, the C-C bond length of the

vinylene linkage keeps decreasing (intermediate to C-C and C=C) whereas the C=C bond length keeps increasing, and the BLA reaches its minimum exactly at the middle of the chain signifying the self-trapping of the exciton[79]. Pure GGA functional PBE fails to exhibit the spatial confinement of the wavefunction. A small fraction (20%) of the HF exchange starts to localize the excitation. However, BHandHLYP, CAM-B3LYP and LC-wPBE exhibit clear structural localization; the sizes of the self-trapped excitation ranging from three to four repeat units. This is in agreement with a joint experimental and theoretical study,[147] in which the lattice deformations for S_1 states are reported to extend over a length of about 20Å (between three to four repeat units). The T_1 states are much more spatially localized compared to S_1 excitations. This is also observed in Karabunarliev *et al*. study[87] and argued due to the absence of repulsive spin-exchange between the electron and hole. Localization in B3LYP geometry is much more pronounced than that for S_1. However, BHandHLYP, CAM-B3LYP and LC-wPBE optimized structures lead to an inverted BLA (C-C bond being shorter than C=C bond in the center) resulting in much more localized T_1 state compared to B3LYP data. Here T_1 is found to be spatially confined between one to two repeat units in the middle of the chain.

For the P^+ state, like for neutral excitations, we find an enhancement in the phonon induced self-trapping with increasing orbital exchange fraction. Although, BHandHLYP and CAM-B3LYP exhibit the structural localization, still these models are inefficient in reproducing the experimentally observed polaron size.[146] However, PBE and B3LYP completely fail to predict the polaron formation. Long-range-corrected, LC-wPBE has the sharpest minimum at the middle of the chain and extends over two to three repeat units in accordance with experimental observations.[146]

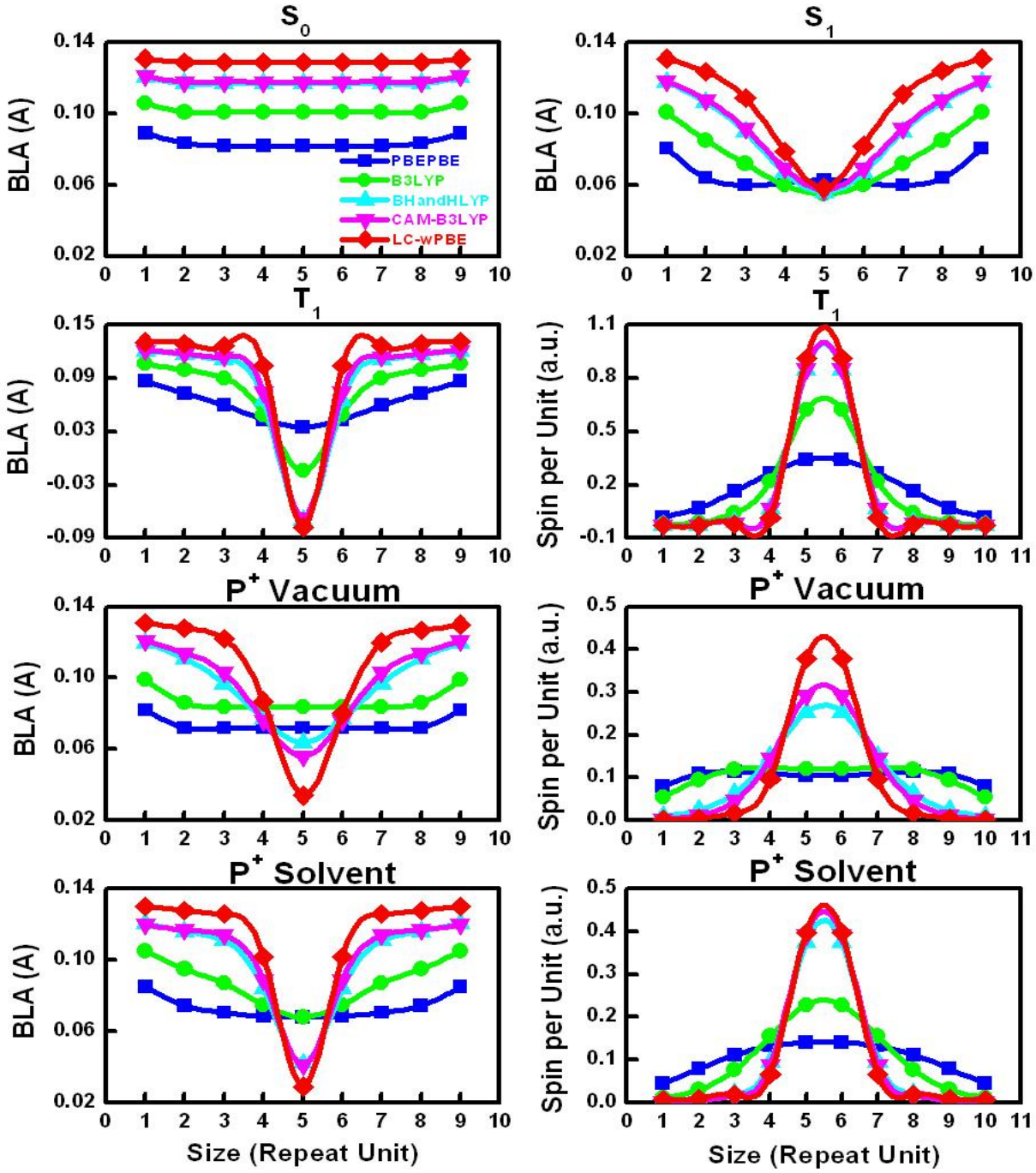

Figure 5.4: Bond length alternation (BLA) (Å) of vinylene units (left) and Mulliken atomic spin densities (a.u.) per repeat unit (right) of MEH-PPV oligomer computed using PBE, B3LYP, BHandHLYP, CAM-B3LYP, LC-wPBE functional models and 6-31G* basis set. Geometry optimization is carried out for five different electronic states, ground state (S_0), the first singlet excited state (S_1), the first triplet excited state (T_1), positive polaron (P^+) and negative polaron (P^-).

Hence, it is evident that the application of asymptotically corrected hybrid DFT functionals is critical in order to predict the polaron formation. Surprisingly, P^+ state is less localized than T_1 state. P^+ and P^- excitations display very similar trends (P^- is not shown in Figure 5.4). Thus, we can state that particle-hole symmetry is preserved in trans-isomeric form of the polymer. However, we have noticed the differences for P^+ and P^- excitations after introduction of certain defects in the chain (explained in Chapter 7), which is consistent with experimental observation[68] indicating the difference in the P^+ and P^- polaron sizes.

5.3.1.2 Influence of Polarization on Localization

We find no substantial change in the BLA of neutral S_0 oligomer and neutral S_1 and T_1 excitations by the inclusion of polarizable medium through solvent calculations as compared to the corresponding gas phase results. This is consistent with earlier DFT studies on the effect of polarization function on large systems with relatively long and easily polarizable π-bridges.[77, 151] However, as shown in Figure 5.3, polar solvent tends to increase the geometric distortion for all the XC functionals used whether pure GGA, hybrid or long range corrected in comparison to vacuum for charged excitations (P^+ and P^-). One of the major observations here is that the polarization of the medium has an effect on the polymer properties, similar to adding long range corrections to hybrid DFT. It is clearly evident from the BLA pattern of P^+ excitation that a small fraction of HF exchange (20%) in the XC functional, which was unable to predict the structural distortion in the absence of polarizing medium, begins to exhibit the localization properties in its presence. BHandHLYP and CAM-B3LYP manifest significant changes with respect to geometry localization in the presence of the solvent compared to their corresponding gas phase geometries. It is interesting to note that, BHandHLYP results are almost similar to CAM- B3LYP and very

close to LC-wPBE. In the dielectric medium, LC-wPBE is able to predict the polaron sizes correctly in accordance with experiment extending around two repeat units. This implies that inclusion of polarizable dielectric medium has a greater effect on the spatial confinement of the polaronic wavefunctions, in addition to long-range-corrections to DFT functionals. The BLA patterns for P^- states in the presence of solvent are same as those of P^+.

5.3.2 Localization due to Energy Stabilization

We also examine the Mulliken atomic spin densities (difference in the spin of electrons in alpha and beta molecular orbitals) integrated over each repeat unit for T_1, P^+ and P^- excitations. These quantities shown in Figure 5.4 are complementary to BLA and show similar order of localization in both gas phase and solvent. Comparison of these two quantities, BLA signifying localization via geometric distortion and spin density distribution probing localization of the electronic density, allows distinguishing between two distinct origins leading to localization of electronic excitations: spatial localization of the state wavefunction by itself on the undistorted geometry and localization of the wavefunction assured by distortion of the structure during geometry relaxation. We found (not shown here) that neutral excitations S_1 and T_1 localize primarily due to geometric distortion (depicted in the BLA functional form in Figure 5.4). In contrast, charged species P^+ and P^- mainly localize due to electronic reasons. This is in agreement with the observations elucidated in Geskin *et al.*[93] about the emphasis on the choice of the method for electronic-structure calculations rather than geometrical optimization for charged species. This suggests that, for charged excitations, localization is principally produced by the electronic rearrangements and the character of the functional rather than the structural

distortions, however, the opposite seems to be the case for neutral excitons. A detailed analysis of these phenomena will be presented in Chapter 6.

5.4 Conclusions

We summarize the localization properties predicted by different DFT functionals in terms of the characteristic size of the electronic excitations under study in Figure 5.5.

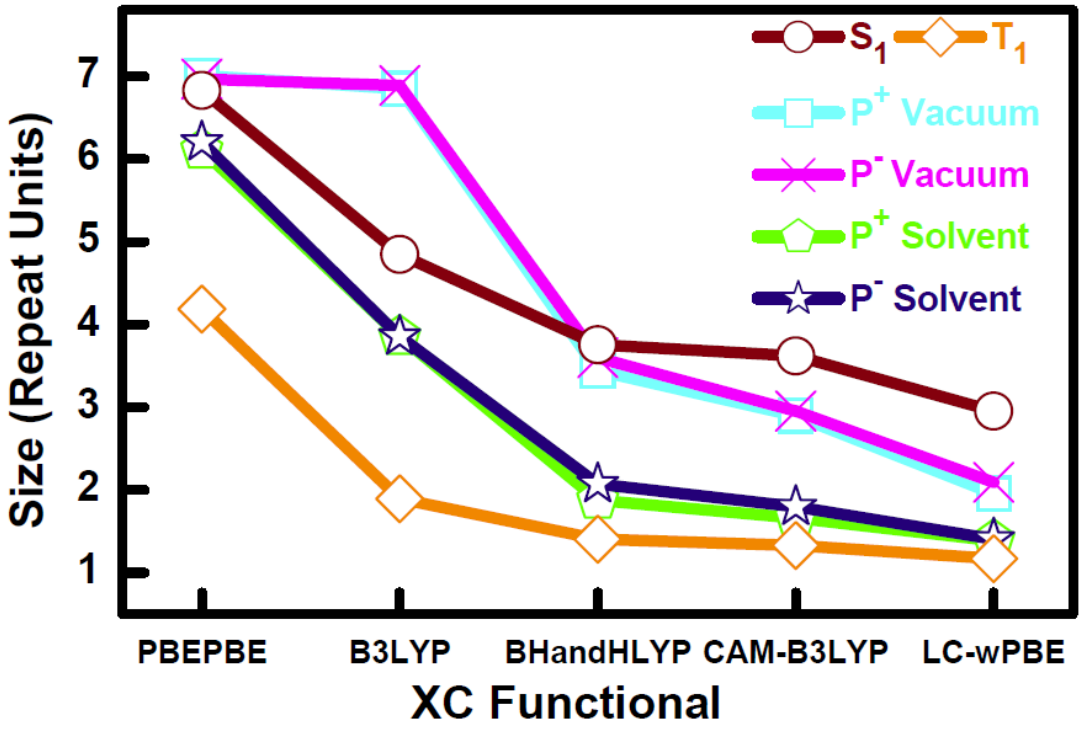

Figure 5.5: Characteristic size of the electronic excitations defined as full width at half maximum (in terms of repeat units) of the BLA extent in MEH-PPV oligomer calculated for S_1, T_1, P^+ and P^- states from Figure 5.4 data.

This size is defined as the full width at half maximum (FWHM) in terms of repeat units of the optimized carbon-carbon BLA of vinylene bridges of the polymer chain. For P^+ and P^- states in solvent, LC-wPBE, CAM-B3LYP and BHandHLYP predict the localization in agreement with experimental findings[146]. Particle-hole symmetry is clearly evident from this figure. The S_1 states

of neutral oligomers are spatially less localized compared to polaronic wavefunctions, whereas T_1 excitations are more localized than them.

Poly-phenylene-vinylene based materials are of substantial theoretical interest for the extensive available experimental data[64, 152-154] and significant technological promises. We investigated theoretically the five electronic states (S_0, S_1, T_1, P^+ and P^-) in MEH-PPV oligomer playing the major role in the charge- and energy- transfer dynamics in the bulk polymeric materials. It has been established that the long-range corrections to the XC functional are crucial in order to predict the spatial localization of all electronic excitations considered. Inclusion of dielectric medium effects is also shown to be important for the polaron formation. LC-wPBE (0-100%) predicts the polaron localization in both vacuum and solvent agreeing with experimental data for charged polymers, whereas BHandHLYP (50%) and CAM-B3LYP (20-65%) produce significant localization only in the presence of a polarizable solvent.

CHAPTER 6 ROLE OF GEOMETRIC DISTORTION AND POLARIZATION IN LOCALIZATION OF ELECTRONIC EXCITATIONS

In Chapter 5, we have studied five different density functional theory (DFT) models ranging from pure GGA to long-range-corrected hybrid functionals) to study the nature of the self-trapped electronic excitations in oligo (phenylene vinylenes). The polaron formation (spatial localization of excitations) is observed only with the use of range-corrected hybrid DFT models including long-range electronic exchange interactions. We have spoken about the two distinct origins leading to self-localization of electronic excitations in these low-dimensional semiconducting polymers. First of all, distortion of molecular geometry may create a spatially localized potential energy well where the state wavefunction self-traps. Secondly, even in the absence of geometric relaxation and vibrational dynamics, the electronic excitation may become spatially confined due to energy stabilization caused by polarization effects from surrounding dielectric medium. This motivated us to conduct a detailed first principle study of oligo (phenylene vinylene) derivatives aiming to separate these two fundamental sources of spatial localization. The electronic excitations in question include the lowest singlet (S_1) and triplet ($T_1^{\dagger}$) excitons, positive (P^+) and negative (P^-) polarons and the lowest triplet (T_1) states .We have analyzed the interdependence between the extent of the geometrical distortion and the localization of the orbital and spin density, and have observed that the localization of P^+ and P^- charged species are quite sensitive to solvent polarization effects and the character of the DFT functional used, rather than the structural deformations. In contrast, the localization of neutral states, S_1 and $T_1^{\dagger}$, is found to follow the structural distortions. Notably, T_1 excitation obtained with the mean field SCF approach is always strongly localized in range-corrected hybrid DFT models. The molecular orbital energetics of these excitations was further investigated to identify

the relationships between state localization and the corresponding orbital structure. A characteristic stabilization (destabilization) of occupied (virtual) orbitals is observed in hybrid DFT models, compared to tight-binding model-like orbital filling in semi-local GGA functionals. The molecular and natural orbital representation allows visualization of the spatial extent of the underlying electronic states. In terms of stabilization energies, neutral excitons have higher binding energies compared to charged excitations. In contrast, the polaronic species exhibit the highest solvation energies amongst all electronic states studied. These studies are important for understanding excited-state dynamics and charge-transfer properties of excitons and polarons in polymeric materials.

6.1 Computational Details

We study the ground state S_0 (charge=0, spin=0), positive polaron P^+ (charge=+1, spin=1/2), negative polaron P^- (charge=-1, spin=1/2), first triplet T_1 (charge=0, spin=1), first singlet S_1 (charge=0, spin=0) and first triplet $T_1^\dagger$ (charge=0, spin=1) excited states for a ten-repeat-unit MEH-PPV oligomer in its trans-isomeric geometrical form unless otherwise mentioned. In our model, the side-chain groups OC_8H_{17} in MEH-PPV have been replaced by OCH_3 to speed up the quantum calculations. Every repeat unit consists of a phenyl ring attached to a vinyl linkage. The two terminal rings share the same vinyl bridge. Cationic P^+ and anionic P^- species correspond to the presence of a hole and an electron on the chain, respectively. Optimal geometries and energetics of P^+, P^- and T_1 states are obtained using the standard self-consistent force (SCF) scheme, whereas $T_1^\dagger$ and S_1 are calculated using time dependent DFT (TD-DFT) methodology. In particular, this allows us to compare properties of the first triplet state obtained

with two different computational techniques: the variational mean-field SCF approach for a given spin state (denoted as T_1) and the TD method for calculating the triplet state (denoted as $T_1^{\dagger}$) via single-particle excitations from the reference ground state S_0.

A moderately polar solvent, acetonitrile (ε=37.5), is included in this study via the conductor-like polarizable continuum model (CPCM) as implemented in Gaussian09 software package[46] in order to mimic the polymer's highly polarizable dielectric environment. Even though this may be an overestimation of the dielectric constant of PPV,[155] the effects of this dielectric medium throughout our study are minor and the conclusions are the same as for the simulations in gas phase. All computations have been performed using Gaussian09 suite[46] and the 6-31G* basis set. Fully relaxed geometries of all the six electronic states (S_0, P^+, P^-, T_1, S_1 and $T_1^{\dagger}$) are studied at five different DFT models ranging from pure GGA to long-range-corrected hybrid functionals without imposing any symmetry constraints. These DFT functionals are comprised of different exchange-correlation (XC) functionals namely PBE[148] (a=0), B3LYP[130] (a=20), BHandHLYP[130] (a=50), CAM-B3LYP[149] (a=20-65) and LC-wPBE[149] (a=0-100), where parameter a is the fraction of Hartree-Fock (HF) exchange in the XC functional (Equation 2.17).

6.2 Interrelation between Two Distinct Origins of Localization

Comparison of bond length alternations[156] (BLAs) and electronic density distributions[72, 75] in conjugated organic polymers is useful in understanding the factors governing localization in them. On one hand, BLA predicts the degree of structural deformation and, thus, confinement of the state wavefunction arising due to the distortion during geometry relaxation. However, the

electron density distribution directly signifies spatial confinement of this wavefunction on the distorted or undistorted geometry. In order to quantify these two distinct origins of localization and to explore the interrelation between them, we calculate the electronic density at PBE and LC-wPBE levels for both uniform and distorted geometries individually. In Chapter 5, we observed that the long-range-corrected LC-wPBE exhibited clear structural and electronic localization in contrast to the pure GGA functional PBE. Long-range-corrected hybrid functionals have been shown to predict the BLAs and charge-transfer excitations in π-conjugated materials.[157, 158] In order to investigate the effect of geometry distortion on the electronic localization we show the electronic calculations at PBE level for both PBE and LC-wPBE optimized geometries. Similarly, the LC-wPBE level of calculation for both these geometries allows us to infer the influence of the delocalized geometry on the localization of the electronic wavefunction. The Mulliken atomic spin densities (difference in the spin of electrons in alpha and beta MOs) integrated over each repeat unit for all the SCF excitations are used to measure the delocalization of the electronic state for polaronic states, and the same analysis on the natural transition orbitals[150] (NTOs) of a hole or electron yields information about the localization of excited states in neutral TD excitations. Since the hole and electron orbital wavefunctions show similar delocalization properties (in absence of charge-transfer states in these polymeric chains) the average of the two is analyzed. The spin and orbital densities for all these excitations are normalized to unity for a fair comparison.

6.2.1 Influence of Geometry on Energy Stabilization

Figure 6.1 summarizes the effect of the DFT models on the localization properties of electronic excitations by showing the distribution of the Mulliken atomic spin density (electronic

density per repeat unit) along the chain for a ten-repeat-unit MEH-PPV oligomer. In Figure 5.1 we have used a composite notation "*functional1//functional2*" that indicates, first the DFT model used for the calculation of the spin (or orbital) density, and second the functional used to obtain the geometry of the molecule. Previously we found[159] that semi-local PBE and range-corrected LC-wPBE functional result in 'uniform' and 'distorted' optimal geometries, respectively, corresponding to delocalized and localized excitation. Here we observe that the P^+ polaron spin density calculated using the PBE (LC-wPBE) model in vacuum remains delocalized (localized) irrespective of what geometry one uses. Consequently, the localization of the P^+ charged state is driven by the character of the functional rather than by structural distortions. Compared to an isolated molecule, the localization of the P^+ excitation increases when polarizable dielectric medium effects are included in the calculations. The P^- excitation behaves very much as P^+. Thus, particle-hole symmetry is conserved in a uniform all-trans MEH-PPV oligomer approach and the LC-wPBE model always localizes this excitation. However, the geometry distortion at the LC-wPBE optimal geometry for T_1 state is local and strong (the respective BLA becomes negative) as discussed in Chapter 5. As a result, the T_1 state becomes localized even at the PBE level when the LC-wPBE optimal geometry is used. Triplet state localization calculated with TD-DFT approach shows the same trend as the calculation at the mean-field SCF level. Notably, localization properties of the first excited state S_1 calculated using TD-DFT seem to be similar to those of the P^+ state (except slightly larger size). However, this conclusion is not justified since in this case the end effects appear and calculations of larger oligomers are necessary (see discussion below). The calculations for neutral T_1, $T_1^{\dagger}$ and S_1 excitations in a dielectric medium are not shown in Figure 6.1 as they offer no substantial effect on their localization properties.

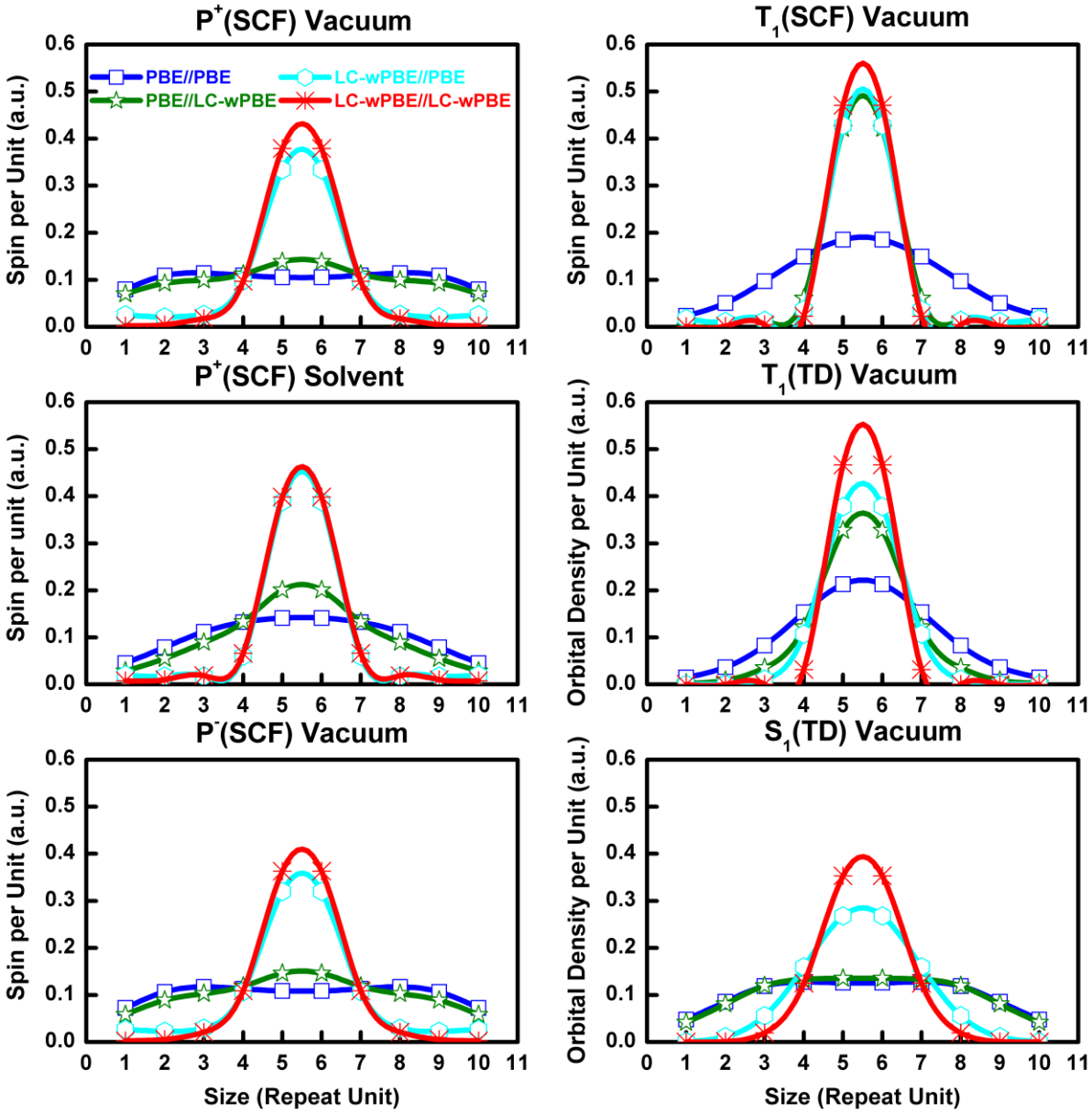

Figure 6.1: Electronic density per repeat unit (a.u.) of MEH-PPV oligomer consisting of 10 repeat units computed at PBE//PBE, PBE//LC-wPBE, LC-wPBE//PBE and LC-wPBE//LC-wPBE levels using 6-31G* basis set.

The calculations are obtained for five electronic states: positive (P^+) and negative (P^-) polarons, the first triplet (T_1) excited state obtained using the SCF scheme, and the first triplet ($T_1^\dagger$) and singlet (S_1) excitons calculated using TD-DFT methodology. Plotted are the Mulliken atomic spin densities (spin per unit) integrated over each repeat unit for P^+, P^- and T_1 states, and the average population densities of the NTOs for the hole and electron (orbital density per unit) for $T_1^\dagger$ and S_1 excitations. The spin and orbital densities are normalized to unit for fare comparison and are calculated using the first functional in the legend in their corresponding fully relaxed geometries optimized with the second functional.

Figure 6.2 explores the effect of the geometry relaxation on the localization of the state wavefunction calculated for the ten-repeat-unit MEH-PPV oligomer. Plotted are spin (for SCF calculations) and orbital (for TD-DFT calculations) electronic densities for all excitations (T_1, P^+, P^-, $T_1^\dagger$ and S_1) in the ground state S_0 'uniform' geometry (top row) and in their corresponding native optimal 'distorted' geometries (bottom panel) as calculated at LC-wPBE level. In vacuum, we observe that T_1 is much more localized than P^+ and P^- - a more quantitative measure of localization/delocalization is given in Figure 6.3. The P^+ localization is similar to that of P^-. The $T_1^\dagger$ state computed with TD-DFT is much more localized compared to T_1. This difference in results between SCF and TD-DFT calculations is discussed below. The S_1 state exhibits the least tendency to localize among them all. Further addition of a polarizable medium (solvent) into the calculation localizes the charged (P^+ and P^-) species but has no effect on the neutral (T_1, $T_1^\dagger$, S_1) states. The bottom panels in Figure 6.2 display the electronic localization of the excitations under study in their corresponding relaxed native geometries. Comparing top and bottom panels we see that the geometry relaxation has no influence on the T_1, P^+ and P^- excitations since they are already strongly localized at the undistorted S_0 geometry. However, the $T_1^\dagger$ and S_1 states calculated with TD-DFT are found to be much more localized in their corresponding native geometries than in the S_0 state: the S_1 state being nearly as localized as P^+ and P^-, whereas $T_1^\dagger$ localization coincides with that of T_1. This indicates a significant localization effect associated with geometry distortion for the neutral $T_1^\dagger$ and S_1 excitations within the TD-DFT framework. Given strong localization of all states, the solvent effects are minimal in their corresponding relaxed geometries (Figure 6.2). A figure similar to Figure 6.2 calculated at the BHandHLYP level are shown in Figure 6.S1 and it emphasizes the generality of our observations.

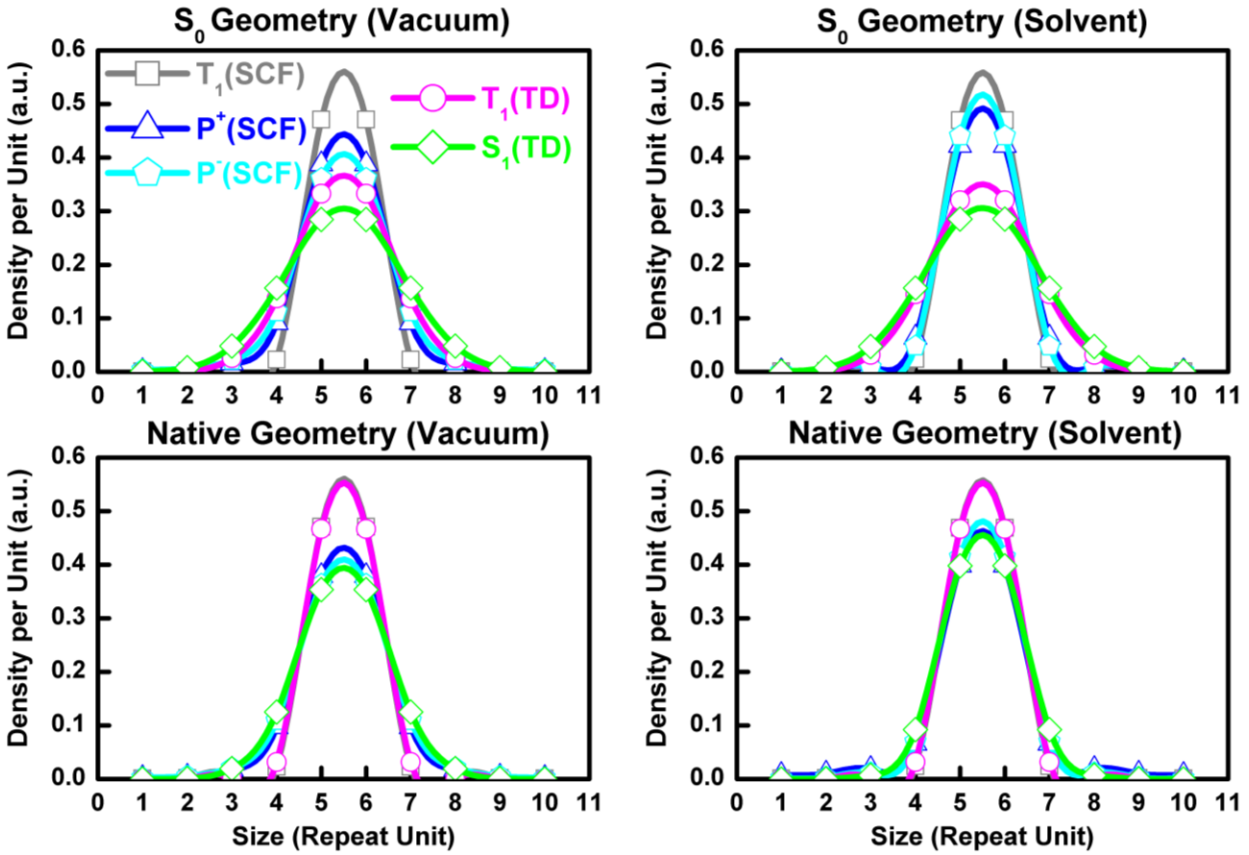

Figure 6.2: Electronic density per repeat unit (a.u.) of the MEH-PPV oligomer consisting of 10 repeat units for all the excitations in ground state (S_0) geometry (top panel) and their corresponding native geometries (bottom panel) calculated at LC-wPBE/6-31G* level.

6.2.2 Influence of Chain Length on Energy Stabilization

The localization properties predicted by the LC-wPBE functional in terms of the characteristic size of the electronic excitations for S_0 and corresponding native geometries in vacuum and solvent are summarized in Figure 6.3 for ten and twenty repeat units of the MEH-PPV oligomer. This size is defined as the full width at half-maximum (fwhm) in terms of the repeat units of the electronic density plots of the polymer chain. The triplet state T_1 exhibits the highest localization for all states considered in Figure 6.3 being insensitive to the chain length, solvent and geometric distortion.

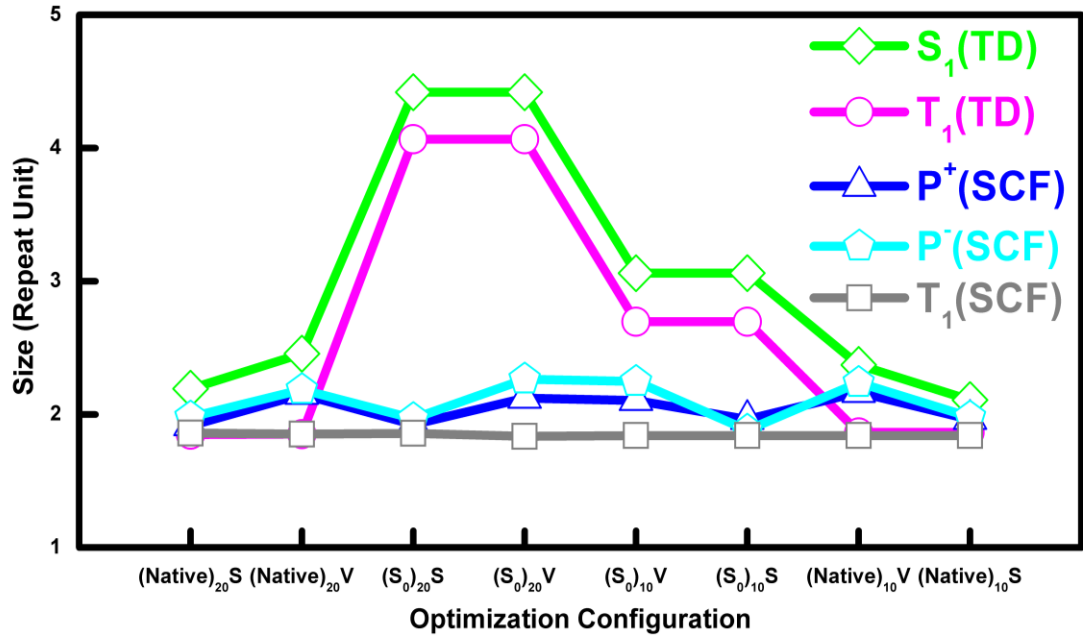

Figure 6.3: Characteristic size of calculated electronic excitations (S_1, $T_1^{\dagger}$, P^+, P^- and T_1) defined as the full width at half-maximum (fwhm) in terms of the repeat units in MEH-PPV oligomers of different lengths calculated at LC-wPBE level.
The X-axis label of this figure describes the geometry in a common bracket with the number of repeat units of the polymer as a subscript, and the medium (V and S stand for vacuum and solvent, respectively).

Polarization of the medium plays an important role in the localization of charged (P^+ and P^-) species, while distortions of geometry have smaller effects. Figure 6.3 clearly evidences that the singlet state S_1 is more delocalized than triplet state T_1 for all cases as one would expect due to the Pauli repulsion of the two electrons occupying the same orbital. It is also observed in Karabunarliev *et al.*'s[87] study and argued due to the absence of repulsive spin-exchange between the electron and hole. As expected, the localization sizes do not depend on the oligomer length for all calculation of T_1, P^+ and P^- excitations performed at the mean-field SCF level. However, the situation is different for TD-DFT calculations of $T_1^{\dagger}$ and S_1 states. We observe a strong increase of $T_1^{\dagger}$ size at the uniform ground state S_0 geometry when doubling the size of the oligomer from ten to twenty repeat units, which is drastically different from the SCF results for

T_1 state. This difference can be attributed to the fact that, for a uniform geometry, TD-DFT builds the excited state wavefunction by an equal weight superposition of the single-particle excitations from the ground state along the chain (i.e. the delocalization of $T_1^{\dagger}$ state would monotonically grow with the chain length).[73, 160] In contrast, the mean-field construct automatically limits the spatial extent of a spin to fewer than two repeat units. However, it is important that geometry distortion is local and strongly localized triplet state at TD-DFT level. Namely, triplets T_1 and $T_1^{\dagger}$ do show the same extent of localization in their corresponding native geometries, demonstrating consistency between SCF and TD-DFT modeling. Calculations of the first singlet excitation S_1 with the TD-DFT approach show trends similar to $T_1^{\dagger}$ modeling. Notably, the dielectric medium slightly increases S_1 localization for native geometry (exciton self-trapping).

6.3 Effect of Orbital Exchange and Polarization on Kohn-Sham Density

We further examine the density of single-particle states (Kohn-Sham orbitals) for all SCF calculations (S_0, T_1, P^+ and P^-) in their corresponding native geometries calculated at PBE, B3LYP, BHandHLYP, CAM-B3LYP and LC-wPBE levels in Figure 6.4. Calculation of ground state S_0 shows a typical HOMO-LUMO gap between occupied and valance space growing with an increase of the orbital exchange in the functional model. In the semi-local PBE framework, all excitations (T_1, P^+ and P^-) are formed by filling/emptying the respective orbitals with minimal change to the relative orbital energetics. For example, the T_1 state is made by promoting an electron from the α highest occupied molecular orbital (HOMO) to β lowest unoccupied molecular orbital (LUMO).

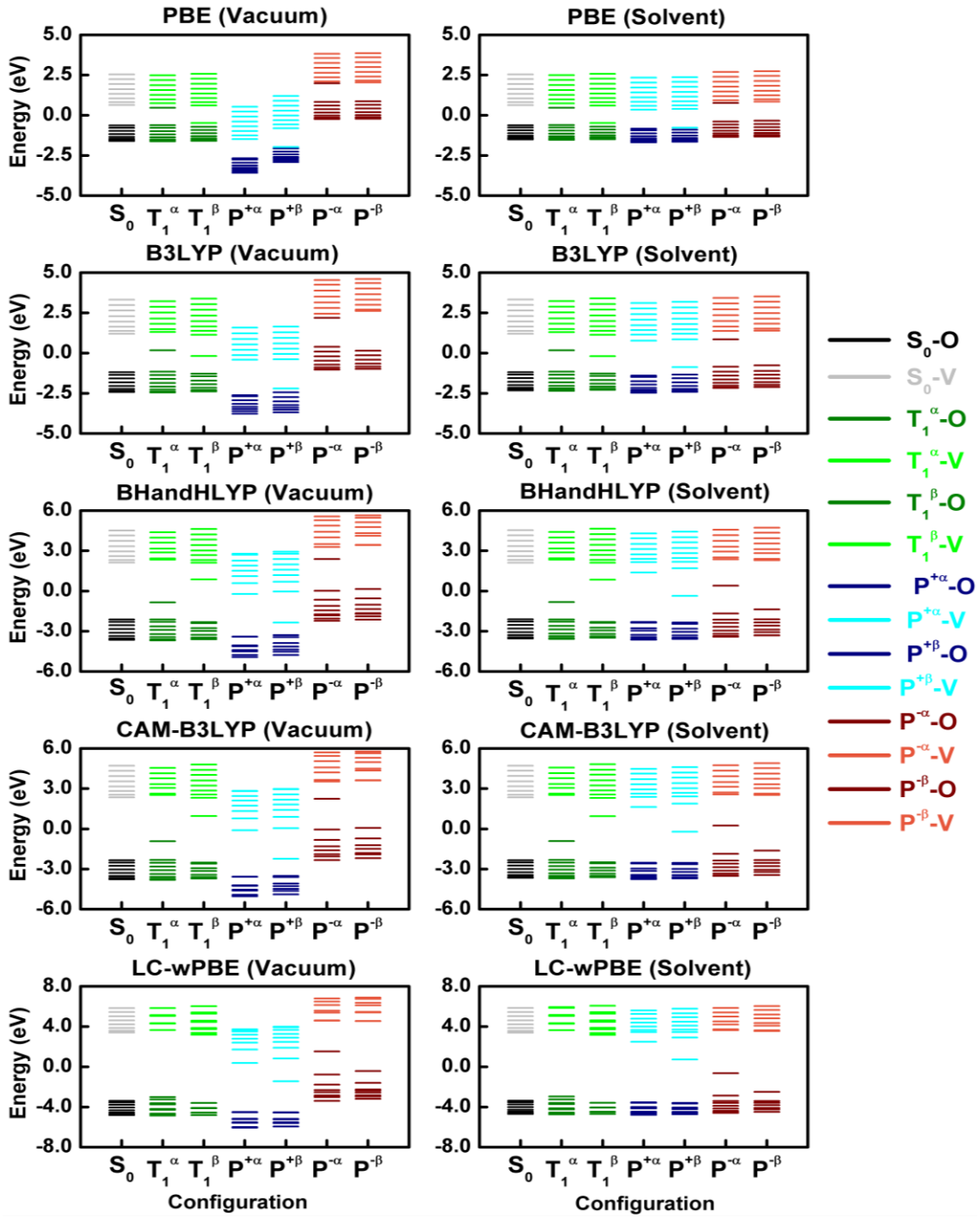

Figure 6.4: Density of Kohn-Sham states of MEH-PPV oligomer comprised of 10 repeat units computed using various functional models with 6-31G* basis set for S_0, T_1, P^+ and P^- states calculated using the SCF.

The α and β molecular orbitals MOs of each spin states are shown separately (represented by the same color). The darker (lighter) shades in the figure correspond to the occupied (O) and virtual (V) orbitals, respectively.

Thus, pure/semi-local DFT behaves as a typical tight-binding model with no electronic orbital relaxation effects. Calculation of charged species P^+ (P^-) in vacuum lead to stabilization (destabilization) of the entire orbital manifolds as evidenced by shifts down (up) in Figure 6.4 (left column). Notably, calculations of P^+ and P^- in the solvent environment strictly align their HOMO-LUMO gaps with the respective neutral species S_0 and T_1 (Figure 6.4, right column). In addition, the solvent leads to a slight increase in the band gap for the charged (P^+ and P^-) excitations as compared to their respective counterparts in the vacuum. This is consistent with earlier DFT results on the effect of polarization functions on large systems with π-conjugation.[137, 151] Adding a fractional amount of HF orbital exchange into the DFT functional results in a well-pronounced electronic orbital relaxation, i.e. the singly occupied state shifts down toward occupied manifold whereas the singly unoccupied state moves up toward valence manifold. The solvent enhances this stabilization. Consequently, for a range-corrected LC-wPBE model (with 100% of asymptotic exchange) calculations of T_1 in solvent, (n+1) α and (n-1) β occupied orbitals become well aligned well separated from the respective virtual orbitals. Calculations at the same level of the charged state P^+ (P^-) lead to the appearance of a single unoccupied (occupied) state located close to the mid-gap. This is a typical picture of polaron energetics emerging from solid-state models.[86, 161, 162] Optical transitions emerging after creating charge carriers are attributed to such states and have been extensively explored via ultrafast pump-probe spectroscopy. [95, 163, 164]

6.4 Effect of Geometry Relaxation on Kohn-Sham Density

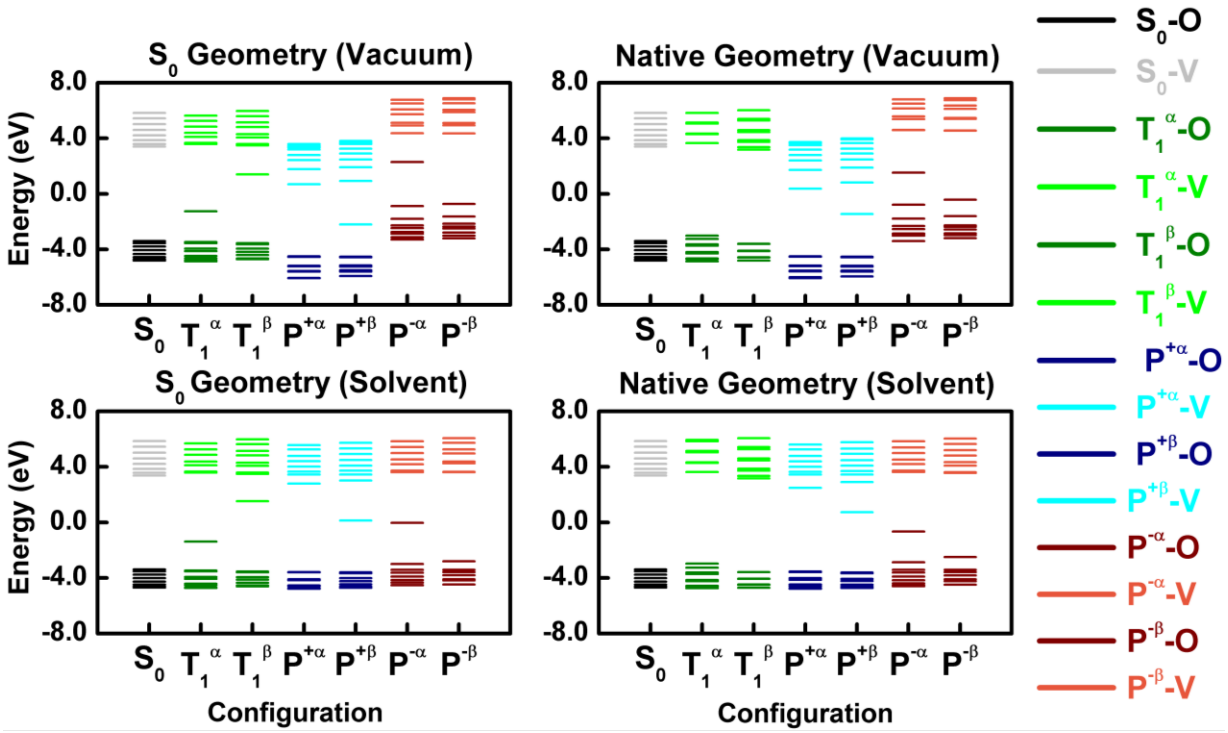

Figure 6.5: Density of Kohn-Sham states for S_0, P^+, P^- and T_1 states of the MEH-PPV oligomer comprised of 10 repeat units computed at LC-wPBE/6-31G* level for S_0 state geometry (left panel) and their corresponding native optimal geometries (right panel).

Figure 6.5 elucidates the effects of geometry relaxation on the energy band picture for these (S_0, T_1, P^+ and P^-) states calculated at LC-wPBE level. As shown in Chapter 5, compared to the S_0 uniform geometry, the BLA parameter calculated with LC-wPBE functional is locally reduced in the middle of the molecule at the respective native optimal geometry evidencing excitation self-trapping. This distortion increases from the S_1 state to charged P^+ and P^- species, and to even inverted (negative) BLA for the T_1 excitation. Such strong geometry distortion for the T_1 state manifests itself by a visible orbital relaxation of the mid-gap singly occupied α and empty β levels in S_0 geometry toward the respective occupied and virtual manifolds at the native geometry. In contrast, positions of Kohn-Sham (KS) orbitals are not significantly affected by

geometry relaxation for charged states P^+ and P^-. Compared to vacuum, the solvent environment aligns the band-gaps of charged excitations with the neutral ones and further facilitates the orbital relaxation. Figure 6.S2 displays similar plots obtained for the other three functionals, PBE, B3LYP and CAM-B3LYP (only vacuum calculations are shown), illustrating a monotonic reduction of the orbital relaxation with decrease of the orbital exchange fraction in the DFT kernel.

6.5 Effect of Orbital Exchange and Polarization on Orbital Energetics

Table 6.1: Binding energies of 10 repeat units of MEH-PPV oligomer for all the SCF (T_1, P^+ and P^-) and TD-DFT (S_1 and $T_1^\dagger$) excitations under study at five different XC functionals namely PBE, B3LYP, BHandHLYP, CAM-B3LYP and LC-wPBE both in vacuum (V) and solvent (S).

Binding Energy [E(S_0,X)-E(X,X)] (eV)										
Excitation (X)	**T_1**		**P^+**		**P^-**		**S_1**		**$T_1^\dagger$**	
	V	**S**	**V**	**S**	**V**	**S**	**V**	**S**	**V**	**S**
PBE	0.10	0.10	0.03	0.03	0.04	0.04	0.06	0.06	0.10	0.10
B3LYP	0.30	0.29	0.05	0.06	0.06	0.07	0.13	0.14	0.20	0.20
BHandHLYP	0.67	0.66	0.11	0.18	0.11	0.19	0.18	0.19	*1.39*	*1.38*
CAM-B3LYP	0.63	0.62	0.14	0.17	0.14	0.19	0.17	0.17	*1.31*	*1.29*
LC-wPBE	1.01	0.99	0.29	0.26	0.31	0.28	0.30	0.30	*1.81*	*1.80*

The difference between the total energy of the excitation (X) in S_0 geometry and that in its corresponding fully relaxed geometry is reported. Binding energies marked in red color in italics are not meaningful due to the negative excitation energies from the S_0 state attributed to the orbital instabilities introduced with higher HF exchange.

This analysis of the orbital energetics allows us to rationalize trends in the excitation binding energies due to geometry relaxation (Table 6.1) and solvation energies (Table 6.2). Table 6.1 summarizes the binding energies calculated for ten repeat unit MEH-PPV oligomer for all excitations (T_1, P^+, P^-, S_1 and $T_1^\dagger$) under study at various DFT levels both in vacuum and in

solvent. Binding energy is defined as the difference between the total energy of the excitation in the neutral (S_0) geometry and that in its fully relaxed configuration (denoted as X). Binding energy is an important parameter controlling the charge transport in the conjugated polymers.[73] Overall, we observe a gradual increase in the energy with the percent of HF exchange in the functionals for all excitations (Table 6.1). The semi-local PBE model with zero HF exchange produces the lowest, heavily underestimated energies amongst all,[74, 165] whereas LC-wPBE functional with full HF exchange at the long range reports the highest. The values calculated at BHandHLYP with 50% HF exchange and coulomb attenuated CAM-B3LYP are almost the same. An addition of a dielectric medium does not have a significant effect on these energies. At the LC-wPBE level, the binding energy of the T_1 state is the largest, reflecting significant electronic orbital relaxation (Figure 6.4) due to large geometry distortion. Binding energies for the P^+, P^- and S_1 excitations are about the same. Notably, binding energies for the $T_1^\dagger$ excitation calculated using TDDFT with functionals with high fraction of orbital exchange (BHandHLYP, CAM-B3LYP and LC-wPBE) become negative (marked in the italic red). This is a manifestation of the well-known triplet instability first observed in the TD-HF methodology, which also appears in TD-DFT for hybrid functionals with large amount of HF exchange, as studied in detail elsewhere.[157] These problems arise when a spin-contaminated unrestricted KS solution becomes lower in energy than the respective restricted closed-shell solution.[157]

Table 6.2 reports the solvation energies for the ten repeat unit MEH-PPV oligomer for all excitations (T_1, P^+, P^-, S_1 and $T_1^\dagger$) under study calculated at various DFT levels. This quantity is defined as the difference between the total energy of the excitation in vacuum and that in the solvent, both calculated using the S_0 geometry. Overall solvation energies are significant, varying from 1.5 to 3eV across the set. Their values gradually increase with an increase of a fraction of

orbital exchange in the functional owing to a larger solvent stabilization of more localized states. The solvation energies for the polaronic species P^+ and P^- are markedly higher than those for neutral ones (T_1, S_1 and $T_1^\dagger$) due to the orbital alignment effect shown in Figure 6.3.

Table 6.2: Solvation energies of the 10 repeat units of the MEH-PPV oligomer for all (T_1, P^+ and P^-, S_1 and $T_1^\dagger$) excitations under study at five different XC functionals namely PBE, B3LYP, BHandHLYP, CAM-B3LYP and LC-wPBE.

Solvation Energy [$E(S_0,X_V)$-$E(S_0,X_S)$] (eV)					
Excitation (X)	**T_1**	**P^+**	**P^-**	**S_1**	**$T_1^\dagger$**
PBE	1.65	1.85	2.68	1.68	1.65
B3LYP	1.57	1.82	2.64	1.61	1.56
BHandHLYP	1.66	2.10	2.95	1.71	1.63
CAM-B3LYP	1.59	2.11	2.93	1.64	1.58
LC-wPBE	1.78	2.46	3.35	1.83	1.75

The difference between the total energy of the excitation (X) in vacuum and that in the solvent is reported. Both these energies are calculated in S_0 geometry.

6.6 Orbital Analysis for Electronic Excitations

Figure 6.6 displays the characteristic HOMO and LUMO orbitals for S_0, T_1, P^+ and P^- states in their corresponding native geometries calculated using the LC-wPBE model in the presence of the solvent. For all the states but S_0, the highest energy valence state belongs to α orbitals whereas the lowest energy conduction state to the β ones. We observe the HOMO and the LUMO for S_0 to be delocalized throughout the oligomer whereas those for the T_1 state become completely localized due to a significant geometry distortion. The α HOMO of P^- represents a localized state of a negative polaron, whereas the β LUMO orbital is delocalized. The situation is reversed for P^+ excitation, where the β LUMO represents a polaronic state. A similar plot but for calculations in vacuum presented in Figure 6.S3, shows that solvent does not change the form/delocalization of the orbitals.

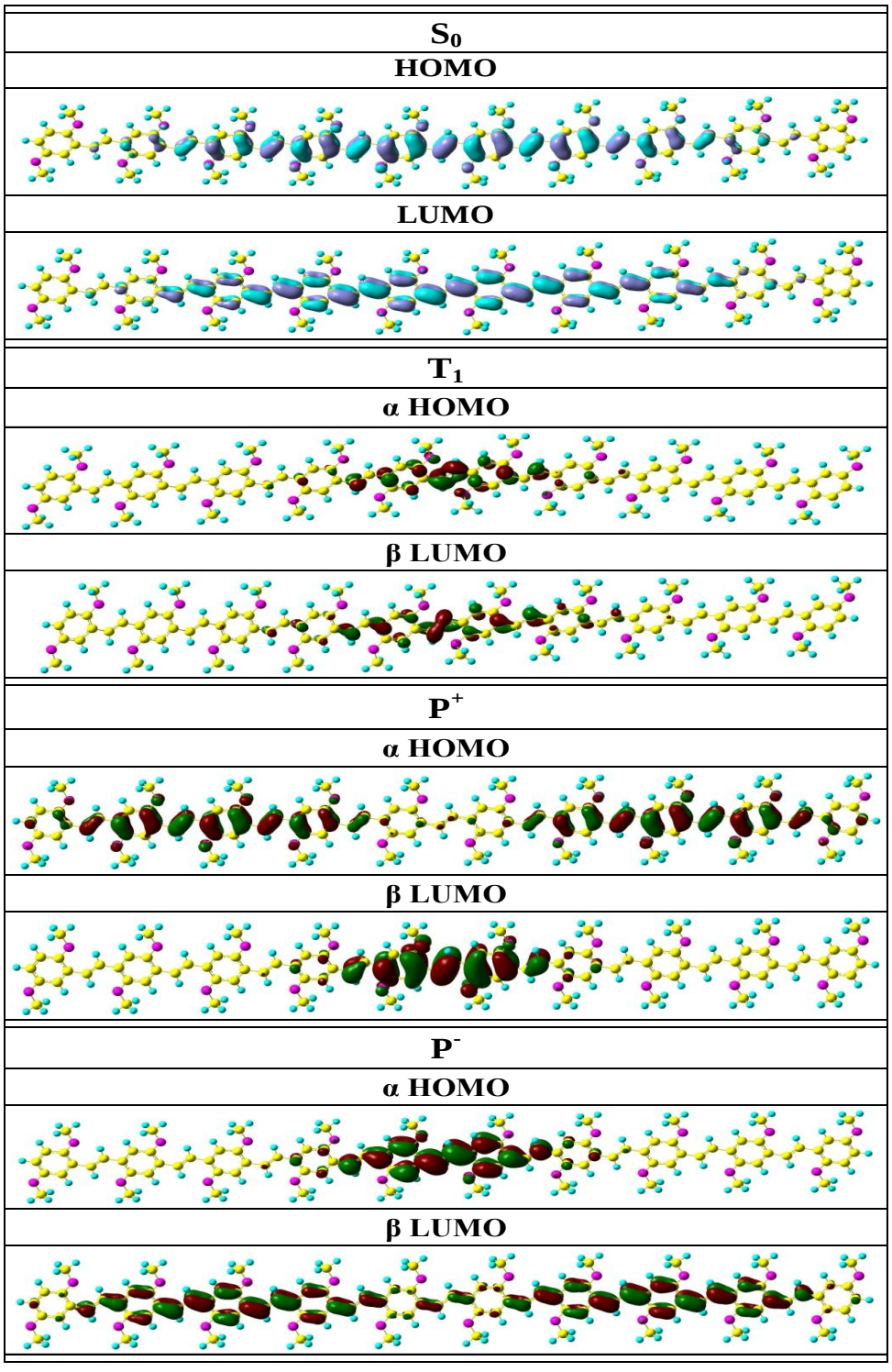

Figure 6.6: Characteristic HOMO and LUMO molecular orbitals of S_0, T_1, P^+ and P^- states in their corresponding native geometries calculated at LC-wPBE/6-31G* level in the presence of solvent for MEH-PPV oligomer.

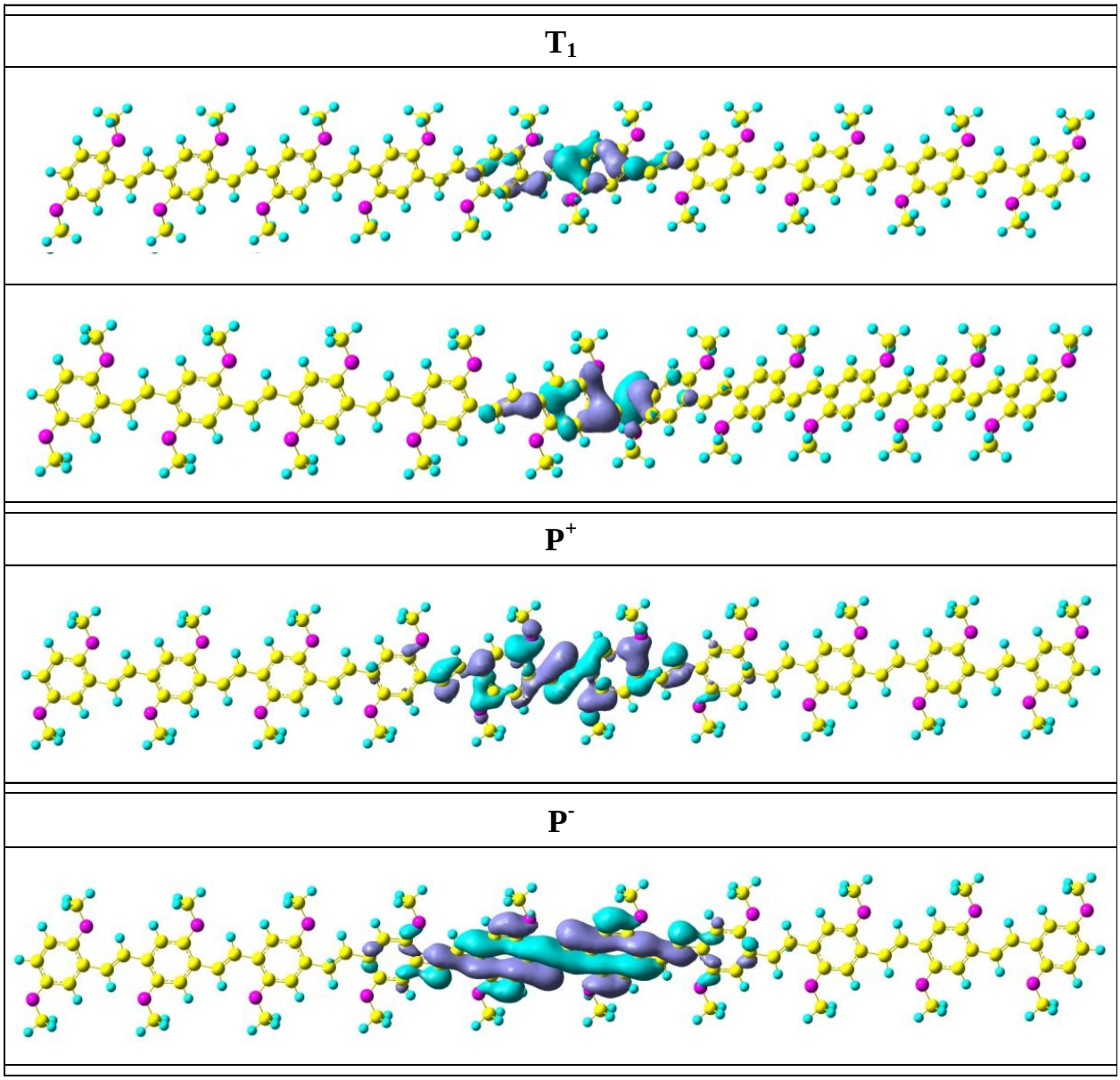

Figure 6.7: Characteristic natural orbitals (NOs) for the singly occupied electronic levels for T_1, P^+ and P^- excitations in their corresponding native geometries calculated at LC-wPBE/6-31G* in the presence of solvent for MEH-PPV oligomer.
For T_1, only two orbitals shown have unit occupation. Whereas both P^+ and P^- have only one NO each with a single occupation number.

Finally, orbital analysis of electronic excitations can be conducted using the natural orbital (NO) representation for the singly occupied electronic levels as shown in Figure 6.7 for T_1, P^+ and P^- excitations calculated at LC-wPBE level in the presence of the polarizable

dielectric medium. These NOs are defined as the eigenfunctions of the spinless one-particle electron density matrix. The T_1 state has only two orbitals with a single occupation as shown in the figure whereas P^+ and P^- have only one NO with unit occupation. These plots visually show that localization of T_1 state is more pronounced compared to P^+ or P^- excitations. Similar plots obtained for calculations in vacuum are shown in Figure 6.S4.

6.7 Conclusions

In summary, we presented a detailed computational study and analysis of the energetics and spatial delocalization of significant electronic states in conjugated oligomers (phenylene vinylenes), thus providing deeper understanding of the physics controlling localized excitations in organic electronic materials for technological applications. Use of the long-range-corrected DFT functionals, such as LC-wPBE, is found to be crucial in order to predict physically correct spatial localization of all electronic excitations considered. In these models, we observe that the electronic localization of charged P^+ and P^- states is mostly decided by polarization properties of the surrounding media, while exhibiting lesser dependence on the molecular geometry. However, localization of the neutral S_1 and T_1 ($T_1^\dagger$) states is weakly dependent on polarization. For these excitations, the self-trapping of their electronic wavefunctions mostly follows the lattice distortion when TD-DFT methodology is used. In particular, TD-DFT calculated S_1 and $T_1^\dagger$ excitations are found to be strongly delocalized along the oligomer chain at the uniform ground state S_0 geometry, owing to the non-variational construction of the excited state wavefunction. In contrast, mean-field calculated P^+, P^- and T_1 states are always spatially localized even in S_0 geometry, independent of the oligomer length used. Polaron P^+ and P^- formation is signified by the presence of the localized states for the hole or the electron deep inside the HOMO-LUMO

gap of the oligomer as a result of the orbital stabilization at the LC-wPBE level. The broadening of the HOMO-LUMO band gap for the T_1 exciton compared to the charged (P^+ and P^-) states is associated with the inverted bond length alternation observed at this level. Neutral excitons have higher binding energies than polarons. However, the trends observed for solvation energies are completely reversed. LC-wPBE predicts the highest binding and solvation energies compared to other DFT levels used in this study. Thus, our investigation allows one to choose an appropriate electronic structure methodology and provides an analysis of the essential electronic excitations controlling energy-transfer and charge-transport processes in opto-electronic devices.

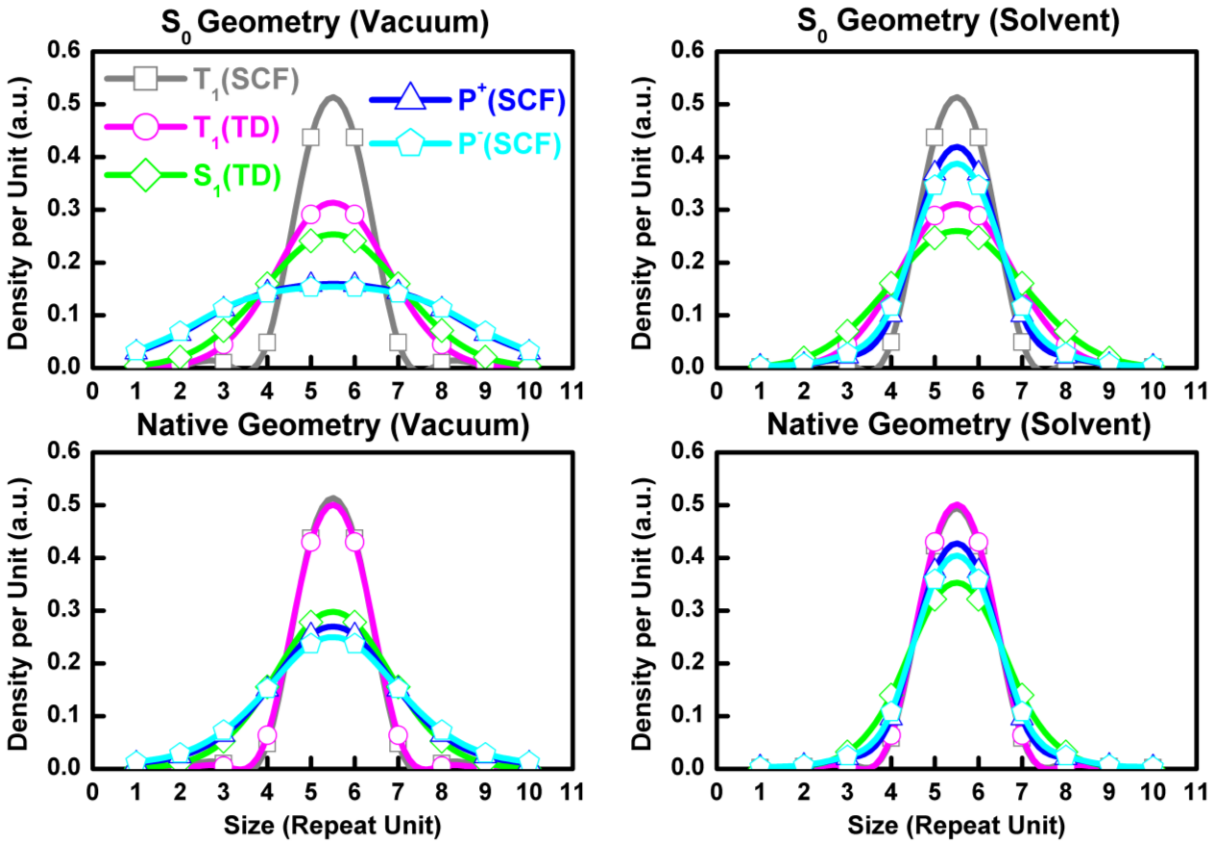

Figure 6.S1: Electronic density per repeat unit (a.u.) of MEH-PPV oligomer consisting of 10 repeat units for all the excitations (T_1, P^+, P^-, $T_1^\dagger$ and S_1) in S_0 state geometry (top panel) and their corresponding native geometries (bottom panel) calculated at BHandHLYP level using 6-31G* basis.

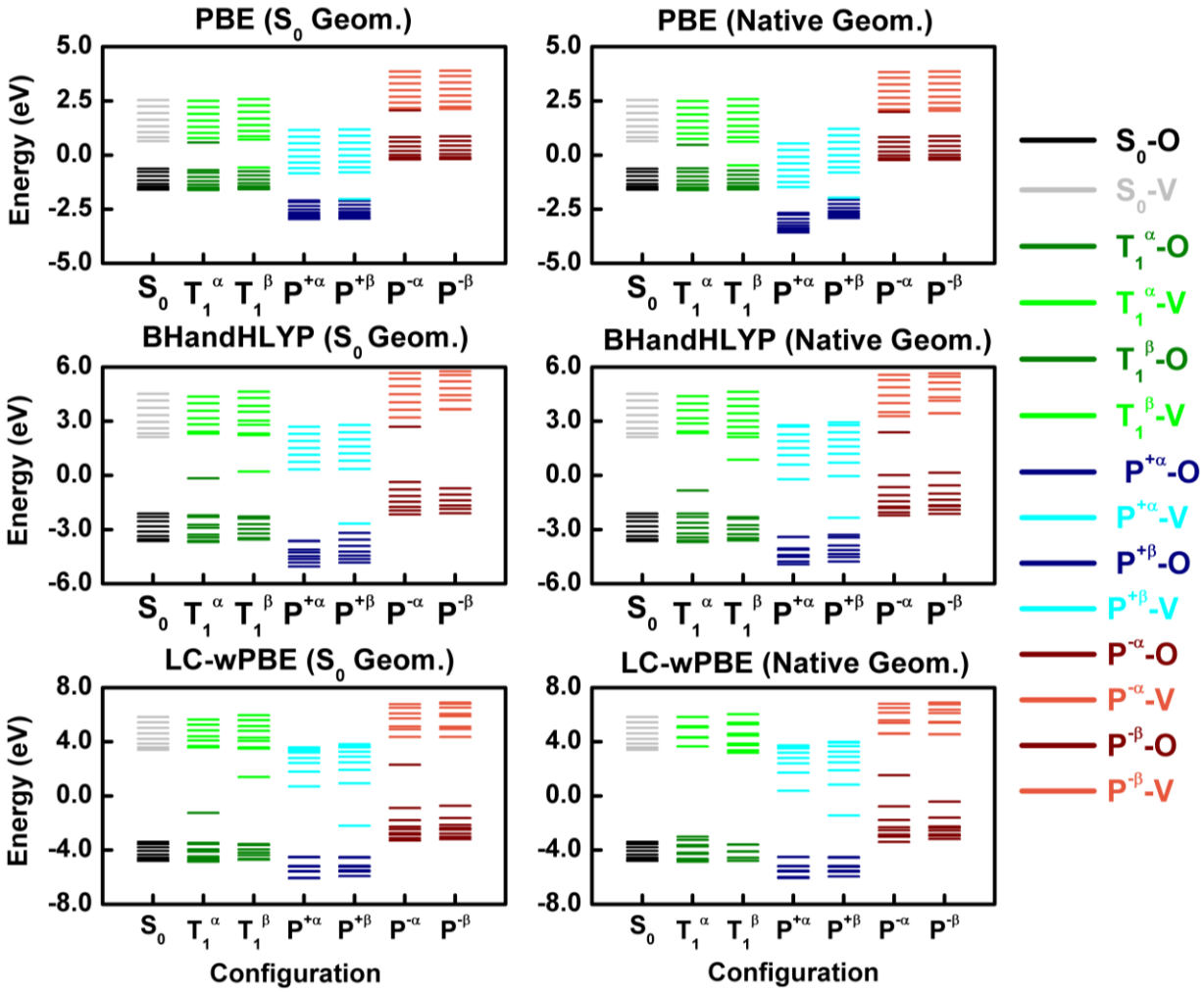

Figure 6.S2: Density of Kohn-Sham states for S_0, P^+, P^- and T_1 states of MEH-PPV oligomer comprised of 10 repeat units computed at PBE, BHandHLYP and LC-wPBE levels with 6-31G* basis set for S_0 state geometry (left panel) and their corresponding native optimal geometries (right panel).

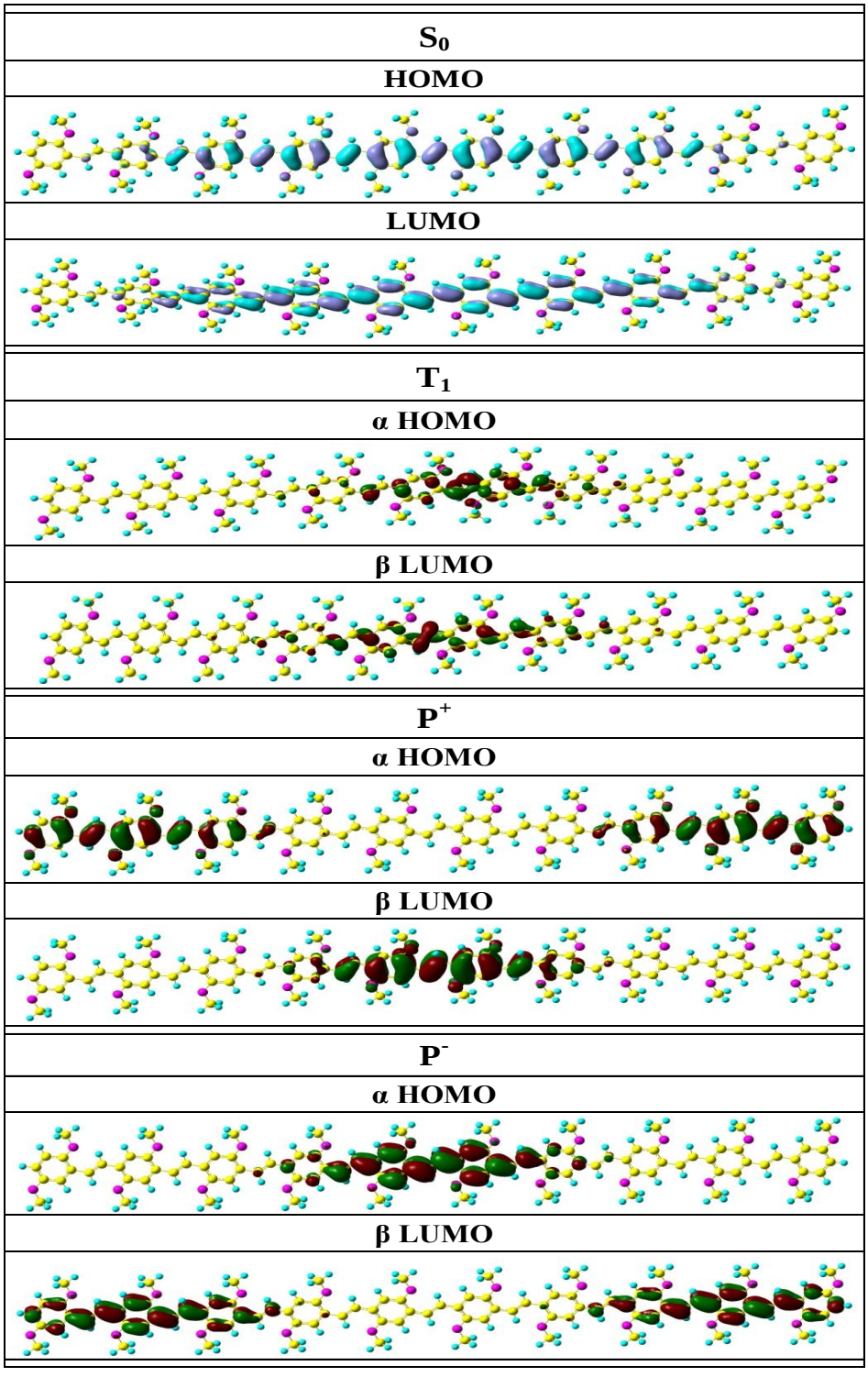

Figure 6.S3: **Characteristic HOMO and LUMO molecular orbitals of S_0, T_1, P^+ and P^- states in their corresponding native geometries calculated at LC-wPBE/6-31G* level in vacuum for MEH-PPV oligomer comprised of 10 repeat units.**

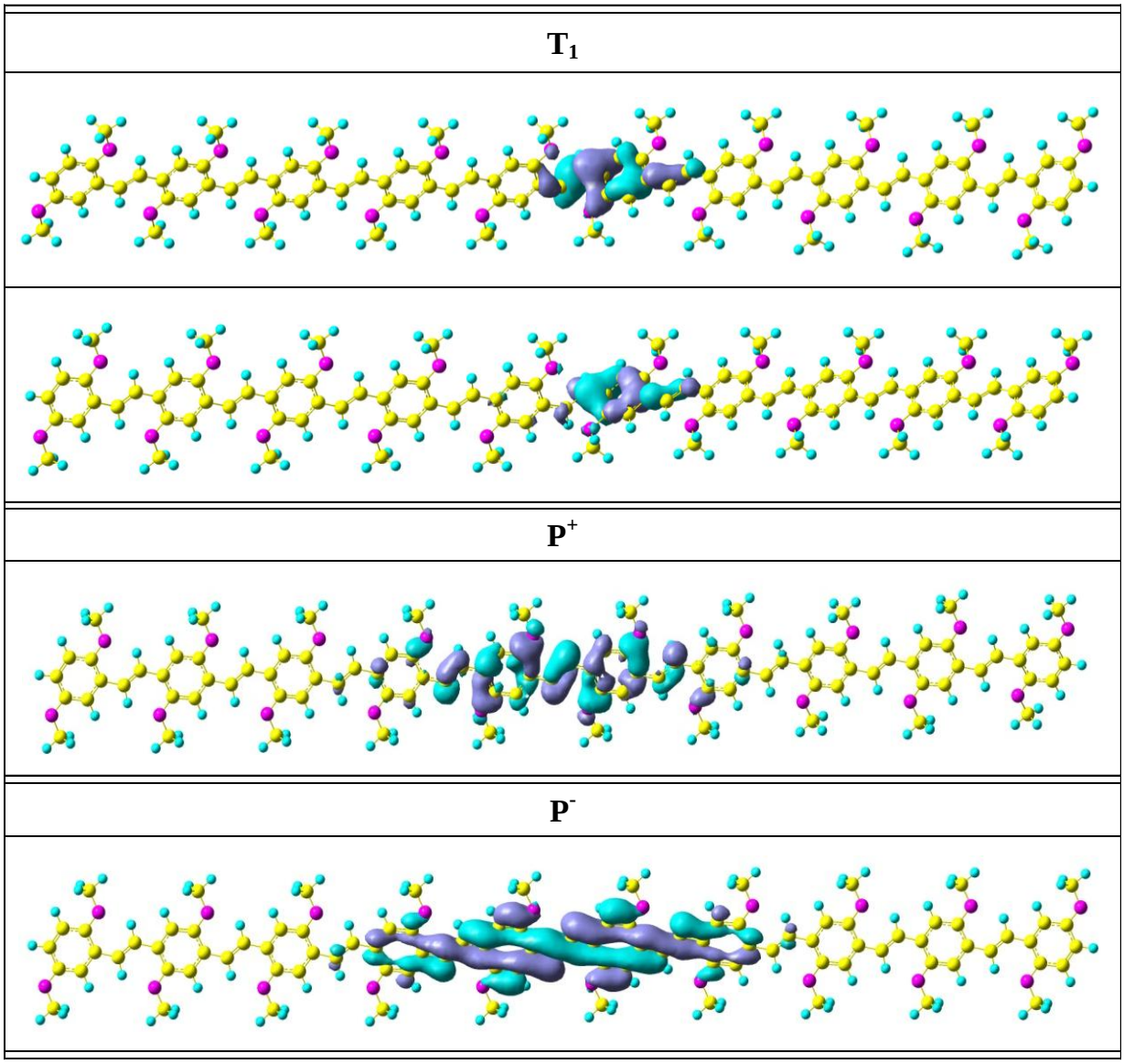

Figure 6.S4: Characteristic natural orbitals (NOs) for singly occupied electronic levels for T_1, P^+ and P^- excitations in their corresponding native geometries calculated at LC-wPBE/6-31G* in vacuum for MEH-PPV oligomer comprised of 10 repeat units.

CHAPTER 7 EFFECT OF *trans* AND *cis* ISOMERIC DEFECTS ON THE LOCALIZATION OF CHARGED EXCITATIONS

In Chapter 5, we have observed the particle-hole symmetry is preserved in trans-isomeric forms of PPV [poly (p-phenylene vinylene)] and its derivative MEH-PPV [poly{2-methoxy-5-(2-ethyl-hexyloxy)-PPV}]. However in an experimental study, McCamey *et al*.[68] predicted substantial differences in the response of the hyperfine field exerted by the opposite charge carriers constituting polaron pairs in organic light-emitting diodes.[98, 102] The charge-transfer properties were also shown to vary for different isomeric forms of PPV derivatives. This has led us to investigate the influence of various conformational defects of *trans* and *cis* nature on the energetics and localization of the charged excitations in PPV and MEH-PPV. We observe that the extent of self-trapping for positive (P^+) and negative (P^-) polarons is highly sensitive on the molecular and structural conformation, and distribution of atomic charges within the polymers. We observe the P^- state is localized on the *weak*-trans defect in comparison to P^+, which is localized away from the defect position for MEH-PPV. At the same time, the defect of strong-*cis* nature repels both the charges. So, the particle-hole symmetry is broken with the introduction of weak-*trans* defects. We emphasize on the crucial role played by the polarizable dielectric environment in predicting the asymmetry in the P^+ and P^- excitations for MEH-PPV oligomer having *trans* and *cis* distortions. The electrons are reported to be more localized than holes in consistent with experiment.[68] For unsubstituted PPV chains, the particle-hole symmetry is restored for all the conformation types and in the presence of a dielectric. The differences in the behavior of PPV and MEH-PPV is rationalized based on their orbital energetics and atomic charge distributions. The P^- states exhibit larger binding, solvation and reorganization energies

than P^+. We attribute this to the ability of carbon to accommodate more partial negative charge resulting in the larger stabilization of C-H interactions in comparison to P^+. Higher reorganization energies contribute to lower carrier hopping rates according to Marcus hopping model.[166] The deeper analysis of the predicted double wells for *trans* distorted MEH-PPV geometries elucidate the higher hole-transport properties than electrons. Thus, we see that various types of defects influence the behavior and drift mobilities of the charge carriers in substituted oligo (phenylene vinylenes).

7.1 Computational Details

We study the positive (P^+) and negative (P^-) polarons using long-range-corrected LC-wPBE functional for ten repeat units of *trans* and *cis* isomers of PPV and MEH-PPV oligomers with different types of conformational defects along their length. Each repeat unit consists of a phenyl ring attached to a vinyl bridge. The importance of the inclusion of long-range corrections to the exchange for the description of these excitations in accordance with experimental measurements has already been showed in Chapters 5 and 6. The defects of *trans* nature are introduced by applying a 180° rotation of the dihedral between phenyl and vinyl units, forming a weak bent along the length of the chain. Similarly, *cis* defect is produced by a strong bent involving the 180° rotation of one of the vinyl bonds along the polymer. Hence, we refer to "weak-*trans*" and "strong-*cis*" defects as "small kink (SK)" and "large kink (LK)" also, respectively. These kinks break the symmetry of the π-conjugation along the chain into two distinct segments of equal or unequal lengths. We study the effect of the conformational defects of *trans* and *cis* nature on the localization of the charged excitations in comparison to the undistorted *trans* geometry. Different configurations belonging to the same isomer type differ in

their respective position of the kink on the chain. Figure 7.1 presents all the geometry types of MEH-PPV oligomer studied in this chapter: (a) *trans*, (b) *trans*-SK (6-3), (c) *trans*-SK (7-2), (d) *cis*-LK (4-4) and (e) *cis*-LK (5-3). The left and right hand numerals in the parenthesis denote the number of vinyl bonds on either side of the kink.

All computations have been performed using the Guassian09 suite[5] and the 6-31G* basis set. In our calculation model, the alkoxy side chain groups OC_8H_{17} are replaced by OCH_3 in MEH-PPV to speed up the quantum calculations.

(a) *trans*

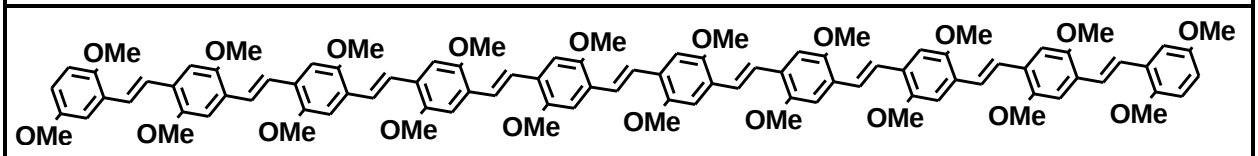

(b) *trans*-SK (6-3)

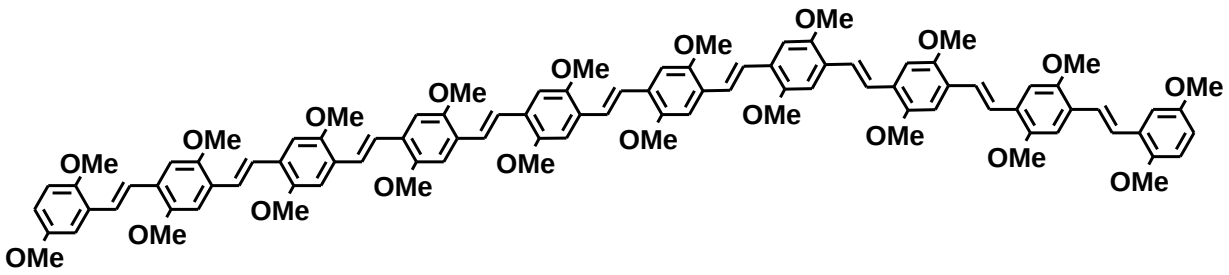

***trans*-SK (7-2)**

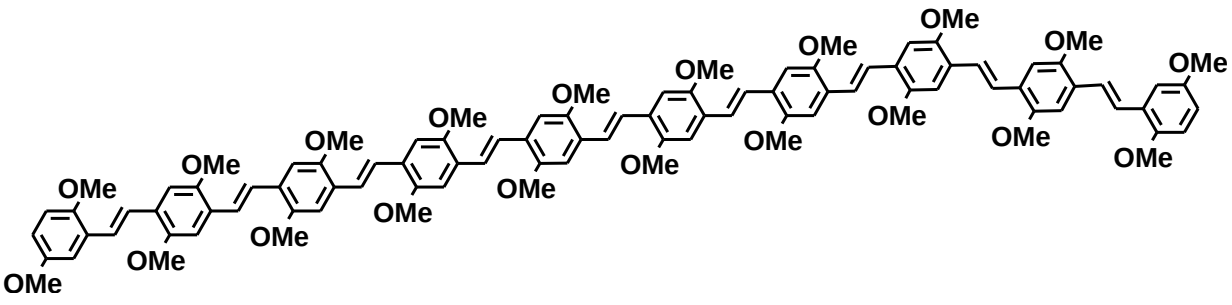

(c) *cis*-LK (4-4)

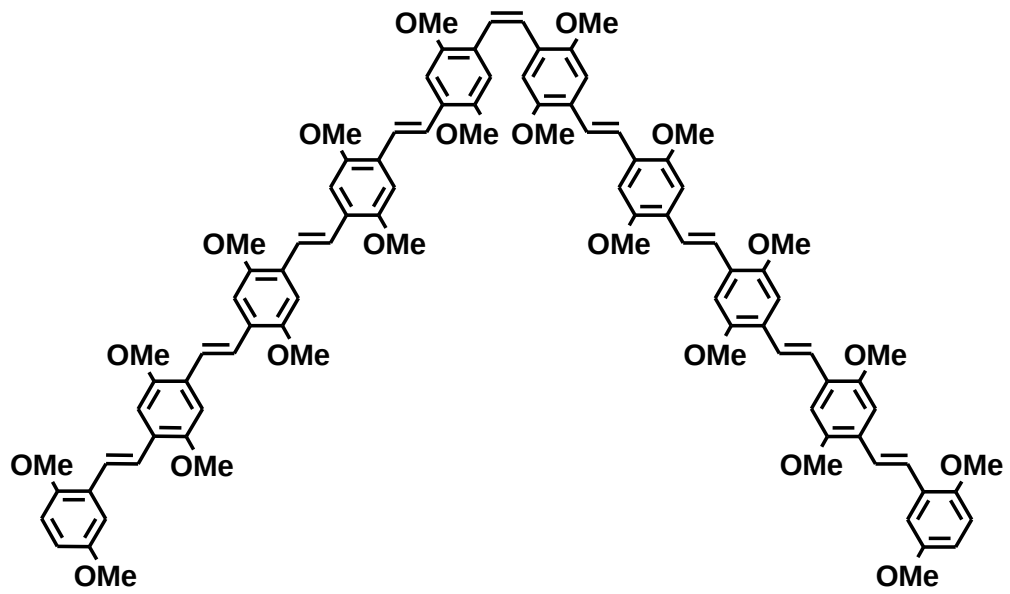
OMe
OMe
OMe

Optimal geometries of P^+ and P^- states have been obtained using standard self-consistent force (SCF) scheme. Different types of isomeric conformations of the PPV derivatives were shown to exhibit distinct nature of interactions with the polymer.[98] Therefore, we added a moderately polar solvent, acetonitrile (ε=37.5), via the conductor-like polarizable continuum (CPCM) model as implemented in Gaussian09 software package[5] in order to mimic the polymer's highly polarizable dielectric environment.

7.2 Role of Polarization in Localizing Different Isomeric Conformations

Figure 7.2 explores the effect of various defects on the localization properties of P^+ excitation for MEH-PPV oligomer. Plotted are the bond length alternation (BLA) of vinyl bonds (left panel) along the length of the chain for vacuum and solvent. The BLA parameter is defined as the difference between C-C single and double bonds in the vinyl bridge and determines the degree of Peierls distortion in conjugated molecular chains.[79] It is observed to reach its minimum, signifying the self-trapping of the positive polaron at the middle of the chain for the undistorted *trans* geometry both in vacuum and solvent. The P^+ polaron oxidizes the double bond in the vinyl linkage, therefore, reducing the BLA to almost zero after geometry optimization. However, a polar solvent tends to slightly increase the geometric distortion in accordance with our findings in Chapter 5. Next, we discuss the effect of various *trans* and *cis* defects along the backbone of the MEH-PPV polymer on the extent of spatial confinement of the P^+ state in vacuum. The dashed line in the figure denotes the position of the defect along the chain length.

.

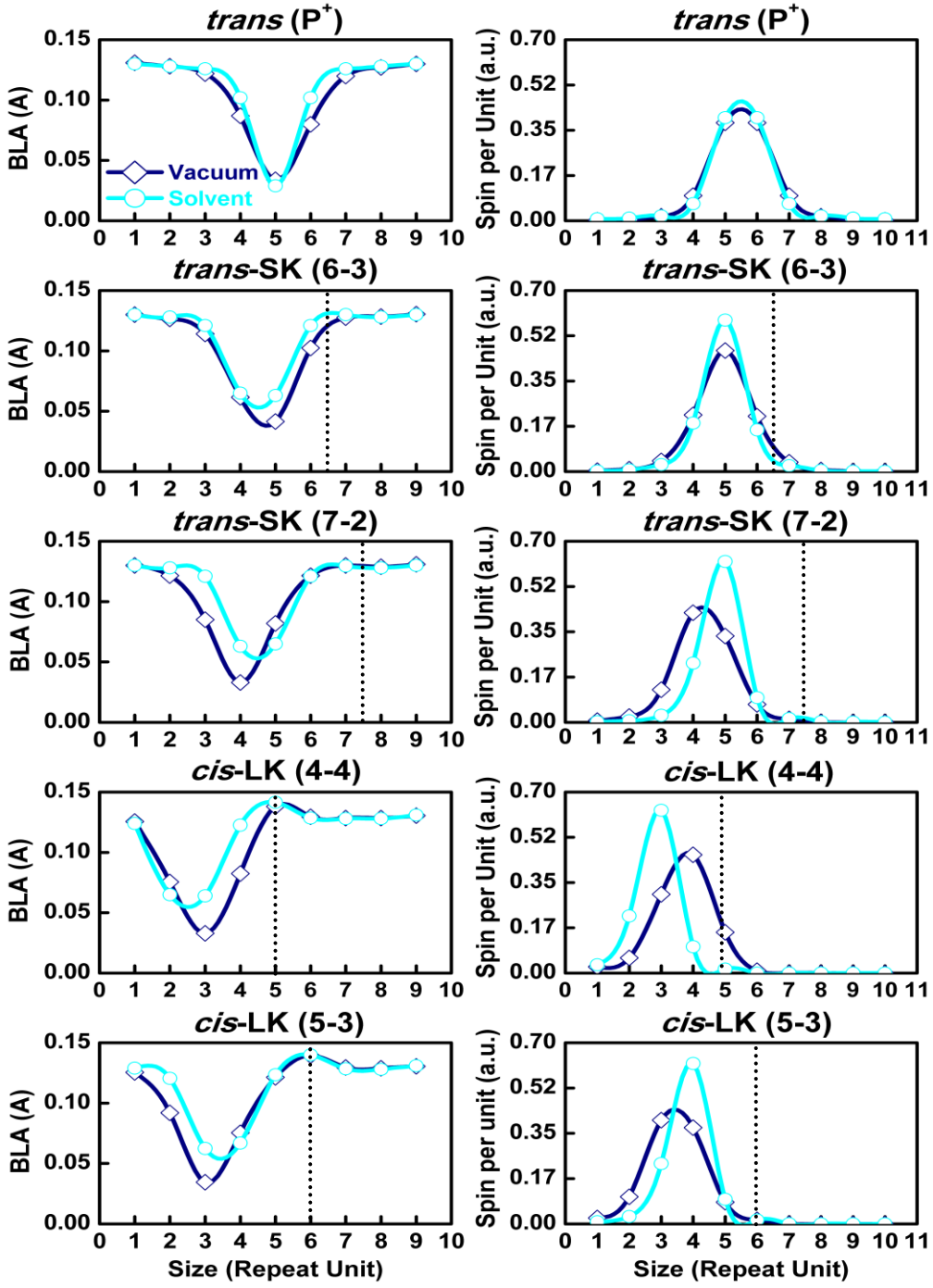

Figure 7.2: Variations of BLA (Å) (left) and Mulliken atomic spin densities (a.u.) per repeat unit (right) in MEH-PPV oligomer computed at LC-wPBE/6-31G* level for the optimal positive polaronic state (P^+) in vacuum and solvent.

The equilibrium state is calculated for five different geometrical conformations: *trans*, *trans*-SK (6-3), *trans*-SK (7-2), *cis*-LK (4-4) and *cis*-LK (5-3) as shown in Figure 7.1. The dashed line represents the defect position on the chain.

The P^+ excitation for geometries having various *trans* defects localizes close to the fourth vinyl bond on the longer conjugated segment of the oligomer, whereas it localizes on the third vinyl unit for both the *cis* conformations. This indicates that the hole is slightly more repelled by the defect for *cis* geometries in comparison to the distorted *trans* ones. As the *cis*-LK (4-4) configuration divides the oligomer chain into two segments of equal lengths, the hole has an equal probability to localize on either of them. We choose the left hand side for consistency with the results obtained for other configurations. Interestingly, we observe a decrease in the extent of spatial localization due to geometry relaxation with the inclusion of solvent for all the distorted (*trans* and *cis*) geometries in contrast to the undistorted *trans* one. The right panels in Figure 7.2 display the Mulliken atomic spin densities (difference in the spin of α and β molecular orbitals) integrated over each repeat unit (right panel) for the P^+ state. Spin density distributions signify the spatial confinement of the electronic excitation due to the polarization effects. These exhibit a similar order of localization as predicted by the BLA in vacuum. The addition of a polarizable medium (solvent) notably enhances the extent of electronic localization for the geometries with defects, which is in contrast to the behavior of the corresponding BLAs (left panels). Thus, we notice that the polarization effects play an important role in the spatial confinement of positive polaron due to the trapping of electronic wavefunction, which ultimately signifies the respective lattice distortions.

Similar to Figure 7.2, Figure 7.3 represents calculation localization properties of P^- states in MEH-PPV. The similarity of top panels in Figures 7.2 and 7.3 demonstrate particle- hole symmetry for the undistorted *trans* geometry in terms of the position and extent of their distortion along the chain.

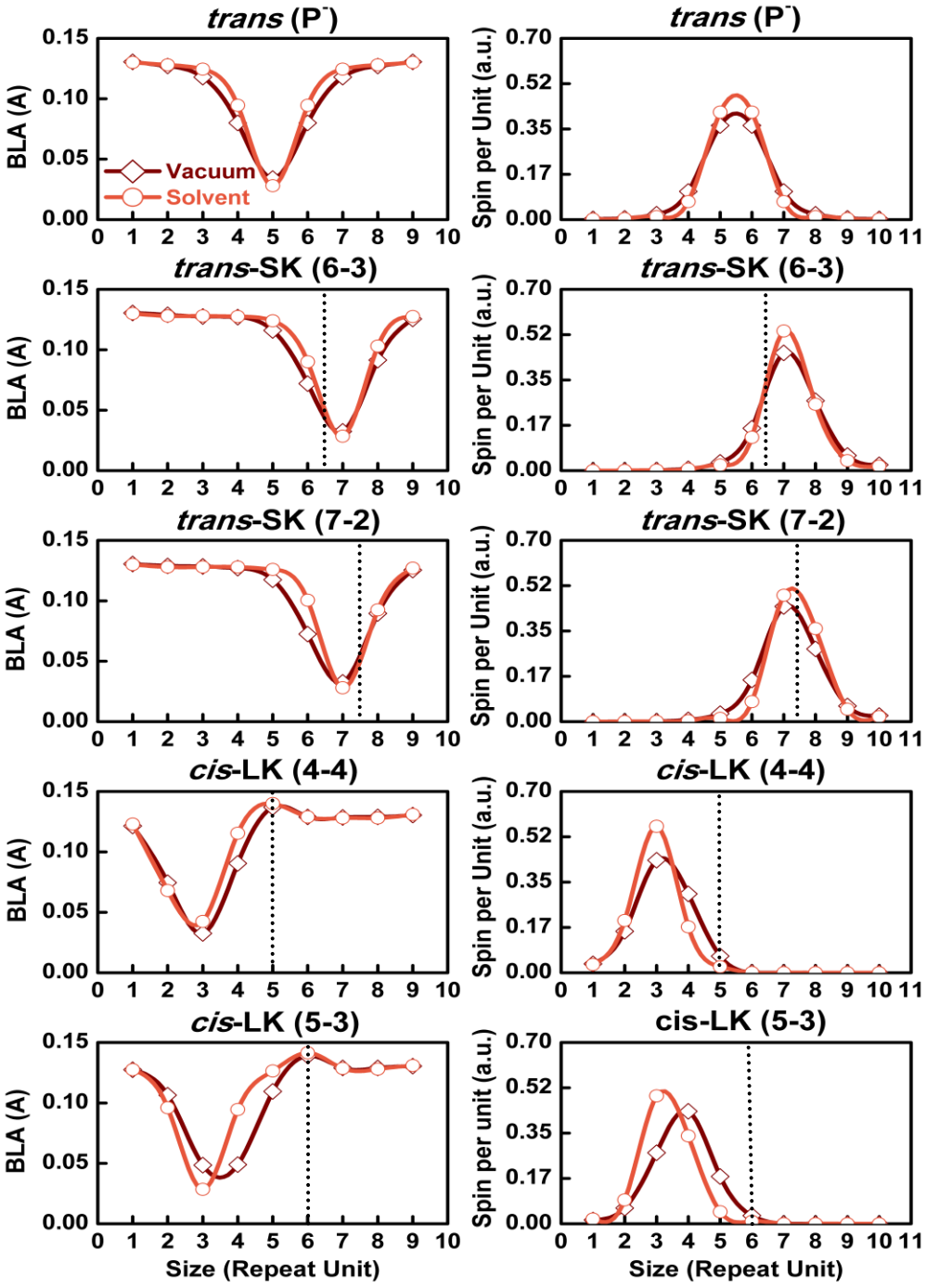

Figure 7.3: Same as Figure 7.2 but for the optimal negative polaronic state (P^-).

At the same time, P^- localizes around the seventh vinyl bond for distorted *trans* geometries in the vicinity of the defect position as judged by both BLA and spin density measures (middle row panels). Therefore, for the same configuration, electrons are attracted by the *trans* defect sites and holes are repelled. In contrast, the *cis* defect sites repel the injected electrons to the same extent as observed for holes (compare two bottom rows in Figures 7.2 and 7.3). Various conformational distortions on the chain exhibit negligible effect on the oligomer-solvent interactions for the P^- state in comparison to the undistorted *trans* geometry. The Mulliken atomic spin densities follow the same trends as BLA in vacuum and solvent. Therein, the polarization of the medium increases the extent of both the structural and electronic localization for negative polaron P^- unlike the trends observed for the positive polaron P^+.

7.3 Role of Side Group Substitution in Localizing Different Isomeric Conformations

Figure 7.4 summarizes the BLAs of P^+ and P^- states in MEH-PPV (right panel) in comparison to PPV (left panel). Only the calculations in the presence of a dielectric medium are shown. Both the polarons localize in the middle of PPV and MEH-PPV chains for their undistorted *trans* geometries (top panels in Figure 7.4). However, PPV exhibits different localization patterns than MEH-PPV for various *trans* and *cis* defects as discussed below. The P^+ and P^- polarons continue to localize in the middle of the PPV chain with weak distortions of *trans* nature, whereas the observed particle-hole symmetry is completely broken for MEH-PPV chains having the same nature of distortions. The P^- state now resides close to the defect position while P^+ stays away from it. Interestingly, we observe the particle-hole symmetry to be roughly preserved for PPV and MEH-PPV oligomers having strong-*cis* distortions.

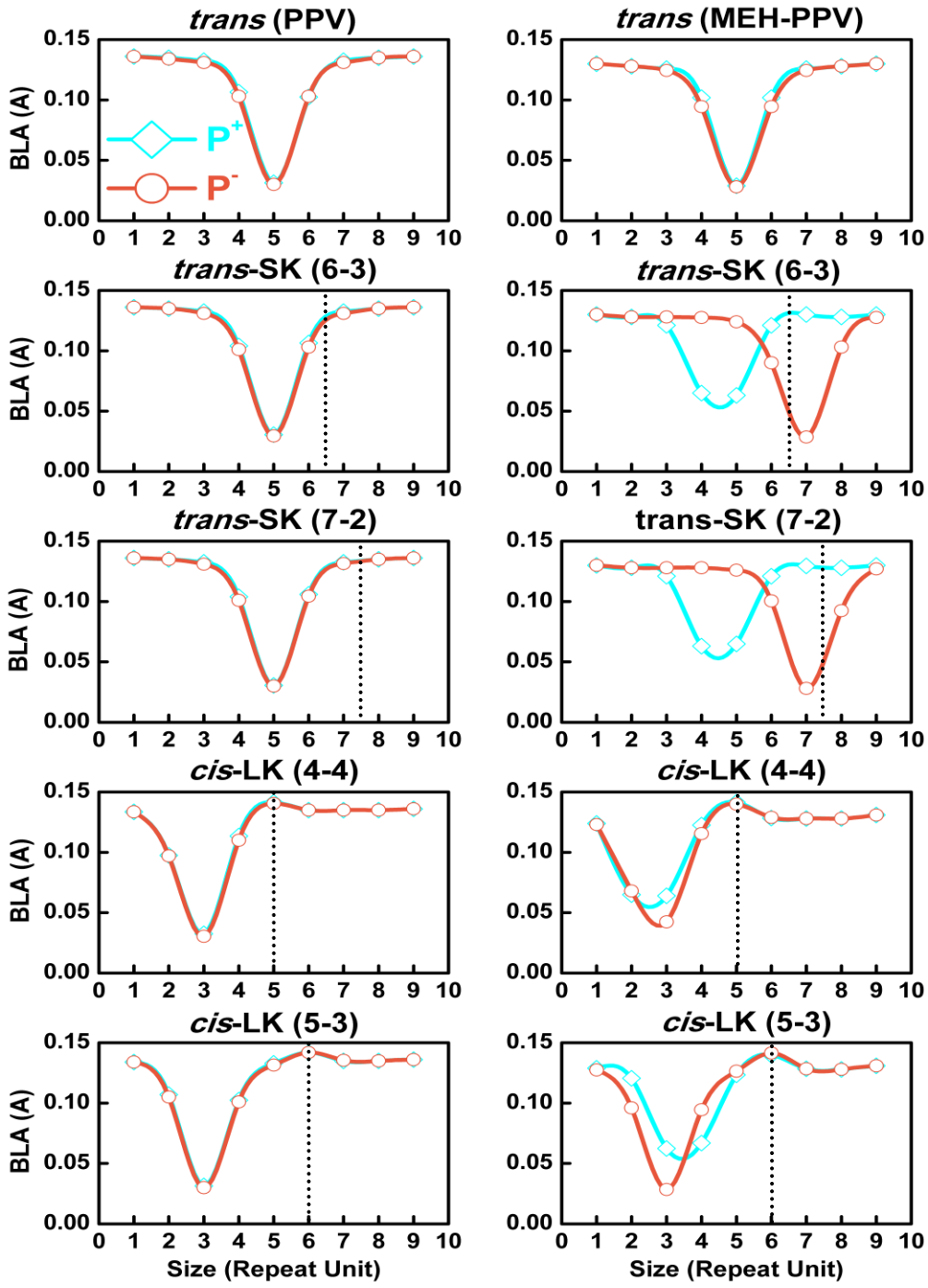

Figure 7.4: Variation of BLA (Å) for P^+ and P^- excitations in PPV (left) and MEH-PPV (right) oligomers calculated at LC-wPBE/6-31G* level in the presence of solvent.
The corresponding fully relaxed geometries are obtained for five different configurations: *trans*, *trans*-SK (6-3), *trans*-SK (7-2), *cis*-LK (4-4) and *cis*-LK (5-3). The dashed line represents the defect on the chain.

In both these systems, the electrons and holes are repelled away from the *cis* defect site. The characteristic sizes of the P^+ and P^- excitations are found to be identical for PPV for all the considered configurations. This trend changes for MEH-PPV, where the size of the P^+ excitation is larger compared to that of P^- with the introduction of defects. The size is defined as the full width at half-maximum in terms of the repeat units of the BLA plots of the oligomer chains. Thus, we observe that the interaction of solvent with oligo (phenylene vinylene) chains is highly sensitive to their molecular geometry. The different behavior of PPV and MEH-PPV is attributed to the presence of the alkoxy groups (OCH_3) on the phenyl rings in the latter distributing a complex set of local dipoles along the molecular backbone.

7.4 Role of Geometry Relaxation in Localizing Different Isomeric Conformations

The difference in the response of injected holes and electrons on MEH-PPV chains with weak-*trans* distortions intrigued us to further investigate these localization patterns as discussed below. We are interested in studying the behavior of holes (electrons) added to these systems in the native optimal geometries of P^- (P^+) states to understand whether the added holes (electrons) would still localize away from (close to) the weak-*trans* defect sites and be able to overcome the energy barrier for hopping. Figure 7.5 demonstrates the BLA (left) and spin density (right) of P^+ (P^-) excitations on the MEH-PPV chains relaxed in the neutral ground (S_0) and charged P^- (P^+) states in the presence of solvent. Plotted are *trans*-SK (6-3) (top) and *trans*-SK (7-2) (bottom) configurations. In this figure, we have used a composite notation "(X,Y)" where X indicates the initial optimal state of the system before adding a charge carrier, and Y denotes the final equilibrium state upon its addition. We observe that the system attains its equilibrium away from

(close to) the defect upon P^+ (P^-) excitation from the uniform S_0 state. In contrast, it relaxes close to (away from) the defect when starting from the optimal P^- (P^+) state for P^+ (P^-) excitation. This suggests the existence of two energy minima for P^+ and P^- states for MEH-PPV geometries with weak-*trans* defects. The system at the global minimum of P^+ (P^-) state attains the local minimum configuration for P^- (P^+) with the addition of an electron (hole).

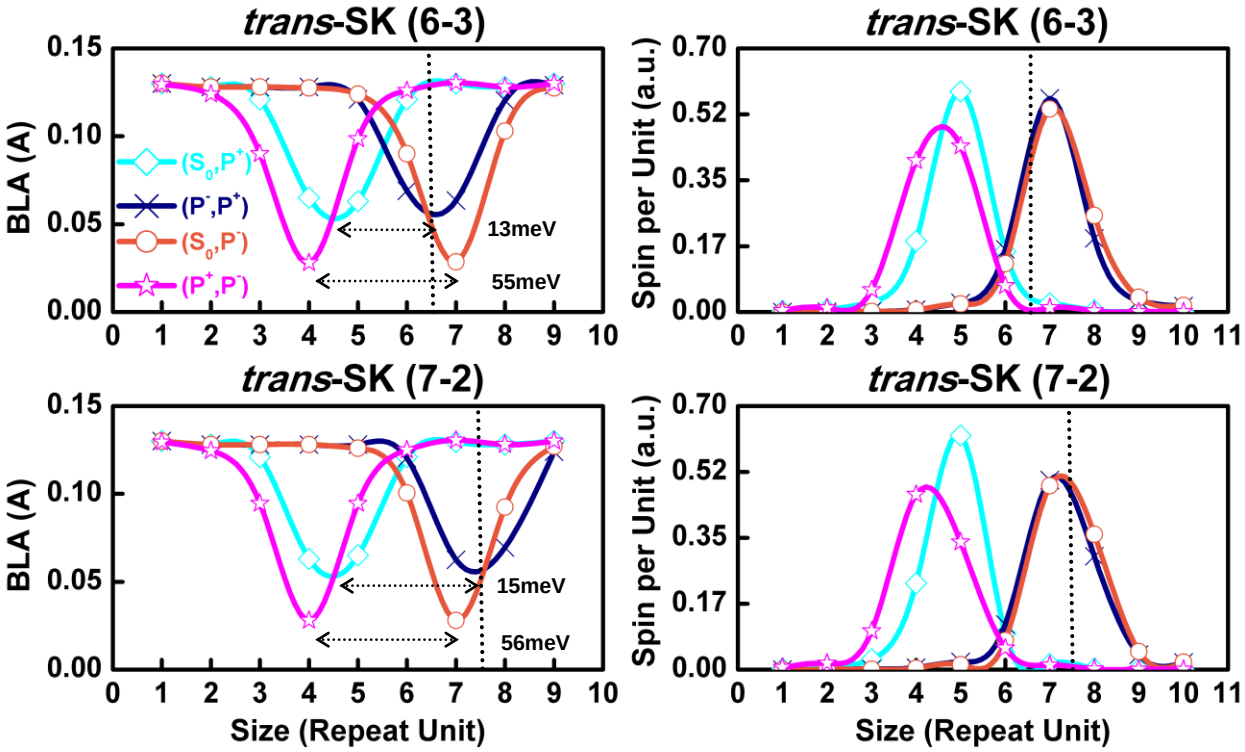

Figure 7.5: Variation of BLA (Å) (left) and Mulliken atomic spin densities (a.u.) per repeat unit (right) of the MEH-PPV oligomer in *trans*-SK (6-3) and *trans*-SK (7-2) geometrical configurations for P^+ and P^- polarons.
The calculations are performed at LC-wPBE/6-31G* level in the presence of a dielectric medium. We have used a notation "(X,Y)" in the legend, where X denotes the initial optimal state of the system before adding a charge carrier, while Y denotes the final equilibrium state. The dashed line represents the defect position on the chain.

For P^+, the two BLA minima for *trans*-SK (6-3) geometries differ by 13meV (in energy) which is less than the average thermal fluctuations at room temperature (~25meV), whereas they differ by 55meV for P^- excitation. This also implies that the average drift mobility for the hole in these

systems is higher than the electron, to be discussed in detail later in this section. Figure 7.S1 exhibits a similar trends for the spin localization of the injected holes (electrons) into the weak *trans*-distorted systems optimized in P^- (P^+) states and establishes the generality of our observations.

Our hypothesis for the existence of double-well potential energies for P^+ and P^- states (Figure 7.5) can be explored in-depth from an alternate perspective. Figure 7.6 shows the BLA plots for the optimal P^+ and P^- states when starting from the nine different initial configuration geometries for the *trans*-SK (6-3) MEH-PPV chains in the presence of the solvent. The BLA of the initial states vary in their position of the vinyl bond from one end of the chain to the other as depicted in Figure 7.S2. The top panel of Figure 7.6 shows that the system attains equilibrium at two specified (4th and 7th units) positions on the chain irrespective of the initial state of injected holes and electrons. For P^+, the global minimum is away (4th unit) from the defect, while it is observed to be close (7th unit) to the defect site for P^- excitation. The positions of the local minima for both are excitations are, however, reversed. The potential energy barriers between the two BLA minima (global and local) are predicted to be 14.7 meV for P^+ and 53.9 meV for P^-. These observations are in accordance with the results contained in Figure 7.5 and validate the double-well energy potential surfaces for the charged species for *trans*-SK MEH-PPV geometries. The middle panels in Figure 7.6 depict BLA plots for the transition states between the two optimal states for P^+ and P^-, each. Finally, the bottom panels sketch the energy diagram for the two final optimal states attained for P^+ and P^- excitations along with their corresponding transition states. The transition states are lower by 0.2meV for P^+ and higher by 5.1meV for P^- from their corresponding local minima. This indicates a potential for deeper negative polaron trapping in MEH-PPV materials.

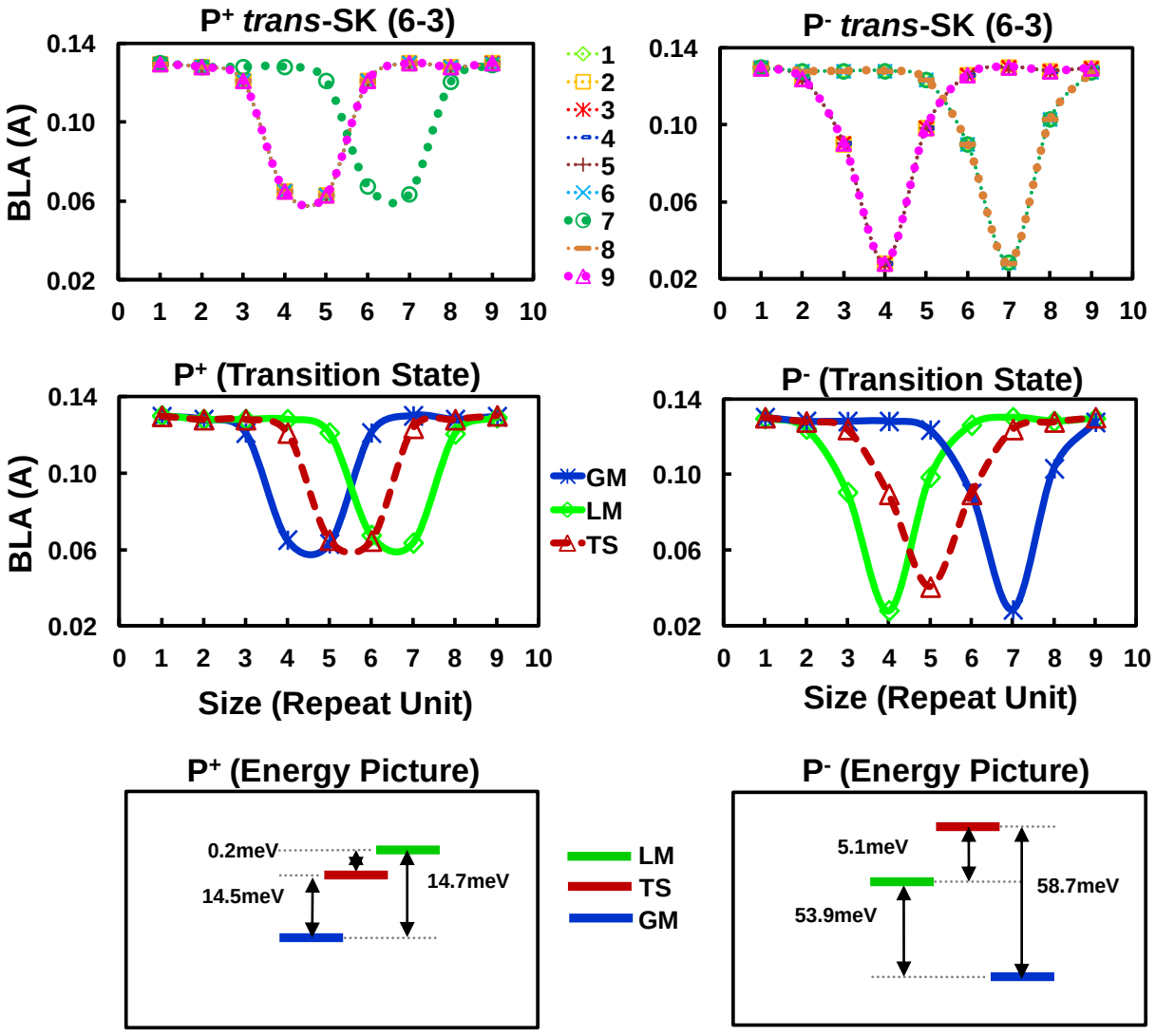

Figure 7.6: The top panel display the BLA (Å) of MEH-PPV oligomer in *trans*-SK (6-3) geometrical configuration for the P^+ and P^- polaronic excitations calculated at LC-wPBE/6-31G* level in the presence of the solvent.
The BLA is shown for 9 distinct states presented in Figure 7.S2. The middle panels display the BLA plots for the global and local maxima (GM and LM) for P^+ and P^- states along with their corresponding transition states (TS). The bottom panels sketch the respective energy picture.

7.5 Influence of Isomeric Defects on Orbital Energetics

We further analyze trends in the excitation binding and reorganization energies (Table 7.1) due to geometry relaxation, and solvation energies (Table 7.2). Table 7.1(A) summarizes the

binding energies calculated for P^+ and P^- states in PPV and MEH-PPV oligomers for five studied geometry types in vacuum and solvent. Binding energy is defined as the difference between the total energy of the excitation in the neutral (S_0) geometry and that in its fully relaxed charged-state configuration (X). Binding energy is an important parameter controlling the charge transport in conjugated polymers.[73]

Table 7.1: Binding and reorganization energies (eV) of 10 repeat units of PPV and MEH-PPV oligomers for P^+ and P^- excitations for *trans*, *trans*-SK (6-3), *trans*-SK (7-2), *cis*-LK (4-4) and *cis*-LK (5-3) conformations calculated at LC-wPBE/6-31G* level both in vacuum and solvent.

System	PPV				MEH-PPV			
Excitation (X)	P^+		P^-		P^+		P^-	
Medium	V	S	V	S	V	S	V	S
Conformation	(A) Binding Energy [$E(S_0,X)-E(X,X)$] (eV)							
trans	0.41	0.29	0.44	0.31	0.29	0.26	0.31	0.28
trans-SK (6-3)	0.39	0.30	0.43	0.32	0.29	0.23	0.34	0.33
trans-SK (7-2)	0.39	0.30	0.42	0.33	0.29	0.23	0.34	0.33
cis-LK (4-4)	0.60	0.31	0.66	0.34	0.34	0.30	0.40	0.27
cis-LK (5-3)	0.41	0.31	0.44	0.34	0.29	0.22	0.31	0.28
	(B) Reorganization Energy [Binding Energy+{$E(X,S_0)-E(S_0,S_0)$}]							
trans	0.75	0.57	0.79	0.60	0.62	0.53	0.65	0.58
trans-SK (6-3)	0.73	0.58	0.78	0.61	0.61	0.47	0.70	0.63
trans-SK (7-2)	0.73	0.58	0.78	0.62	0.62	0.47	0.70	0.63
cis-LK (4-4)	0.93	0.59	1.01	0.62	0.60	0.47	0.67	0.57
cis-LK (5-3)	0.76	0.59	0.79	0.63	0.62	0.47	0.65	0.57

Various *trans* and *cis* defects have no marked effect on the binding energies of P^+ and P^- states for PPV and MEH-PPV oligomers. Except for *cis*-LK (4-4) geometry in PPV chain, the reported energies are higher by 0.2eV than the rest of the geometries. Addition of a polarizable

medium reduces the binding energies for PPV and MEH-PPV. However, the geometry relaxation effects in the presence of a polar solvent are much more pronounced in PPV than for MEH-PPV. We observe that the binding energies for P^+ states are smaller in magnitude than those for P^- in vacuum and solvent. Not surprisingly, this difference is much more pronounced (>0.1eV) for weak *trans* conformations of MEH-PPV in the presence of solvent. We attribute this effect to the particle-hole symmetry not being preserved for the *trans* distortions along the MEH-PPV chains. Overall the binding energies for PPV are higher than those for MEH-PPV. Figure 7.S3 examines the density of single-particle states (Kohn-Sham orbitals) for P^+ and P^- excitations in their corresponding native states for five different geometry types for MEH-PPV. The detailed description of these states for undistorted *trans* geometry has been provided in Chapter 6. We do not observe any difference in the Kohn-Sham orbitals with the introduction of *trans* or *cis* defects into the system. However, the similar values of the binding energies for each of these geometry types already suggest this.

Reorganization energies are reported in Table 7.1(B). The reorganization energy is defined as the sum of two geometry relaxation energies: one is the binding energy and the other is the total energy of the neutral (S_0) state in the charged-state geometry (X) and that in S_0 geometry for organic crystals. This signifies the geometrical change in conjugated polymers upon excitation by a charge carrier.[102] According to the Marcus hopping model,[166] the reorganization energies are inversely proportional to the charge carrier hopping rates determining their transport properties in π-conjugated systems. All distorted geometry types (*trans*-SK and *cis*-LK defects) considered in this work are observed to show similar hole and electron transport properties for PPV in solvent, unlike observed for MEH-PPV. The *trans* and *cis* distorted geometries exhibit higher hole-transport properties (lower reorganization energies) than electron-

transport properties for MEH-PPV. Further, the difference in the energies for P^+ and P- for the distorted *trans* geometries is higher by 0.16eV in comparison to the *cis* ones. Inclusion of a polarizable medium provides a much higher stabilization for the P^+ states for distorted *trans* and *cis* geometries than for P^- states observed in MEH-PPV oligomers. This is attributed to the different characteristic sizes (localization strengths) for the hole and electron for MEH-PPV geometries (Figure 7.4). In addition, for *trans* defects the P^+ and P^- excitations are localized at two different positions on the MEH-PPV chain. Hence, the predicted reorganization energies are in close agreement with the trends observed for their corresponding localization strengths (Figure 7.4).

Table 7.2: Solvation energies (eV) of PPV and MEH-PPV oligomers for P^+ and P^- excitations for all five geometrical conformations calculated at LC-wPBE/6-31G* level.

System	**PPV**		**MEH-PPV**	
Excitation (X)	**P^+/P^-**		**P^+/P^-**	
Conformation	**Solvation Energy $[E(S_0,X)_v$-$E(S_0,X)_s]$(eV)**			
trans	2.13	2.38	2.52	3.37
trans-SK (6-3)	2.10	2.35	2.55	3.38
trans-SK (7-2)	2.10	2.34	2.57	3.37
cis-LK (4-4)	2.27	2.58	2.50	3.34
cis-LK (5-3)	2.08	2.34	2.55	3.32

Table 7.2 reports the solvation energies for P^+ and P^- states of PPV and MEH-PPV oligomers. This quantity is defined as the difference between the total energy of the charged excitation (X) in vacuum and that in the solvent, both calculated using the S_0 geometry. We observe that the geometry types do not have much influence on the solvation energies for either of the excitations for PPV and MEH-PPV. A polar solvent seems to provide a greater

stabilization of about 0.8eV to the P^- state in comparison to P^+ for MEH-PPV. The difference in the solvation energies for P^+ and P^- states in PPV is half of that computed for these states in MEH-PPV. The observed asymmetry in P^+ and P^- solvation energies is due to the difference in the distribution of local atomic charges within P^+ and P^- charged chains of PPV. The larger P^- energies are attributed to the ability of carbons to accommodate more partial negative charge in comparison to P^+. This leads to the higher stabilization of the C-H interactions for P^- excitations.[96] Finally, the P^- energy values are observed to further increase for MEH-PPV due to the presence of the more electronegative oxygen atom.

7.6 Influence of Isomeric Defects on Orbital Analysis

Observed trends can be illustrated using the spatial distributions of various molecular orbitals. Figure 7.7 displays the characteristic HOMO and LUMO orbitals for P^+ and P^- states in their corresponding native geometries for the *trans*-SK (6-3) geometry of MEH-PPV oligomer in the presence of solvent. The highest energy valence state belongs to α orbitals whereas the lowest energy conduction state to the β orbitals. The β LUMO of P^+ represents a localized state of a positive polaron, while the α HOMO represents a polaronic state for P^- excitation. We observe P^- state to spread around the defect in contrast to P^+ excitation. Orbital analysis of electronic excitations was conducted using the natural orbital (NO) representation for the singly-occupied electronic levels as illustrated in Figure 7.8(A). The NOs are defined as the eigenfunctions of the spinless one-particle electron density matrix. The P^+ and P^- have only one NO with unit occupation localized away and on the defect, respectively. Finally, Figure 7.8(B) plots the Mulliken atomic spin density distributions for P^+ and P^- excitations in the presence of the polarizable dielectric medium for the *trans*-SK (6-3) geometry.

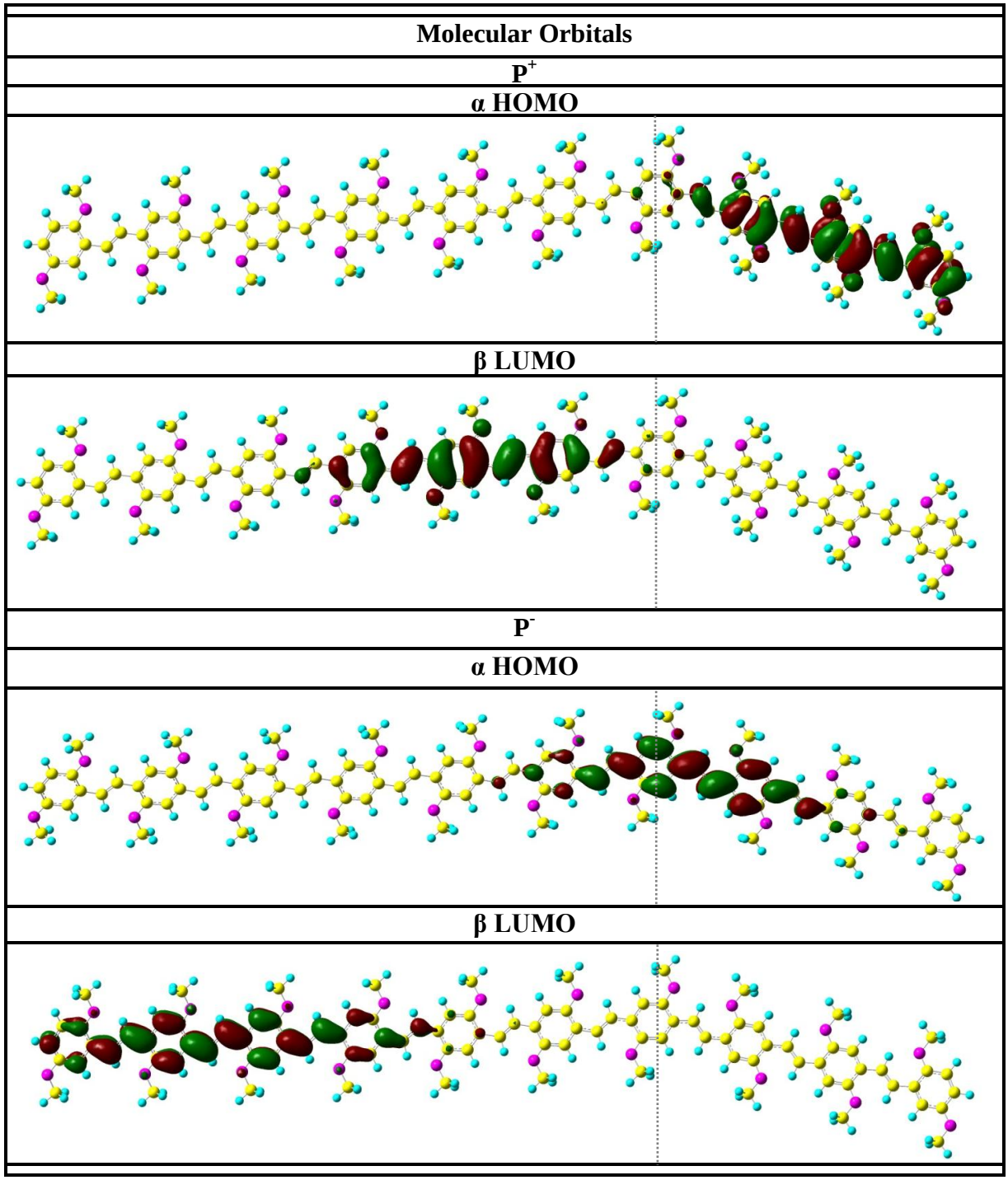

Figure 7.7: Characteristic HOMO and LUMO molecular orbitals of P^+ and P^- states in their corresponding native geometries calculated at LC-wPBE/6-31G* level in the presence of solvent for *trans*-SK (6-3) configuration of MEH-PPV oligomer.
The HOMO and LUMO represent alpha (α) and beta (β) electrons, respectively. The dashed line represents the defect position on the chain.

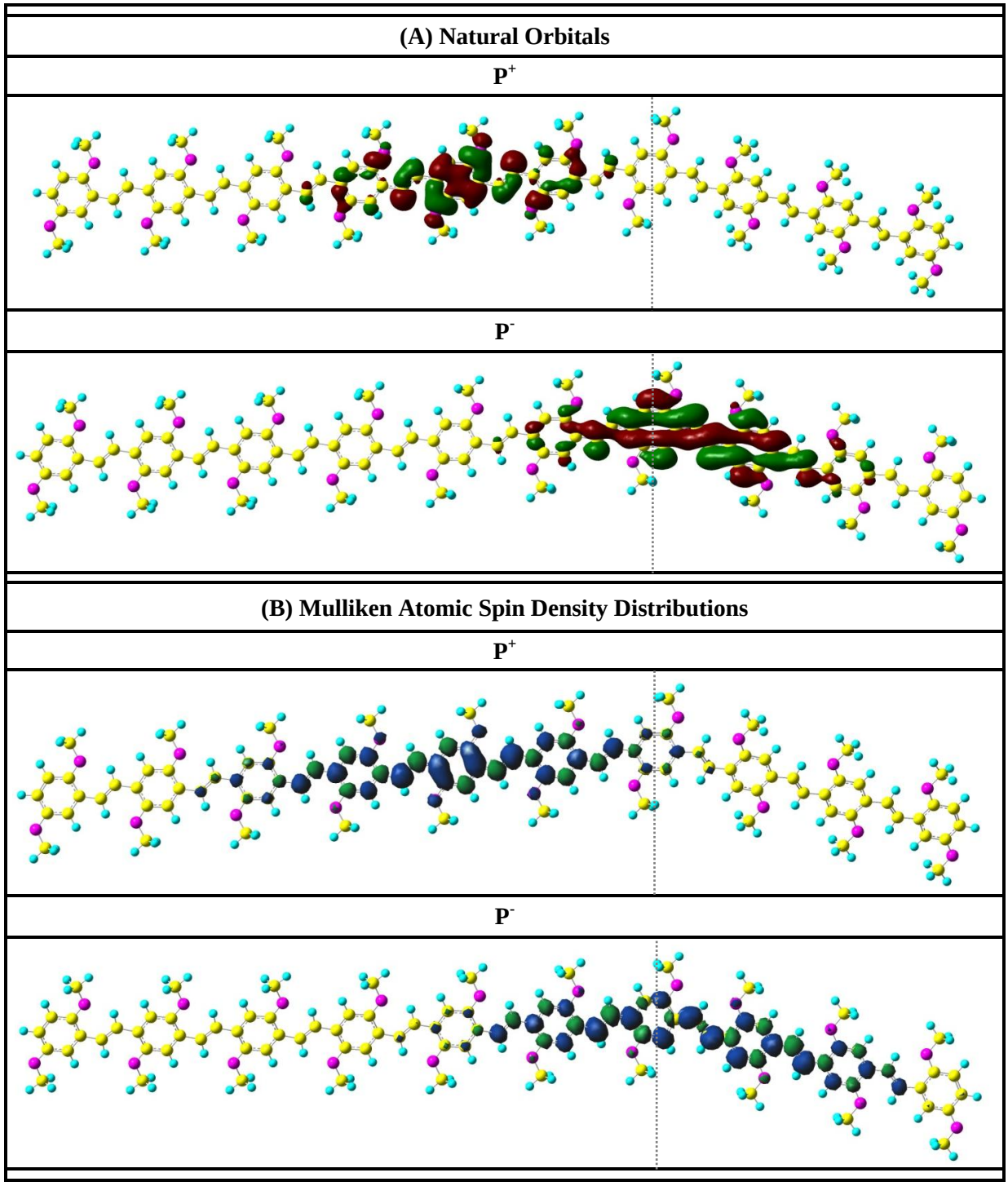

Figure 7.8: Characteristic natural orbitals (NOs) for singly occupied electronic levels and Mulliken atomic spin density distribution plots for P^+ and P^- excitations for *trans*-SK (6-3) conformation of MEH-PPV oligomer optimized at LC-wPBE/6-31G* level in the presence of solvent.

These plots virtually show that the localization of P^+ is away from the defect position as opposed to the P^- state which is spread on the defect site.

7.7 Conclusions

In summary, we presented a detailed computational study and analysis of the energetics and spatial localization of polaronic excitations in conjugated phenylene vinylene oligomers with weak and strong conformational distortions. We observe that the particle-hole symmetry for undistorted all-*trans* MEH-PPV geometries is broken with the introduction of weak-*trans* defects. As opposed to being localized in the middle of the chain, the electron is now attracted to the defect site while the hole is repelled away. At the same time, both holes and electrons are repelled away from the strong defect sites of *cis* nature. The localization patterns for the polaronic excitations were observed to be invariant with respect to the position of defects along the chain. Inclusion of a polarizable dielectric medium (solvent) is found to be crucial for the self-trapping of positive and negative polarons. However, it has a different influence on two distinct origins of localization. The polar solvent tends to increase the lattice distortion during geometry relaxation processes for P^-, while P^+ exhibit less localization than the gas phase. The solvent tends to increase the spatial confinement of electronic wavefunction for both types of polarons, although the effect is highly pronounced for P^+. This is in a clear agreement with an experimental study,[68] where the electrons are reported to be more localized than the hole for MEH-PPV oligomers. On the other hand, the pristine PPV chains preserve the particle-hole symmetry even with the introduction of these defects. The *trans* isomers are observed to localize the charges in the middle, while the polarons are spatially kept away from the *cis*-defect positions. The solvent seems to enhance the extent of lattice and spin distortion equally for P^+

and P^- for all geometry types. The larger binding and solvation energies for P^- in comparison to P^+ in MEH-PPV than unsubstituted PPV elucidates the distinct localization patterns for holes and electrons in these oligomers.

We also found that the localized P^+ and P^- states exhibit double-well potentials for weak-trans distorted geometries of MEH-PPV oligomers. The energy difference between the two wells is much higher for P^- than P^+. Thus, the hole is observed to have higher drift mobilities in weak-*trans* MEH-PPV geometries than the electrons as also predicted by their observed lower reorganization energies according to Marcus hopping model.[166] Hence, this study allows us to tune the charge-transport and photo-physical properties in conjugated organic materials by understanding their structure-property relations.

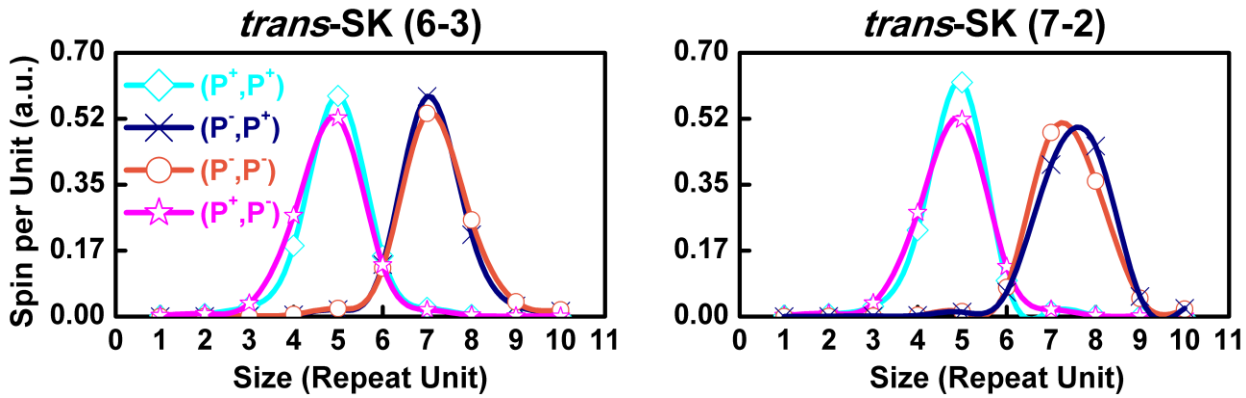

Figure 7.S1: Variation of Mulliken atomic spin densities (a.u.) per repeat unit (right) of the MEH-PPV oligomer in the *trans*-SK (6-3) and *trans*-SK (7-2) conformations for P^+ and P^- polarons in their optimal geometries as well as native geometries of opposite charged states. The calculations are performed at LC-wPBE/6-31G* level in the presence of solvent. We have used a notation "(X,Y)" in the legend, where X denotes the fully relaxed state of the system, while Y denotes the state for which spin is calculated.

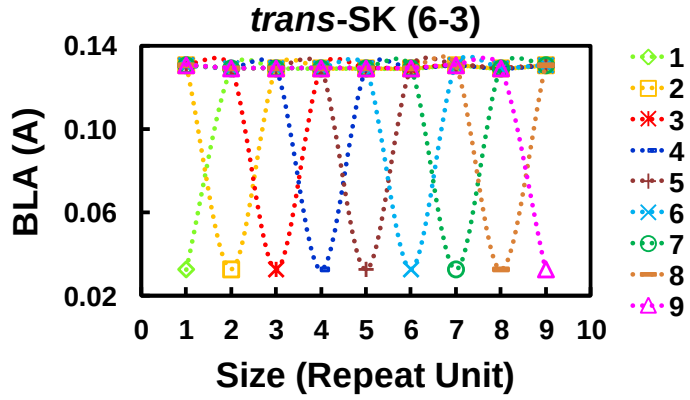

Figure 7.S2: Variation of BLA (Å) of the initial states for MEH-PPV oligomer in its *trans*-SK (6-3) conformation for Figure 7.6.
In Figure 7.6, the P^+ and P^- states are optimzied for all these different configurations as depicted here. These nine initial geometries are named according to the specific location of the distorted vinyl bond on the chain from one end to another.

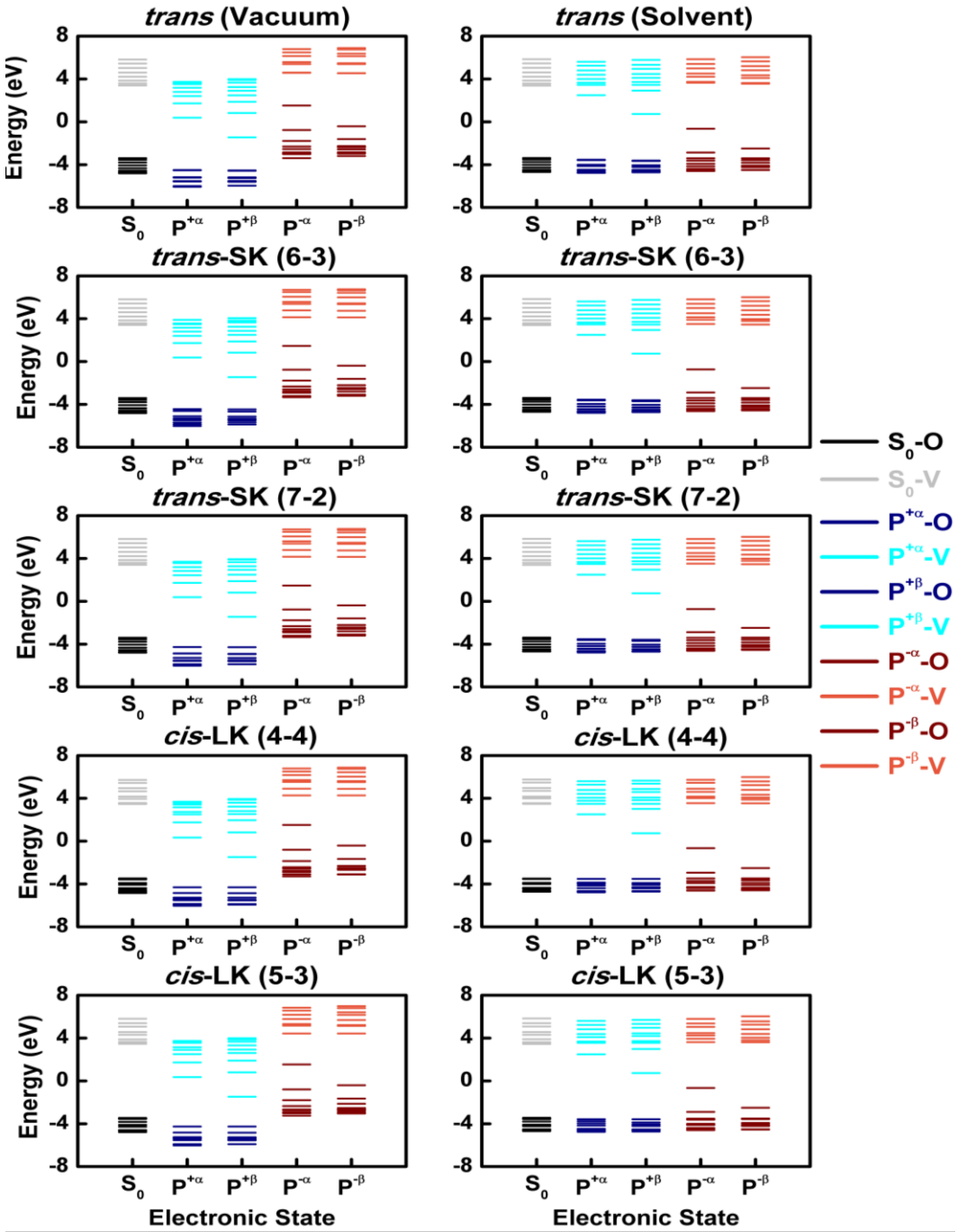

Figure 7.S3. Density of Kohn-Sham states of MEH-PPV oligomer using various geometrical conformations at LC-wPBE/6-31G* level for S_0, P^+ and P^- states.
The alpha (α) and beta (β) molecular orbitals (MOs) of each spin states are shown separately (represented by the same color). The darker (lighter) shades in the figure correspond to the occupied (O) and virtual (V) orbitals, respectively. Both vacuum (left) and solvent (right) calculations are shown.

APPENDIX: LIST OF PUBLICATIONS

1. **Nayyar I. H.,** Batista E. R., Tretiak S., Saxena A., Smith D. L., Martin R. L. **Role of geometric distortion and polarization in localization of electronic excitations in conjugated polymers**, *J. Chem. Theor. Comput.*, 9; 1144-1154, **2013**.
2. **Nayyar I. H.,** Batista E. R., Tretiak S., Saxena A., Smith D. L., Martin R. L. **Effect of *trans* and *cis* isomeric defects on the localization of charged excitations in π-conjugated organic polymers**, *J. Polym. Sci., Part B: Polym. Phys.* "Accepted", **2013**. **"Graphical Abstract Image has been selected as the front cover of the upcoming issue of J. Polym. Sci., Part B: Polym. Phys."**
3. **Nayyar I. H.**, Batista E. R., Tretiak S., Saxena A., Smith D. L., Martin R. L. **Localization of electronic excitations in conjugated polymers studied by DFT,** *J. Phys. Chem. Lett.* 2; 566-571, **2011**.
4. **Nayyar, I. H.,** Mikhailov, I. A.; Masunov, A. E. **Comparison of semiempirical methods for two-photon prediction of substituted stilbenes**, *J. Mol. Mod.*, "Submitted", **2012**.
5. **Nayyar, I. H.**, Mikhailov, I. A., Masunov, A. E. **Comparison of TD-DFT methods used for prediction of two-photon absorption spectra**, *J. Phys. Chem. C*, "Under Revision."
6. Hu H., Fishman D. A., Gerasov A. O., Przhonska O. V., Webster S., Padilha L. A., Peceli D., Shandura M., Kovtun Y. P., Kachkovski A. D., **Nayyar I. H.**, Masunov A. E., Tongwa P., Timofeeva T. V., Hagan D. J., Van Stryland E. W. **Two-photon absorption spectrum of a single crystal cyanine-like dye**, *J. Phys. Chem. Lett.* 3; 1222-1228, **2012**.
7. Gerasov A. O., **Nayyar I. H.**, Masunov A. E., Przhonskta O. V., Kachkovsky O. D., Melnyk D. O., Ryabitsky O. B., Viniychuk O.O, Solitonic Waves in Polyene Dications

and Principles Of Charge Carrier Localization in π-Conjugated Organic Materials, *Int. J. of Qtm. Chem.* 112; 2659-2667, **2012**.

8. Crotty A. M., **Nayyar I. H.**, Powell J. R., Masunov A. E., Hu Z. J., Gesquiere A. J. **Molecular structure of organic solar cell materials. Part1: Insight from the emission lineshapes of P3HT/PCBM**, *J. Phys. Chem. Lett.*, "Under Revision."

LIST OF REFERENCES

1. Zijlstra, P.; Chon, J. W. M.; Gu, M. *Nature* **2009,** 459, (7245), 410-413.
2. Juodkazis, S.; Mizeikis, V.; Matsuo, S.; Ueno, K.; Misawa, H. *Bulletin of the Chemical Society of Japan* **2008,** 81, (4), 411-448.
3. Li, H. R.; Xie, T.; Hu, N. D.; Yang, L. F.; Zhang, S. T.; Gao, F. *Progress in Chemistry* **2009,** 21, (7-8), 1398-1407.
4. Filippidis, G.; Gualda, E. J.; Mari, M.; Troulinaki, K.; Fotakis, C.; Tavernarakis, N. *Micron* **2009,** 40, (8), 876-880.
5. Frisch, M. J. T., G. W.; Schlegel, H. B.; Scuseria, G. E.; Robb, M. A.; Cheeseman, J. R.; Scalmani, G.; Barone, V.; Mennucci, B.; Petersson, G. A.; Nakatsuji, H.; Caricato, M.; Li, X.; Hratchian, H. P.; Izmaylov, A. F.; Bloino, J.; Zheng, G.; Sonnenberg, J. L.; Hada, M.; Ehara, M.; Toyota, K.; Fukuda, R.; Hasegawa, J.; Ishida, M.; Nakajima, T.; Honda, Y.; Kitao, O.; Nakai, H.; Vreven, T.; Montgomery, Jr., J. A.; Peralta, J. E.; Ogliaro, F.; Bearpark, M.; Heyd, J. J.; Brothers, E.; Kudin, K. N.; Staroverov, V. N.; Kobayashi, R.; Normand, J.; Raghavachari, K.; Rendell, A.; Burant, J. C.; Iyengar, S. S.; Tomasi, J.; Cossi, M.; Rega, N.; Millam, N. J.; Klene, M.; Knox, J. E.; Cross, J. B.; Bakken, V.; Adamo, C.; Jaramillo, J.; Gomperts, R.; Stratmann, R. E.; Yazyev, O.; Austin, A. J.; Cammi, R.; Pomelli, C.; Ochterski, J. W.; Martin, R. L.; Morokuma, K.; Zakrzewski, V. G.; Voth, G. A.; Salvador, P.; Dannenberg, J. J.; Dapprich, S.; Daniels, A. D.; Farkas, Ö.; Foresman, J. B.; Ortiz, J. V.; Cioslowski, J.; Fox, D. J. Gaussian 09, Revision A.1; Gaussian Inc.; Wallingford CT, **2009**.

6. Slyfield, C. R.; Niemeyer, K. E.; Tkachenko, E. V.; Tomlinson, R. E.; Steyer, G. G.; Patthanacharoenphon, C. G.; Kazakia, G. J.; Wilson, D. L.; Hernandez, C. J. *J Microsc* **2009,** 236, (1), 52-59.

7. Patel, P. D.; Masunov, A. E. *Journal of Physical Chemistry A* **2009,** 113, (29), 8409-8414.

8. Orr, B. J.; Ward, J. F. *Molecular Physics* **1971,** 20, (3), 513-526.

9. Sun, Y.; Zhao, Y.; Liu, X.-T.; Ren, A.-M.; Feng, J.-K.; Yu, X.-Q. *Journal of Molecular Modeling* **2012,** 18, (6), 2357-2367.

10. Kokil, A.; Yang, K.; Kumar, J. *Journal of Polymer Science Part B-Polymer Physics* **2012,** 50, (15), 1130-1144.

11. Beljonne, D.; Cornil, J.; Shuai, Z.; Bredas, J. L.; Rohlfing, F.; Bradley, D. D. C.; Torruellas, W. E.; Ricci, V.; Stegeman, G. I. *Physical Review B* **1997,** 55, (3), 1505-1516.

12. Xing, X.-J.; Li, J.; Sun, Y.-P.; Wang, C.-K. *Journal of Molecular Structure-Theochem* **2008,** 849, (1-3), 116-121.

13. Albota, M.; Beljonne, D.; Bredas, J. L.; Ehrlich, J. E.; Fu, J. Y.; Heikal, A. A.; Hess, S. E.; Kogej, T.; Levin, M. D.; Marder, S. R.; McCord-Maughon, D.; Perry, J. W.; Rockel, H.; Rumi, M.; Subramaniam, C.; Webb, W. W.; Wu, X. L.; Xu, C. *Science* **1998,** 281, (5383), 1653-1656.

14. Das, G. P.; Yeates, A. T.; Dudis, D. S. *Chemical Physics Letters* **2002,** 361, (1-2), 71-78.

15. Zojer, E.; Beljonne, D.; Kogej, T.; Vogel, H.; Marder, S. R.; Perry, J. W.; Bredas, J. L. *Journal of Chemical Physics* **2002,** 116, (9), 3646-3658.

16. Zhou, X.; Ren, A. M.; Feng, J. K.; Liu, X. J. *Journal of Physical Chemistry A* **2003,** 107, (11), 1850-1858.

17. Hales, J. M.; Hagan, D. J.; Van Stryland, E. W.; Schafer, K. J.; Morales, A. R.; Belfield, K. D.; Pacher, P.; Kwon, O.; Zojer, E.; Bredas, J. L. *Journal of Chemical Physics* **2004,** 121, (7), 3152-3160.

18. Corredor, C. C.; Belfield, K. D.; Bondar, M. V.; Przhonska, O. V.; Hernandez, F. E.; Kachkovsky, O. D. *Journal of Photochemistry and Photobiology a-Chemistry* **2006,** 184, (1-2), 177-183.

19. Zhu, L.; Yi, Y.; Shuai, Z.; Schmidt, K.; Zojer, E. *Journal of Physical Chemistry A* **2007,** 111, (34), 8509-8518.

20. Schmidt, K.; Leclercq, A.; Zojer, E.; Lawson, P. V.; Jang, S.-H.; Barlow, S.; Jen, A. K. Y.; Marder, S. R.; Bredas, J.-L. *Advanced Functional Materials* **2008,** 18, (5), 794-801.

21. AlSalhi, M. S.; Ibnaouf, K. H.; Masilamani, V.; Yassin, O. A. *Journal of Luminescence* **2012,** 132, (2), 484-490.

22. Liang, W. K.; Isborn, C. M.; Li, X. S. *Journal of Chemical Physics* **2009,** 131, (20), 204101(6).

23. Meng, S.; Kaxiras, E. *Journal of Chemical Physics* **2008,** 129, (5), 054110(12).

24. Cronstrand, P.; Luo, Y.; Agren, H. *Chemical Physics Letters* **2002,** 352, (1-2), 262-269.

25. Salek, P.; Vahtras, O.; Guo, J. D.; Luo, Y.; Helgaker, T.; Agren, H. *Chemical Physics Letters* **2003,** 374, (5-6), 446-452.

26. Frediani, L.; Rinkevicius, Z.; Agren, H. *Journal of Chemical Physics* **2005,** 122, (24), 244104(12).

27. Day, P. N.; Nguyen, K. A.; Pachter, R. *Journal of Physical Chemistry B* **2005,** 109, (5), 1803-1814.

28. Day, P. N.; Nguyen, K. A.; Pachter, R. *Journal of Chemical Physics* **2006,** 125, (9), 094103(13).

29. Day, P. N.; Nguyen, K. A.; Pachter, R. *Journal of Chemical Theory and Computation* **2008,** 4, (7), 1094-1106.

30. Zein, S.; Delbecq, F.; Simon, D. *Physical Chemistry Chemical Physics* **2009,** 11, (4), 694-702.

31. Hrobarikova, V.; Hrobarik, P.; Gajdos, P.; Fitilis, I.; Fakis, M.; Persephonis, P.; Zahradnik, P. *Journal of Organic Chemistry* **2010,** 75, (9), 3053-3068.

32. Kobko, N.; Masunov, A.; Tretiak, S. *Chemical Physics Letters* **2004,** 392, (4-6), 444-451.

33. Mikhailov, I. A.; Tafur, S.; Masunov, A. E. *Physical Review A* **2008,** 77, (1), 012510(11).

34. Awasthi, M.; Vanne, Y. V.; Saenz, A.; Castro, A.; Decleva, P. *Physical Review A* **2008,** 77, (6), 063403(17).

35. Fowe, E. P.; Bandrauk, A. D. *Physical Review A* **2011,** 84, (3), 035402(5).

36. Wallikewitz, B. H.; Kabra, D.; Gelinas, S.; Friend, R. H. *Physical Review B* **2012,** 85, (4), 045209(15).

37. AlSalhi, M. S.; Alam, J.; Dass, L. A.; Raja, M. *International Journal of Molecular Sciences* **2011,** 12, (3), 2036-2054.

38. He, Z.; Kan, C. W.; Ho, C. L.; Wong, W. Y.; Chui, C. H.; Tong, K. L.; So, S. K.; Lee, T. H.; Leung, L. M.; Lin, Z. Y. *Dyes and Pigments* **2011,** 88, (3), 333-343.

39. Tang, W. H.; Hai, J. F.; Dai, Y.; Huang, Z. J.; Lu, B. Q.; Yuan, F.; Tang, J. A.; Zhang, F. J. *Solar Energy Materials and Solar Cells* **2010,** 94, (12), 1963-1979.

40. Liao, K. S.; Yambem, S. D.; Haldar, A.; Alley, N. J.; Curran, S. A. *Energies* **2010,** 3, (6), 1212-1250.

41. Mayoral, M. J.; Ovejero, P.; Cano, M.; Orellana, G. *Dalton Transactions* **2011,** 40, (2), 377-383.

42. Samuel, I. D. W.; Turnbull, G. A. *Chemical Reviews* **2007,** 107, (4), 1272-1295.

43. Akiyama, S. *Journal of Synthetic Organic Chemistry Japan* **2012,** 70, (5), 465-472.

44. Sun, S. Y.; Salim, T.; Wong, L. H.; Foo, Y. L.; Boey, F.; Lam, Y. M. *Journal of Materials Chemistry* **2011,** 21, (2), 377-386.

45. Etzold, F.; Howard, I. A.; Mauer, R.; Meister, M.; Kim, T. D.; Lee, K. S.; Baek, N. S.; Laquai, F. *Journal of the American Chemical Society* **2011,** 133, (24), 9469-9479.

46. Xue, J. *Polymer Reviews* **2010,** 50, (4), 411-419.

47. Gemayel, M. E.; Treier, M.; Musumeci, C.; Li, C.; Mullen, K.; Samori, P. *Journal of the American Chemical Society* **2012,** 134, (4), 2429-2433.

48. Kergoat, L.; Piro, B.; Berggren, M.; Horowitz, G.; Pham, M.-C. *Analytical and bioanalytical chemistry* **2012,** 402, (5), 1813-1826.

49. Kola, S.; Sinha, J.; Katz, H. E. *Journal of Polymer Science Part B-Polymer Physics* **2012,** 50, (15), 1090-1120.

50. Matsuo, Y. *Chemistry Letters* **2012,** 41, (8), 754-759.

51. Reineke, S.; Walzer, K.; Leo, K. *Physical Review B* **2007,** 75, (12), 125328(13).

52. Sun, Z.; Stafstrom, S. *Journal of Chemical Physics* **2012,** 136, (24), 244901(5).

53. Ge, L.; Li, S.; George, T. F.; Sun, X. *Physics Letters A* **2008,** 372, (19), 3375-3379.

54. Bounioux, C.; Katz, E. A.; Yerushalmi-Rozen, R. *Polymers for Advanced Technologies* **2012,** 23, (8), 1129-1140.

55. Labat, F.; Le Bahers, T.; Ciofini, I.; Adamo, C. *Accounts of Chemical Research* **2012,** 45, (8), 1268-1277.

56. Aryanpour, K.; Sheng, C. X.; Olejnik, E.; Pandit, B.; Psiachos, D.; Mazumdar, S.; Vardeny, Z. V. *Physical Review B* **2011,** 83, (15), 155124(5).

57. Bedard-Hearn, M. J.; Sterpone, F.; Rossky, P. J. *Journal of Physical Chemistry A* **2010,** 114, (29), 7661-7670.

58. Dykstra, T. E.; Hennebicq, E.; Beljonne, D.; Gierschner, J.; Claudio, G.; Bittner, E. R.; Knoester, J.; Scholes, G. D. *Journal of Physical Chemistry B* **2009,** 113, (3), 656-667.

59. Frolov, S. V.; Kloc, C.; Batlogg, B.; Wohlgenannt, M.; Jiang, X.; Vardeny, Z. V. *Physical Review B* **2001,** 63, (20), 205203(12).

60. Clark, J.; Nelson, T.; Tretiak, S.; Cirmi, G.; Lanzani, G. *Nature Physics* **2012,** 8, (3), 225-231.

61. Thorsmølle, V. K.; Averitt, R. D.; Demsar, J.; Smith, D. L.; Tretiak, S.; Martin, R. L.; Chi, X.; Crone, B. K.; Ramirez, A. P.; Taylor, A. J. *Physical Review Letters* **2009,** 102, (1), 017401(4).

62. Tretiak, S.; Chao, W.; Chernyak, V. Y. *Chemical Physics Letters* **2007,** 433, (4-6), 305-311.

63. Hoyer, U.; Wagner, M.; Swonke, T.; Bachmann, J.; Auer, R.; Osvet, A.; Brabec, C. J. *Applied Physics Letters* **2010,** 97, (23), 233303(3).

64. Moses, D.; Dogariu, A.; Heeger, A. J. *Physical Review B* **2000,** 61, (14), 9373-9379.

65. Yin, K. Z.; Zhang, L. F.; Lai, C. L.; Zhong, L. L.; Smith, S.; Fong, H.; Zhu, Z. T. *Journal of Materials Chemistry* **2011,** 21, (2), 444-448.

66. Osterbacka, R.; Wohlgenannt, M.; Shkunov, M.; Chinn, D.; Vardeny, Z. V. *Journal of Chemical Physics* **2003,** 118, (19), 8905-8916.

67. Kohler, A.; dos Santos, D. A.; Beljonne, D.; Shuai, Z.; Bredas, J. L.; Holmes, A. B.; Kraus, A.; Mullen, K.; Friend, R. H. *Nature* **1998,** 392, (6679), 903-906.

68. McCamey, D. R.; van Schooten, K. J.; Baker, W. J.; Lee, S. Y.; Paik, S. Y.; Lupton, J. M.; Boehme, C. *Physical Review Letters* **2010,** 104, (1), 017601(4).

69. Frankevich, E.; Nishihara, Y.; Fujii, A.; Ozaki, M.; Yoshino, K. *Physical Review B (Condensed Matter and Materials Physics)* **2002,** 66, (15), 155203(7).

70. Kuroda, S.; Marumoto, K.; Shimoi, Y.; Abe, S. *Thin Solid Films* **2001,** 393, (1-2), 304-309.

71. Drew, A. J.; Hoppler, J.; Schulz, L.; Pratt, F. L.; Desai, P.; Shakya, P.; Kreouzis, T.; Gillin, W. P.; Suter, A.; Morley, N. A. e. a. *Nature Materials* **2009,** 8, (2), 109-114.

72. Moro, G.; Scalmani, G.; Cosentino, U.; Pitea, D. *Synthetic Metals* **2000,** 108, (2), 165-172.

73. Geskin, V. M.; Cornil, J.; Bredas, J. L. *Chemical Physics Letters* **2005,** 403, (1-3), 228-231.

74. Zuppiroli, L.; Bieber, A.; Michoud, D.; Galli, G.; Gygi, F.; Bussac, M. N.; Andre, J. J. *Chemical Physics Letters* **2003,** 374, (1-2), 7-12.

75. Geskin, V. M.; Dkhissi, A.; Bredas, J. L. *International Journal of Quantum Chemistry* **2003,** 91, (3), 350-354.

76. Igumenshchev, K. I.; Tretiak, S.; Chernyak, V. Y. *Journal of Chemical Physics* **2007,** 127, 114902(10).

77. Masunov, A.; Tretiak, S.; Hong, J. W.; Liu, B.; Bazan, G. C. *Journal of Chemical Physics* **2005,** 122, (22), 224505(10).

78. Franco, I.; Tretiak, S. *Journal of the American Chemical Society* **2004,** 126, (38), 12130-12140.

79. Tretiak, S.; Saxena, A.; Martin, R. L.; Bishop, A. R. *Physical Review Letters* **2002,** 89, (9), 097402(4).

80. Meng, K.; Ding, Q.; Wang, S. F.; Gong, Q. H. *Chemical Physics Letters* **2011,** 515, (1-3), 155-158.

81. Traub, M. C.; Lakhwani, G.; Bolinger, J. C.; Vanden Bout, D.; Barbara, P. F. *Journal of Physical Chemistry B* **2011,** 115, (33), 9941-9947.

82. Becker, K.; Da Como, E.; Feldmann, J.; Scheliga, F.; Csanyi, E. T.; Tretiak, S.; Lupton, J. M. *Journal of Physical Chemistry B* **2008,** 112, (16), 4859-4864.

83. Ghosh, H. *Synthetic Metals* **2008,** 158, (8-9), 320-329.

84. Kilina, S.; Batista, E. R.; Yang, P.; Tretiak, S.; Saxena, A.; Martin, R. L.; Smith, D. L. *Acs Nano* **2008,** 2, (7), 1381-1388.

85. Sun, M. T.; Kjellberg, P.; Beenken, W. J. D.; Pullerits, T. *Chemical Physics* **2006,** 327, (2-3), 474-484.

86. Yang, P.; Batista, E. R.; Tretiak, S.; Saxena, A.; Martin, R. L.; Smith, D. L. *Physical Review B* **2007,** 76, (24), 241201(4).

87. Karabunarliev, S.; Bittner, E. R. *Journal of Chemical Physics* **2003,** 118, (9), 4291-4296.

88. Franco, I.; Tretiak, S. *Chemical Physics Letters* **2003,** 372, (3-4), 403-408.

89. Campbell, L. H.; Smith, D. L.; Tretiak, S.; Martin, R. L.; Neef, C. J.; Ferraris, J. R. *Physical Review B* **2002,** 65, (8), 085210(8).

90. Norton, J. E.; Bredas, J. L. *Journal of the American Chemical Society* **2008,** 130, (37), 12377-12384.

91. Miranda, R. P.; Fisher, A. J.; Stella, L.; Horsfield, A. P. *Journal of Chemical Physics* **2011,** 134, (24), 244102(13).

92. Sai, N.; Barbara, P. F.; Leung, K. *Physical Review Letters* **2011,** 106, (22), 085210 (8).

93. Geskin, V. M.; Grozema, F. C.; Siebbeles, L. D. A.; Beljonne, D.; Bredas, J. L.; Cornil, J. *Journal of Physical Chemistry B* **2005,** 109, (43), 20237-20243.

94. Zojer, E.; Buchacher, P.; Wudl, F.; Cornil, J.; Calbert, J. P.; Bredas, J. L.; Leising, G. *Journal of Chemical Physics* **2000,** 113, (22), 10002-10012.

95. Frolov, S. V.; Bao, Z.; Wohlgenannt, M.; Vardeny, Z. V. *Physical Review Letters* **2000,** 85, (10), 2196-2199.

96. Norton, J. E.; Bredas, J.-L. *Journal of the American Chemical Society* **2008,** 130, (37), 12377-12384.

97. Melzer, C.; Koop, E. J.; Mihailetchi, V. D.; Blom, P. W. M. *Advanced Functional Materials* **2004,** 14, (9), 865-870.

98. Harbron, E. J.; Hadley, D. H.; Imm, M. R. *Journal of Photochemistry and Photobiology a-Chemistry* **2007,** 186, (2-3), 151-157.

99. Grimes, A. F.; Call, S. E.; Harbron, E. J.; English, D. S. *Journal of Physical Chemistry C* **2007,** 111, (38), 14257-14265.

100. Lewis, S. M.; Harbron, E. J. *Journal of Physical Chemistry C* **2007,** 111, (11), 4425-4430.

101. Son, S.; Dodabalapur, A.; Lovinger, A. J.; Galvin, M. E. *Science* **1995,** 269, (5222), 376-378.

102. Liu, D.; Yin, S.; Xu, H.; Liu, X.; Sun, G.; Xie, Z.; Yang, B.; Ma, Y. *Chemical Physics* **2011,** 388, (1-3), 69-77.

103. Szabo, A.; Ostlund, N. S. *Modern Quantum Chemistry* **1996,** Dover Publishing, Minneola, Newyork.

104. Levine, I. N. *Qunatum Chemistry* **2000,** Prentice Hall, New Jersey.

105. Anderson, W. P.; Edwards, W. D.; Zerner, M. C. *Inorganic Chemistry* **1986,** 25, (16), 2728-2732.

106. Bacon, A. D.; Zerner, M. C. *Theoretica Chimica Acta* **1979,** 53, (1), 21-54.

107. W., K.; M.H., S. *A Chemist's Guide to Density Functional Theory* **2002,** Wiley-VCH, Weinheim.

108. Parr, R. G.; W., Y. *Density Functional Theory of Atoms and Molecules* **1989,** Oxford Univeristy Press, New York.

109. Kohn, W.; Sham, L. J. *Physical Review* **1965,** 140, (4A), 1133-1138.

110. Hohenberg, P.; Kohn, W. *Physical Review B* **1964,** 136, (3B), 864-865.

111. Runge, E.; Gross, E. K. U. *Physical Review Letters* **1984,** 52, (12), 997-1000.

112. Stratmann, R. E.; Scuseria, G. E.; Frisch, M. J. *Journal of Chemical Physics* **1998,** 109, (19), 8218-8224.

113. Tretiak, S.; Chernyak, V. *Journal of Chemical Physics* **2003,** 119, (17), 8809-8823.

114. Chernyak, V.; Mukamel, S. *Journal of Chemical Physics* **2000,** 112, (8), 3572-3579.

115. Hirata, S.; Head-Gordon, M. *Chemical Physics Letters* **1999,** 314, 291-299.

116. Dunning, T. H.; McKoy, V. *Journal of Chemical Physics* **1967,** 47, (5), 1735-1747.

117. Savin, A.; Umrigar, C. J.; Gonze, X. *Chemical Physics Letters* **1998,** 288, (2-4), 391-395.

118. Olsen, J.; Jorgensen, P. *Journal of Chemical Physics* **1985,** 82, (7), 3235-3264.

119. Ohta, K.; Kamada, K. *Journal of Chemical Physics* **2006,** 124, (12), 124303(11).

120. Rumi, M.; Ehrlich, J. E.; Heikal, A. A.; Perry, J. W.; Barlow, S.; Hu, Z. Y.; McCord-Maughon, D.; Parker, T. C.; Rockel, H.; Thayumanavan, S.; Marder, S. R.; Beljonne, D.; Bredas, J. L. *Journal of the American Chemical Society* **2000,** 122, (39), 9500-9510.

121. Masunov, A. M.; Tretiak, S. *Journal of Physical Chemistry B* **2004,** 108, (3), 899-907.

122. Kamarchik, E.; Krylov, A. I. *Journal of Physical Chemistry Letters* **2011,** 2, (5), 488-492.

123. Murugan, N. A.; Kongsted, J.; Rinkevicius, Z.; Aidas, K.; Mikkelsen, K. V.; Agren, H. *Physical Chemistry Chemical Physics* **2011,** 13, (27), 12506-12516.

124. Silva, D. L.; Murugan, N. A.; Kongsted, J.; Rinkevicius, Z.; Canuto, S.; Agren, H. *Journal of Physical Chemistry B* **2012,** 116, (28), 8169-8181.

125. Sasagane, K.; Aiga, F.; Itoh, R. *Journal of Chemical Physics* **1993,** 99, (5), 3738-3778.

126. Pond, S. J. K.; Rumi, M.; Levin, M. D.; Parker, T. C.; Beljonne, D.; Day, M. W.; Bredas, J. L.; Marder, S. R.; Perry, J. W. *Journal of Physical Chemistry A* **2002,** 106, (47), 11470-11480.

127. Cronstrand, P.; Luo, Y.; Agren, H. *Advances in Quantum Chemistry, Vol 50* **2005,** 50, 1-21.

128. Krukau, A. V.; Vydrov, O. A.; Izmaylov, A. F.; Scuseria, G. E. *Journal of Chemical Physics* **2006,** 125, (22), 224106(5).

129. Stephens, P. J.; Devlin, F. J.; Chabalowski, C. F.; Frisch, M. J. *Journal of Physical Chemistry* **1994,** 98, (45), 11623-11627.

130. Becke, A. D. *Journal of Chemical Physics* **1993,** 98, (7), 5648-5652.

131. Lee, C. T.; Yang, W. T.; Parr, R. G. *Physical Review B* **1988,** 37, (2), 785-789.

132. Zhao, Y.; Schultz, N. E.; Truhlar, D. G. *Journal of Chemical Physics* **2005,** 123, (16), 161103(4).

133. Boese, A. D.; Martin, J. M. L. *Journal of Chemical Physics* **2004,** 121, (8), 3405-3416.

134. Zhao, Y.; Schultz, N. E.; Truhlar, D. G. *Journal of Chemical Theory and Computation* **2006,** 2, (2), 364-382.

135. Yanai, T.; Tew, D. P.; Handy, N. C. *Chemical Physics Letters* **2004,** 393, (1-3), 51-57.

136. Likura, H.; Tsuneda, T.; Yanai, T.; Hirao, K. *Journal of Chemical Physics* **2001,** 115, (8), 3540-3544.

137. Badaeva, E. A.; Timofeeva, T. V.; Masunov, A. M.; Tretiak, S. *Journal of Physical Chemistry A* **2005,** 109, (32), 7276-7284.

138. Belfield, K. D.; Bondar, M. V.; Hernandez, F. E.; Masunov, A. E.; Mikhailov, I. A.; Morales, A. R.; Przhonska, O. V.; Yao, S. *Journal of Physical Chemistry C* **2009,** 113, (11), 4706-4711.

139. Wu, C.; Tretiak, S.; Chernyak, V. Y. *Chemical Physics Letters* **2007,** 433, (4-6), 305-311.

140. Epifanovsky, E.; Polyakov, I.; Grigorenko, B.; Nemukhin, A.; Krylov, A. I. *Journal of Chemical Theory and Computation* **2009,** 5, (7), 1895-1906.

141. Wasserman, A.; Maitra, N. T.; Burke, K. *Journal of Chemical Physics* **2005,** 122, (14).

142. Stewart, J. J. P. *Journal of Molecular Modeling* **2007,** 13, (12), 1173-1213.

143. openmopac.net.

144. Frisch, M. J., G. W. Trucks, H. B. Schlegel, G. E. Scuseria, M. A. Robb, J. R. Cheeseman, G. Scalmani, V. Barone, B. Mennucci, G. A. Petersson et al, Gaussian-09, Revision A.1, Gaussian Inc., Wallingford CT (2009).

145. Zerner, M. C., J. E. Ridley, A. D. Bacon, W. D. Edwards, J. D. Head, J. McKelvey, J. C. Culberson, P. Knappe, M. G. Cory, B. Weiner, J. D. Baker, W. A. Parkinson, D. Kannis, J. Yu, N. Roesch, M. Kotzian, T. Tamm, M. M. Karelson, X. Zheng, G. Pearl,

A. Broo, K. Albert, J. M. Cullen, J. Li, G. D. Hawkins, J. D. Thompson, C. P. Kelly, D. A. Liotard, A. V. Marenich, C. J. Cramer, and D. G. Truhlar, ZINDO-MN version 2011, Quantum Theory Project, University of Florida, Gainesville, and Department of Chemistry, University of Minnesota, Minneapolis (2011).

146. Nguyen, T. D.; Hukic-Markosian, G.; Wang, F. J.; Wojcik, L.; Li, X. G.; Ehrenfreund, E.; Vardeny, Z. V. *Nature Materials* **2010,** 9, (4), 345-352.

147. Cornil, J.; Beljonne, D.; Heller, C. M.; Campbell, I. H.; Laurich, B. K.; Smith, D. L.; Bradley, D. D. C.; Mullen, K.; Bredas, J. L. *Chemical Physics Letters* **1997,** 278, (1-3), 139-145.

148. Perdew, J. P.; Burke, K.; Ernzerhof, M. *Physical Review Letters* **1997,** 78, (7), 1396-1396.

149. Tawada, Y.; Tsuneda, T.; Yanagisawa, S.; Yanai, T.; Hirao, K. *Journal of Chemical Physics* **2004,** 120, (18), 8425-8433.

150. Martin, R. L. *Journal of Chemical Physics* **2003,** 118, (11), 4775-4777.

151. Suponitsky, K. Y.; Masunov, A. E.; Antipin, M. Y. *Mendeleev Communications* **2009,** 19, (6), 311-313.

152. Brabec, C. J.; Winder, C.; Scharber, M. C.; Sariciftci, N. S.; Hummelen, J. C.; Svensson, M.; Andersson, M. R. *Journal of Chemical Physics* **2001,** 115, (15), 7235-7244.

153. Nishihara, Y.; Frankevich, E.; Fujii, A.; Ozaki, M.; Yoshino, K. *Journal of the Physical Society of Japan* **2004,** 73, (7), 1888-1894.

154. Wei, X.; Hess, B. C.; Vardeny, Z. V.; Wudl, F. *Physical Review Letters* **1992,** 68, (5), 666-669.

155. Tammer, M.; Monkman, A. P. *Advanced Materials* **2002,** 14, (3), 210-212.

156. Zheng, G.; Clark, S. J.; Brand, S.; Abram, R. A. *Journal of Physics-Condensed Matter* **2004,** 16, (47), 8609-8620.

157. Sears, J. S.; Koerzdoerfer, T.; Zhang, C.-R.; Bredas, J.-L. *Journal of Chemical Physics* **2011,** 135, (15), 151103(4).

158. Magyar, R. J.; Tretiak, S. *Journal of Chemical Theory and Computation* **2007,** 3, (3), 976-987.

159. Nayyar, I. H.; Batista, E. R.; Tretiak, S.; Saxena, A.; Smith, D. L.; Martin, R. L. *Journal of Physical Chemistry Letters* **2011,** 2, (6), 566-571.

160. Wu, C.; Malinin, S. V.; Tretiak, S.; Chernyak, V. Y. *Nature Physics* **2006,** 2, (9), 631-635.

161. Brendel, P.; Grupp, A.; Mehring, M.; Schenk, R.; Mullen, K.; Huber, W. *Synthetic Metals* **1991,** 45, (1), 49-57.

162. Bredas, J. L.; Themans, B.; Fripiat, J. G.; Andre, J. M.; Chance, R. R. *Physical Review B* **1984,** 29, (12), 6761-6773.

163. Frolov, S. V.; Bao, Z.; Wohlgenannt, M.; Vardeny, Z. V. *Synthetic Metals* **2001,** 116, (1-3), 5-7.

164. Brocks, G. *Synthetic Metals* **1999,** 102, (1-3), 914-915.

165. Tao, J.; Tretiak, S.; Zhu, J.-X. *Journal of Chemical Physics* **2008,** 128, (8), 084110(8).

166. Marcus, R. A. *Reviews of Modern Physics* **1993,** 65, (3), 599-610.